ETH
Eidgenössische Technische Hochschule Zürich
Swiss Federal Institute of Technology Zurich

Laser Scanning Microscopy of Microwave Superconducting Lumped Element Resonators

Master Thesis

Junxin Chen

November 9, 2015

Advisors: Prof. Dr. Andreas Wallraff, Dr. Anton Potočnik
Department of Physics, ETH Zürich

Abstract

When laser shines on a superconductor optical photons can break Cooper pairs into quasiparitcles and change resistance and kinetic inductance of the superconductor. This kind of photo-induced change is called photo response. Laser scanning microscopy of superconductors is a measurement synchronizing photo response and spatial information of the laser beam. The principle of laser scanning microscopy has been, for instance, used to probe current density distribution in superconductors and build sensitive photon detectors. However, laser scanning microscopy has not been applied to lumped element resonators and superconducting circuits for quantum information purpose yet. In this thesis, we developed theory of photo response of superconducting lumped element resonators, developed measurement methods enabling us to extract photo-induced changes in resonator properties, studied photo response under different experimental conditions, and explored the possibility of operating laser scanning microscopy at quantum limited microwave powers.

Contents

Chapter 1

Introduction

Optical photons are able to break Cooper pairs in superconductors into quasiparticles (electrons no as Cooper pairs), and increase local resistivity and kinetic inductance. Laser Scanning Microscopy (LSM) of superconductors measures the photo-induced changes in their electrical properties. Any laser-induced change can be referred as photo response in the context of LSM. LSM of superconductors is originally developed for probing the current distribution in superconducting structures in 1993 [1, 2], based on the fact that laser-induced changes are proportional to square of local current density under laser probe [1, 3]. Using LSM as the probe for current, Zhuravel and his colleagues studied the influence of geometry of superconducting microwave devices on the current distribution flowing through them [4, 5, 6], and managed to engineer current distribution and magnetic field by choosing specific designs [3, 7]. Photo response of a superconductor depends on its composition of charge carriers and their dynamics. LSM was also used as a tool for studying properties of superconductors, especially high temperature superconductors [2, 8, 3]. Zhuravel and his colleagues also developed a method to extract local resistive and reactive photo response in terms of change in scattering parameters of a device [9]. This work inspired our development of photo response measurement in this thesis.

Using the same working principle as LSM, superconducting resonators are also used as highly sensitive photon detectors, called Microwave Kinetic Inductance Detectors (MKID) [10, 11]. Due to good scalability, MKID has important application in astronomy. Peter Day and his colleague first reported detecting single X-ray photons using superconducting coplanar waveguide array in 2003 [10]. Later, DC Moore and his colleague reported not-so-reliable detection of single optical photons using photon induced kinetic inductance change in 2009 [12]. Recently, integrated MKID chips, though not in single photon regime, have been used to acquire images of celestial

bodies with reasonable quality [11].

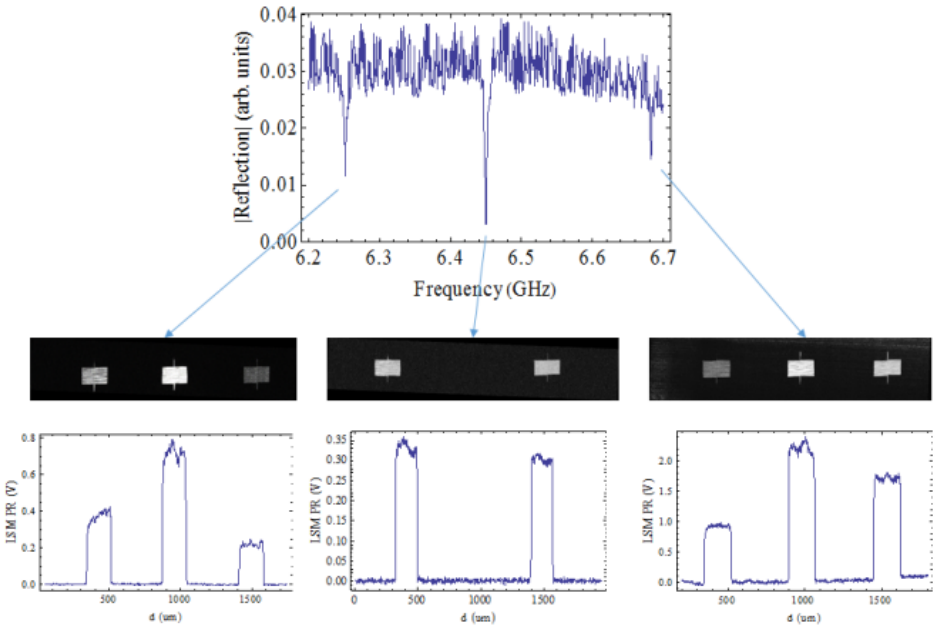

Figure 1.1: Probe resonance mode of linear chain of coupled resonator using laser scanning microscopy. Resonance mode of a coupled resonator system at different frequency has different oscillating amplitude distribution throughout the resonators. In some mode, some of the resonators may have zero oscillation amplitude, like the middle resonator in the middle mode in this figure. [13]

Superconducting circuits are promising candidates for quantum computation and quantum simulation. So far, coplanar waveguides are used for circuit control and circuit state readout. However, more control and readout lines result in more decoherence of quantum state. Without flux line, LSM could be a powerful tool to probe and tune the properties of superconducting circuits. In the quantum limit, LSM could be used to characterize quantum resonator (indirect measurement of quantum excitation). It could also be used as a way to tune the resonance frequency of a resonator without flux line. Even in classical limit, LSM has attractive applications. LSM could be used to detect spurious modes, like ground current. The information could be helpful for developing techniques to avoid these modes. LSM could also be used to detect different resonance modes of a coupled resonator system. Figure 1.1 shows an example of detecting resonance modes of a linear chain of 3 coupled resonators using LSM. Closely related to resonance modes detection, LSM provides the possibility to detect k vector in lattice of coupled resonators [13]. Being able to measuring k vector could be a significant contribution to quantum simulation using coupled resonator systems. However, LSM has not been used for superconducting circuits so far. The theory

of photo response of superconducting circuit is not well-established. The potential of tuning circuit properties with laser is not clear. Moreover, the possibility of detecting finite photo response at quantum limited microwave power is not known. To make the points clear, LSM of superconducting lumped element resonators at classical limited microwave and laser power at liquid Helium temperature is a suitable starting point.

In this study, we developed theory of photo response of superconducting lumped element resonators on the basis of general theory of photo response of superconductors. We also developed measurement methods enabling to extract photo-induced changes in resonance frequency and resistive energy loss rate of lumped element resonators, studied photo response and laser-induced changes in resonator properties under different experimental conditions, and proved the possibility to operating laser scanning microscopy at quantum limited microwave power.

The working principle of LSM is introduced in Chapter 2. The experimental setup and implementation of photo response measurement are introduced in Chapter 3. The experimental results are discussed in Chapter 4. Finally, the possibility of operating LSM at quantum limited microwave power and laser power is discussed in Chapter 5.

Chapter 2

Electrodynamics of Superconductors

Superconductors are lossless for DC current. However, when the current frequency is finite, reactance in the superconducting circuit will guide a part of current flowing through lossy channel of quasiparticles. The theory describing high frequency properties of superconductors was developed by C.J.Gorter and H.B.G.Casimir, even before the well-known BCS theory of superconductivity was presented [14]. Based on this theory, previous researchers and we derived the theory of photo response of superconductors. In this chapter, the basics of electrodynamics of superconductors, the basics of lumped element resonators, and the interaction between superconductor and optical laser will be introduced.

2.1 Two-Fluid Model

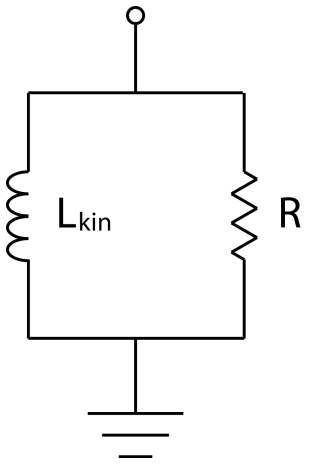

Figure 2.1: Circuit model for piece of superconductor.

There are two kinds of charge carriers in a superconductor at finite temperatures below critical temperature T_c. One kind is Cooper pairs, current of which is lossless (the current flowing through this channel is called supercurrent); the other kind is quasiparticles, which are free electrons not paired as Cooper pairs. Current of quasiparticles dissipates energy due to scattering of electrons on crystal lattice (resistive behavior). So, when the current is direct (DC), all current will flow through the lossless channel as long as the current density is below critical current density of the superconductor. However, when the current is alternative (AC), reactance of the superconducting circuit will guide a portion of current flowing through the lossy channel. To understand this, consider a circuit with an inductor and a resistor in parallel, as shown in Figure 2.1. Impedances of the two channels are given by $Z_L = i\omega L$ and $Z_R = R$ respectively, where L is inductance, R is resistance, i is imaginary unit, and ω is the angular frequency of current. When current frequency is 0, $Z_R = R$, while $Z_L = 0$, so all the current will flow through inductance channel. When current frequency is finite, the current distribution between the two channels will be given by $\frac{1}{R} : \frac{1}{i\omega L}$, such that current passing through lossy channel R is not zero. This argument applies to arbitrary design of superconducting circuit, because the inductance in Figure 2.1 comes from the inertia of Cooper pairs.

To model electrodynamics of superconductors formally, complex conductivity and surface impedance will be presented. According to Drude model, conductivity of a conductor is given by [15]:

$$\sigma = \frac{ne^2\tau}{m_e(1+\omega^2\tau^2)} - i\frac{ne^2\omega\tau^2}{m_e(1+\omega^2\tau^2)} = \sigma_1 - i\sigma_2\,, \tag{2.1}$$

where n is the charge carrier density, e is the charge of electron, τ is relaxation time of the charge carrier, m_e is the mass of electron, and i is imaginary unit. For Cooper pairs, τ goes to infinity, which leads to purely imaginary conductivity

$$\sigma_s(n_c) = -i\sigma_2(n_c) = -i\frac{2n_ce^2}{m_e\omega} = -i\frac{n_se^2}{m_e\omega} = \sigma_s(n_s)\,, \tag{2.2}$$

where n_c is the density of Cooper pair, and n_s is the density of superconducting electron (twice of n_c). Within the two fluid model, the total complex conductivity is given by [16]

$$\sigma = \sigma_1(n_n) - i(\sigma_2(n_s) + \sigma_2(n_n)) \tag{2.3}$$

$$= \frac{n_ne^2\tau}{m_e(1+\omega^2\tau^2)} - i\left(\frac{n_ne^2\omega\tau^2}{m_e(1+\omega^2\tau^2)} + \frac{n_se^2}{m_e\omega}\right)\,, \tag{2.4}$$

where n_n is the density of quasiparticles. In normal metals (as quasiparticles in superconductor), a typical electron-phonon relaxation time is around 10^{-13} s [17]. Therefore, for $\omega < 100$ GHz, terms with $\omega^2\tau^2$ and $\omega\tau^2$ vanish, leading to only Cooper pair contribution to the imaginary conductivity. As the interested angular frequency in this thesis is around 6.5 GHz, the total conductivity can be rewritten as

$$\sigma = \frac{n_n e^2 \tau}{m_e(1+\omega^2\tau^2)} - i\frac{n_s e^2}{m_e \omega}\,. \tag{2.5}$$

Properties like n_s and n_n are temperature dependent. One can absorb them into temperature dependent London penetration depth $\lambda_L(T)$, determining the characteristic depth for magnetic field penetrating into a superconductor [18]. London penetration depth at zero temperature $\lambda_L(0)$ is defined by

$$\lambda_L(0) = \sqrt{\frac{m_e}{n_s(0)e^2\mu_0}}\,, \tag{2.6}$$

where μ_0 is the magnetic permeability. Temperature dependence of n_s is given by

$$n_s(T) = n_s(0)\left(1 - \left(\frac{T}{T_c}\right)^m\right)\,, \tag{2.7}$$

where m is an approximate exponent given by two fluid model, ranging between 2 to 4 [19, 20, 8]. In our case, $m = 4$. Then the temperature dependent London penetration depth $\lambda_L(T)$ is given by

$$\lambda_L(T) = \sqrt{\frac{m_e}{n_s(T)e^2\mu_0}} = \frac{\lambda_L(0)}{\sqrt{1-(\frac{T}{T_c})^4}}\,. \tag{2.8}$$

With this expression, one can rewrite complex conductivity as

$$\sigma = \sigma_1 - i\sigma_2 = \frac{n_n}{n}\sigma_n - i\frac{1}{\omega\mu_0\lambda_L^2(T)}\,, \tag{2.9}$$

where n is the density of total free electrons, σ_n is the real conductivity of normal metal with quasiparticle density n_n.

2.2 Surface Impedance

By definition, the surface impedance $\underline{Z}_s$ of a conductor film is given by [21]

$$\underline{Z}_s = \frac{\int \vec{E} \cdot d\vec{s}}{\int \vec{H} \cdot d\vec{s}} = \sqrt{\frac{i\omega\mu_0}{\sigma}}\,, \tag{2.10}$$

assuming a harmonic plane wave. The total impedance $\underline{Z}$ of a thin sheet is thus

$$\underline{Z} = \underline{Z}_s \frac{l}{w}\,, \tag{2.11}$$

where l is the length of the sheet, and w is the width. The aspect ratio $\frac{l}{w}$ is independent from the actual dimension of the conductor sheet.

Substituting Equation 2.9 into Equation 2.10, one can rewrite surface impedance as

$$\underline{Z}_s = \sqrt{\frac{i\omega\mu_0}{\frac{n_n}{n}\sigma_n - i\frac{1}{\omega\mu_0\lambda_L^2(T)}}} = R_s + iX_s\,, \tag{2.12}$$

which can be approximated with [8]

$$\underline{Z}_s \approx \frac{1}{2}\omega^2\mu_0^2\lambda_L^3(T)\sigma_1 + i\omega\mu_0\lambda_L(T)\,. \tag{2.13}$$

2.3 Kinetic Inductance

The well-known geometric inductance can be frequently found in any circuit, even for a segment of strip line, but the magnitude of geometric inductance is determined by the geometry of the circuit. Geometric inductance stores energy in magnetic field and acts as an inertia of charge carriers to the time-varying electric field. The delay of current phase relative to voltage can be considered as a signature of inductive effect, and pure inductive reactance delays the phase of current by 90°. The energy stored in geometric inductor is given by

$$E_m = \int \frac{\mu_0\vec{H}^2}{2} d = \frac{1}{2}L_m I^2\,, \tag{2.14}$$

where $\vec{H}$ is magnetic field stored in the inductor.

As an analogy to geometric inductance, inertia of charge carriers can also result in delay of current phase relative to time-varying electric field. This effect is called kinetic inductance. Kinetic inductance is described by the imaginary part of complex conductivity of a material. Recall Equation 2.1, for normal conductors, relaxation time of charge carriers are very short, therefore, the kinetic inductance will become significant only in THz frequencies or above. Again, at the frequency we are interested in, the kinetic inductance of quasiparticles can be safely neglected. However, the relaxation time of Cooper pairs is infinity, thus leading to finite imaginary part of complex conductivity. Previous studies show that supercurrent has a 90° phase lag relative to electric filed [11], which infers that the reactance of a superconductor stripe is purely inductive. Then the surface impedance of a superconductor can be written as

$$Z_s = R_s + i\omega L_s \,. \tag{2.15}$$

By comparing the above equation to Equation 2.13, surface inductance can be written as

$$L_s = \mu_0 \lambda_L(T) = \mu_0 \sqrt{\frac{m_e}{n_s(T) e^2 \mu_0}} \,. \tag{2.16}$$

As for energy storage, consider the kinetic energy of Cooper pairs with supercurrent density $\vec{J}_s = n_s e \vec{v}_0$,

$$E_{kin} = \int \frac{m_e n_s \vec{v}_0^2}{2} dV = \frac{m_e}{2 n_s e^2} \int \vec{J}_s^2 dV = \frac{1}{2} \frac{m_e}{n_s e^2} \frac{l}{A} I^2 = \frac{1}{2} L_{kin} I^2 \,, \tag{2.17}$$

where $\vec{v}_0$ is the average velocity of the charge carriers, l is the length of the superconductor segment, A is the effective cross-section area, and L_{kin} is kinetic inductance, defined as an analogy to magnetic inductance. The above equation gives the definition of kinetic inductance:

$$L_{kin} = \frac{m_e}{n_s e^2} \frac{l}{A} \,. \tag{2.18}$$

The difference in n_s dependence between kinetic inductance and superconducting surface impedance (Equation 2.16) comes from the effective thickness of the film. Consider a film thickness much larger than London penetration depth, in which case, the height of effective cross section is limited by $\lambda_L(T)$ ($A = \lambda_L(T) w$). Then L_{kin} can be rewritten as

$$L_{kin} = \frac{m_e}{n_s e^2 \lambda_L(T)} \frac{l}{w} = \mu_0 \frac{\lambda_L^2(T)}{\lambda_L(T)} \frac{l}{w} = \mu_0 \lambda_L(T) \frac{l}{w} = L_s \frac{l}{w} \,. \tag{2.19}$$

The surface inductance of a superconductor is therefore related to the kinetic inductance. From this fact, one can conclude that the energy of kinetic inductance is stored in kinetic energy of Cooper pairs. The total inductance of a superconducting circuit is given by the sum of geometric and kinetic inductances:

$$L = L_{kin} + L_m \,. \tag{2.20}$$

2.4 Introduction to Lumped Element Resonators

Lumped element resonators are RLC resonators of dimensions much smaller than the wavelength of the electromagnetic wave at their resonance frequency. In this limit, electromagnetic field over the resonators can be treated as a constant. This is different from the varying electromagnetic field throughout a coplanar waveguide resonator or a 3D cavity. Lumped element resonators can have dimensions of the order of several hundred micrometers at GHz frequencies, while a coplanar waveguide resonator at the same fundamental resonance frequency has a length of several centimeters. Lumped element resonators are therefore space efficient. Furthermore, lumped element resonators also have higher order resonances far away from fundamental resonance, which reduces the possibility of coupling to these unwanted modes. However, both of the advantages come with a price of a lower internal Q factor compared to coplanar waveguide resonators or 3D resonators. A more detailed introduction to lumped element resonators can be found in Antonio Abadal's master thesis [22].

Figure 2.2 shows a typical design of lumped element resonator. The structure is a direct application of LC resonator, where shunt capacitor and meander inductor contribute most of the capacitance and inductance respectively. The resonator is coupled to feed line capacitively through a coupling capacitor. For multi-resonator structure, resonators are typically coupled together through coupling capacitors. When there is only one feed line coupled to a series of resonators, only reflective measurement is possible. If one would like to conduct transmission measurement, a transmission line is required. The reflective design applies to all the samples in this thesis.

An RLC resonator coupled to an external circuit as shown in Figure 2.2 is called a loaded resonator. The circuit model of a loaded RLC resonator is shown in Figure 2.3. In this case, energy in the resonator can either dissipated by resistive loss in the resonator or escape from coupling capacitor to feed line. Energy loss rate is called γ in the former case and κ for the latter case. Typically, the coupling capacitance $C_\kappa \ll C$, the shunt capacitance. In

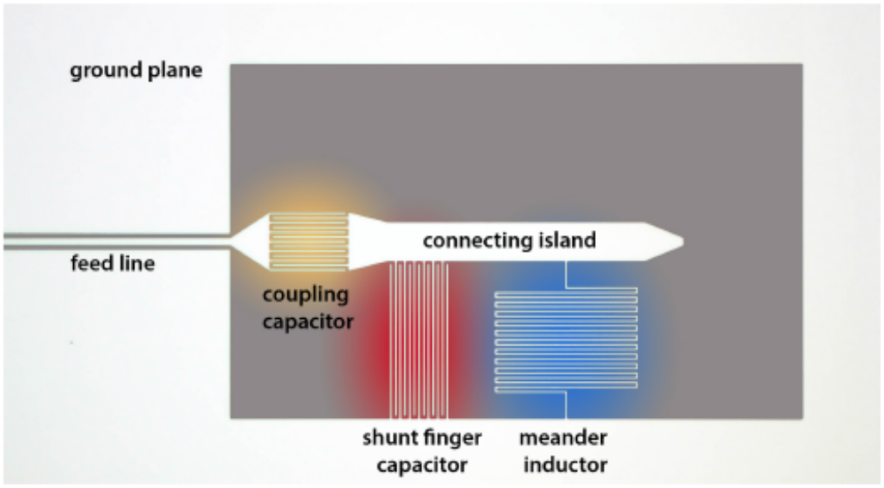

Figure 2.2: A typical design of a single lumped element resonator. Coupling between two resonators is usually done by connecting the coupling capacitor of one resonator to the island of another. [22]

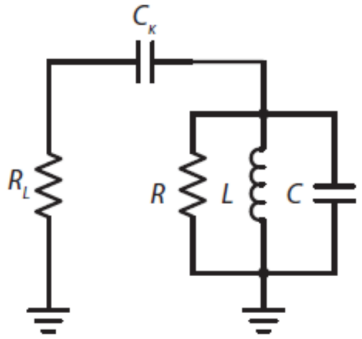

Figure 2.3: Circuit model for a loaded RLC resonator, where R_L is impedance of feed line, and C_κ is coupling capacitance. [22]

this limit, resonance frequency of a loaded RLC resonator is approximately the same as the unloaded case, which is $\omega_0 = 1/\sqrt{LC}$, while loaded Q factor $Q_L = 2\pi \frac{EnergyStored}{EnergyDissipatedPerCycle} = \omega_0 \frac{EnergyStored}{PowerLoss}$ describing the energy loss in the resonator per resonance cycle is given by

$$\frac{1}{Q_L} = \frac{1}{Q_{int}} + \frac{1}{Q_{ext}} = \frac{\gamma}{\omega_0} + \frac{\kappa}{\omega_0}, \tag{2.21}$$

where $Q_{int} = \omega_0/\gamma$ is the internal Q factor, describing the energy loss per cycle through resistive dissipation, and $Q_{ext} = \omega_0/\kappa$ is the external Q factor, describing the energy loss per cycle through coupling capacitor.

Reflection coefficient (Γ) is the ratio between reflected signal and input sig-

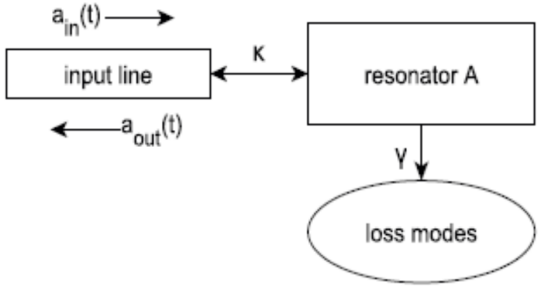

Figure 2.4: Schematic of input-output theory of loaded RLC resonators. [22]

nal, which stores the information of proportion of energy dissipated in the resonator and phase shift of the reflected signal relative to the input one. Measuring reflection coefficient by measuring corresponding S parameter is one of the most important ways to extract information of a reflectively coupled lumped element resonator. The input-output theory of a loaded RLC resonator help us derive Γ theoretically. A schematic of input-output theory is shown in Figure 2.4.

Consider the Hamiltonian of a resonator in linear regime:

$$\mathcal{H} = \hbar\omega_0 \left(\hat{a}^\dagger \hat{a} + \frac{1}{2} \right) , \tag{2.22}$$

where ω_0 is the angular resonance frequency and $\hat{a}^\dagger$, $\hat{a}$ are creation and annihilation operators of the field in the resonator. Then the Heisenberg equation of the system is

$$\dot{\hat{a}}(t) = -\frac{i}{\hbar}[\hat{a}(t), \mathcal{H}] - \frac{\kappa + \gamma}{2}\hat{a}(t) + \sqrt{\kappa}\hat{a}_{in}(t) , \tag{2.23}$$

after Fourier transform to frequency domain, we have

$$-i\omega\hat{a}(\omega) = -i\omega_0\hat{a}(\omega) - \frac{\kappa + \gamma}{2}\hat{a}(\omega) + \sqrt{\kappa}\hat{a}_{in}(\omega) . \tag{2.24}$$

Together with input-output relation

$$\hat{a}_{in}(\omega) + \hat{a}_{out}(\omega) = \sqrt{\kappa}\hat{a}(\omega) , \tag{2.25}$$

the reflection coefficient can be derived as

$$\Gamma = \frac{\hat{a}_{out}(\omega)}{\hat{a}_{in}(\omega)} = \frac{\sqrt{\kappa}\hat{a} - \hat{a}_{in}}{\hat{a}_{in}} = \frac{\kappa}{-i(\omega - \omega_0) + \frac{\kappa+\gamma}{2}} - 1\,, \tag{2.26}$$

Reflection coefficient depends on signal frequency, resonance frequency, coupling to feed line and internal loss of the resonator. In practice, the derivation above is correct up to an arbitrary phase factor $e^{i\varphi}$.

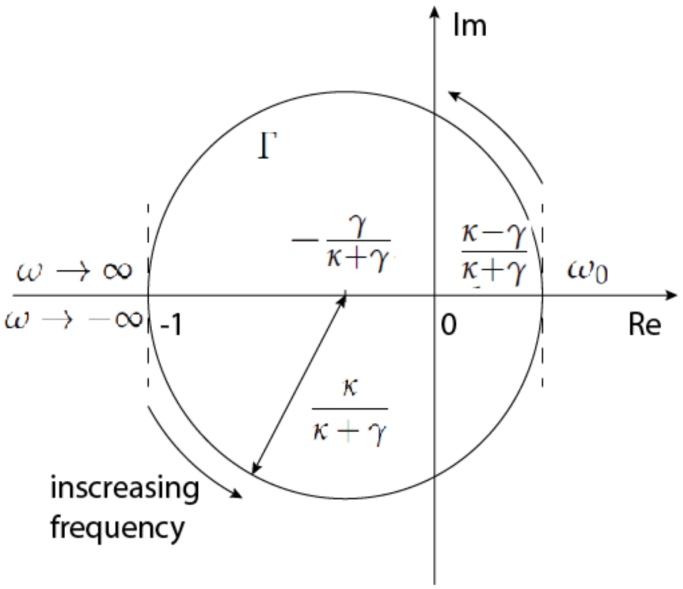

Figure 2.5: Reflection coefficient on complex plane. In practice, there can be an arbitrary phase shift.

Please notice that reflection coefficient Γ is a complex quantity. When signal frequency is infinitely far from resonance frequency, the amplitude of Γ is 1, and corresponds to the point $(-1, 0)$ on the complex plane. When signal frequency is at resonance, Γ corresponds to the point at $(\frac{\kappa-\gamma}{\kappa+\gamma}, 0)$. When $\kappa > \gamma$, resonance point is on the positive side of real axis, then we say the resonator is overcoupled, because leaking into feed line is the more important energy losing channel. On the contrary, when $\kappa < \gamma$, we say the resonator is undercoupled. In the case $\kappa = \gamma$, we call the resonator critically coupled, where the reflection coefficient at resonance drops to 0. We can rewrite Γ into a form of well separated real and imaginary part

$$\Gamma = \frac{\kappa(\kappa+\gamma)/2}{(\omega - \omega_0)^2 + \frac{1}{4}(\kappa+\gamma)^2} - 1 + i\frac{\kappa(\omega - \omega_0)}{(\omega - \omega_0)^2 + \frac{1}{4}(\kappa+\gamma)^2}\,. \tag{2.27}$$

The distance between any point on the path of Γ on the complex plane and the middle point between far off resonance and on resonance $(\frac{1}{2}(\frac{\kappa-\gamma}{\kappa+\gamma}-1),0)=(-\frac{\gamma}{\kappa+\gamma},0)$ can be calculated as

$$\begin{aligned}
Distance =& \sqrt{\left(Re(\Gamma)-\left(-\frac{\gamma}{\kappa+\gamma}\right)\right)^2+Im^2(\Gamma)} \\
=& \left(\left(\frac{\kappa(\kappa+\gamma)/2}{(\omega-\omega_0)^2+\frac{1}{4}(\kappa+\gamma)^2}-1-\left(-\frac{\gamma}{\kappa+\gamma}\right)\right)^2+\left(\frac{\kappa(\omega-\omega_0)}{(\omega-\omega_0)^2+\frac{1}{4}(\kappa+\gamma)^2}\right)^2\right)^{\frac{1}{2}} \\
=& \left(\left(\frac{\kappa(\kappa+\gamma)/2}{(\omega-\omega_0)^2+\frac{1}{4}(\kappa+\gamma)^2}-\frac{\kappa}{\kappa+\gamma}\right)^2+\left(\frac{\kappa(\omega-\omega_0)}{(\omega-\omega_0)^2+\frac{1}{4}(\kappa+\gamma)^2}\right)^2\right)^{\frac{1}{2}} \\
=& \left(\frac{\kappa^2}{(\kappa+\gamma)^2}+\frac{1}{4}\frac{\kappa^2(\kappa+\gamma)^2}{\left((\omega-\omega_0)^2+\frac{1}{4}(\kappa+\gamma)^2\right)^2}\right. \\
& \left.-\frac{\kappa^2\left((\omega-\omega_0)^2+\frac{1}{4}(\kappa+\gamma)^2\right)}{\left((\omega-\omega_0)^2+\frac{1}{4}(\kappa+\gamma)^2\right)^2}+\frac{\kappa^2(\omega-\omega_0)^2}{\left((\omega-\omega_0)^2+\frac{1}{4}(\kappa+\gamma)^2\right)^2}\right)^{\frac{1}{2}} \\
=& \frac{\kappa}{\kappa+\gamma},
\end{aligned} \tag{2.28}$$

which is a constant. Therefore, the path of Γ on complex plane is an arc. In addition, it is easy to see for $\omega\to\infty$ and $\omega\to-\infty$ the phases differ by 2π, so the path of Γ is actually a circle. Figure 2.5 displays Γ on the complex plane.

In practice, we measure the voltage of reflected signal from sample V_{out}, and reflection coefficient can be calcualted by using equation $\Gamma=V_{out}/V_{in}$. However, due to phase shift and optical length difference between signal arm and reference arm, measured reflection coefficient usually differs from what is shown in Figure 2.5. The effect of phase shift and optical length difference can be summarized in a phaser $e^{i(\omega\tau_{opt}+\varphi)}$, where τ_{opt} is the optical delay due to finite optical length difference, and φ is the phase shift. Then the measured reflection coefficient is

$$\Gamma=\left(\frac{\kappa}{-i(\omega-\omega_0)+\frac{\kappa+\gamma}{2}}-1\right)e^{i(\omega\tau_{opt}+\varphi)}. \tag{2.29}$$

The effect of finite optical length difference is shown in Figure 2.6. When τ_{opt} is negative, the path of Γ is closed, and has two arms at frequencies away

from resonance. When τ_{opt} is positive, the path of Γ is open, and has two arms, too. The connecting points of arm and circle correspond to a sudden change in phase for both cases. Optical length difference has to be corrected before analyzing complex reflection coefficient data.

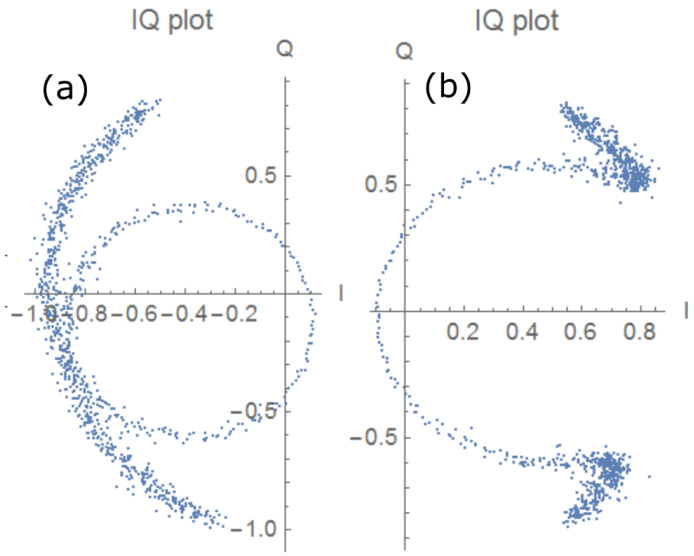

Figure 2.6: Reflection coefficient with (a) negative and (b) positive optical length.

In practice, the amplitude of reflection coefficient ($|\Gamma|$) is sometimes measured instead of complex reflection coefficient. Measuring $|\Gamma|$ does not require reference arm, and is free from any phaser problem. $|\Gamma|$ is given by

$$|\Gamma| = \sqrt{1 - \frac{\kappa\gamma}{(\omega - \omega_0)^2 + \left(\frac{\kappa+\gamma}{2}\right)^2}}, \tag{2.30}$$

where the second term in square root is a Lorentzian function. In the above equation, the roles of κ and γ are symmetric, which forbids extracting γ and κ deterministically from $|\Gamma|$ data without extra information. Increasing either γ or κ broadens the Lorentzian function, and thus broadens the dip in $|\Gamma|$ spectrum around resonance frequency.

2.5 Interaction between Light and Superconductor

Laser scanning microscopy is based on laser-induced local changes of materials, in our case superconductor's electric properties.

The laser used in this thesis has a wavelength of 405 nm, with single photon

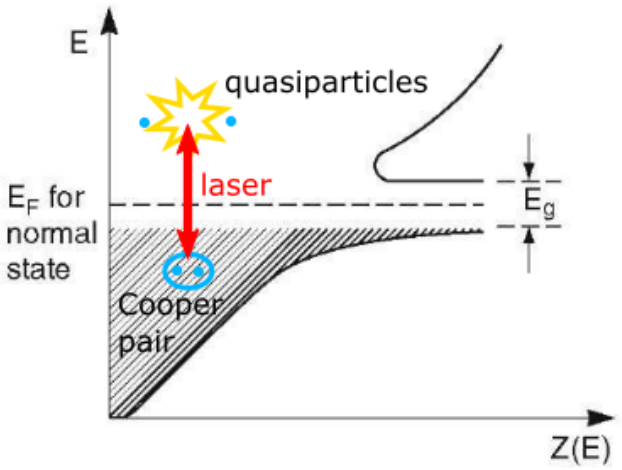

Figure 2.7: Photons with energy above superconductor energy gap can be absorbed by superconductor, and breaks Cooper pairs into quasiparticles. Z(E) is density of state as a function of energy. [23]

energy of 4.9 eV. The typical gap energy of pure superconducting Niobium at zero temperature is 2.9 meV [24], which is much smaller than a single photon energy. When the single photon energy is above twice of the gap energy in the superconductor, a part of photons shining on superconductor will be absorbed and break Cooper pairs into quasiparticles. Due to electron-electron, electron-phonon interaction and direct Stokes-like depairing, the high energy quasiparticles generated by photon will subsequently break other Cooper pairs quickly, until the energy of the absorbed photon is evenly distributed to n quasiparticles. The maximum number of created quasiparticles from a single photon with frequency ν is $n = h\nu/E_g$, where h is Planck constant and E_g is the gap energy of superconductor [3]. Within the model explained in previous sections, the effect of laser can be considered as a change of the density of Cooper pairs and quaisparticles either by breaking the Cooper pairs or possibly by heating the sample. In the latter case, the temperature dependence of superconducting gap and more thermal energy will lead to change of number of thermally excited quasiparticles as a function of temperature.

Both absorption of photon and heating of the sample increase the density of quasiparticles and decrease the density of Cooper pairs. For Equation 2.5, laser increases the real part of the complex conductivity, and decreases the imaginary part. The increasing real part of complex conductivity leads to the increase of electric loss, and thus the decrease of internal Q factor. The effect of decreasing imaginary part of conductivity can be seen by looking at the kinetic inductance given by Equation 2.16 and 2.17, which show that

laser enhances kinetic inductance of a resonator, thus increases total inductance. The shift of inductance can be detected by measuring the resonance angular frequency of a resonator, which is given by

$$\omega_0 = \frac{1}{\sqrt{LC}}, \tag{2.31}$$

when L increases, the resonance frequency will decrease. Photo response in a superconducting resonator can be summarized as decreasing of resonance frequency and internal Q factor.

A significant usage of LSM is to probe current density distribution. Previous researchers such as Newman and Zhuravel pointed out that inductive photo response in terms of change in S parameter is proportional to J^2, where J is local current density at laser probe [8, 1]. However, there is no formula available for the magnitude of laser-induced kinetic inductance change. In this thesis, we developed a model of laser-induced kinetic inductance change (resonance frequency shift) for general microwave superconducting devices. Recall Equation 2.17, the expression of kinetic energy of Cooper pairs related to kinetic inductance, where the integration is overall volume with finite super current density. If there is a laser shining on a position with super current density, we can rewrite Equation 2.17 as

$$E_{kin} = \frac{m_e}{2e^2}\int \frac{1}{n_s} J_s^2 dV = \frac{m_e}{2e^2}\left(\int_{rest} \frac{1}{n_s} J_s^2 dV + \int_{V_{laser}} \frac{1}{n_s^*} J_s^2 dV\right), \tag{2.32}$$

where the second integral is over the volume where n_s is changed by laser, the first integral is over the volume other than V_{laser} with finite current density. The laser-modified superconducting electron density is indicated as n_s^*. We can subsequently rewrite E_{kin} as original kinetic energy of Cooper pairs E_{kin0} in the whole circuit, and the laser-induced change ΔE_{kin}

$$\begin{aligned} E_{kin} &= \frac{m_e}{2e^2}\left(\int \frac{1}{n_s} J_s^2 dV + \int_{V_{laser}} \left(\frac{1}{n_s^*} - \frac{1}{n_s}\right) J_s^2 dV\right) \\ &= E_{kin0} + \frac{m_e}{2e^2}\int_{V_{laser}} \frac{\Delta n_s}{n_s(n_s - \Delta n_s)} J_s^2 dV = E_{kin0} + \Delta E_{kin}, \end{aligned} \tag{2.33}$$

where $\Delta n_s = n_s - n_s^*$ is the laser-induced change in superconducting electron density. Then the ratio between E_{kin0} and ΔE_{kin} has the relation

$$\frac{\Delta L_{kin}}{L_{kin0}} = \frac{\frac{1}{2}\Delta L_{kin} I^2}{\frac{1}{2} L_{kin0} I^2} = \frac{\Delta E_{kin}}{E_{kin0}} = \frac{\frac{m_e}{2n_s e^2}\int_{V_{laser}} \frac{\Delta n_s}{n_s - \Delta n_s} J_s^2 dV}{\frac{m_e}{2n_s e^2}\int J_s^2 dV}. \tag{2.34}$$

We assume that change of n_s is uniform over the laser spot, then the local change in n_s will be independent from spatial position. We can take $\frac{\Delta n_s}{n_s - \Delta n_s}$ out of the integral and get

$$\begin{aligned}\frac{\Delta L_{kin}}{L_{kin0}} &= \frac{\Delta n_s}{n_s - \Delta n_s}\frac{\int_{V_{laser}} J_s^2 dV}{\int J_s^2 dV} = \frac{\Delta n_s}{n_s - \Delta n_s}\frac{\int t f_{laser}(x,y) J_s^2 dxdy}{\int t J_s^2 dxdy} \\ &= \frac{\Delta n_s}{n_s - \Delta n_s}\frac{\int f_{laser}(x,y) J_s^2 dxdy}{\int J_s^2 dxdy} = \frac{\Delta n_s}{n_s - \Delta n_s} F_{laser}(x,y)\,,\end{aligned} \tag{2.35}$$

where t is the effective thickness of the film, f_{laser} is a function with value 1 in the area influenced by laser and 0 elsewhere, and F_{laser} is a position dependent function. The numerator of F_{laser} is governed by local current density square $f_{laser}(x,y)J_s^2$, which is consistent with the conclusion of previous works. But the denominator renormalizes $F_{laser}(x,y)$ with average J_s^2 over the whole volume with finite current density. Assuming current density distribution is independent of total current flowing through the superconductor, F_{laser} is independent of total current, in this sense, $F_{laser}(x,y)$ is the participation ratio of the part of superconductor illuminated by laser. From Equation 2.35, we can see that when laser probes on somewhere without current density, there will be no change in kinetic inductance of the resonator. This result not only holds for position on ground plane away from resonator, but also holds for resonators in dark state of some certain resonance mode of a chain/circle of coupled resonators. Equation 2.35 would be a crucial guide if one would like to tune the resonance frequency of a resonator with laser.

Previous researchers also pointed out that internal loss photo response in terms of change in S parameter is proportional to J^2, where J is the local current density at the laser probe [3, 1]. Let's call photo-induced resistive change in S parameter PR_R. As S parameter is proportional to energy, resistive photo response in terms of S parameter is

$$PR_R \propto J^2(x_0, y_0)\delta R(x_0, y_0)\,, \tag{2.36}$$

where right hand side is photo-induced change in resistive energy dissipation, and $\delta R(x_0, y_0)$ is position dependent photo-induced change in total resistance. For a laser probe at position l_0, $\delta R(l_0)$ can be described by

$$\delta R(l_0) \propto \frac{\pi\Lambda}{4wl}\int_{\not\perp} dl \frac{\partial R(l_0)}{\partial J(l_0)}\frac{\partial J(l_0)}{\partial P_L}\delta P_L(l_0)\,, \tag{2.37}$$

where P_L is laser power, δP_L is the portion of laser power absorbed by superconductor, integral is over a path $\not{L}$ along the whole inductor line, and Λ is the characteristic healing length describing spatial decay of $PR_R(l_0) \propto e^{-|l-l_0|/\Lambda}$ at a distance l from laser spot. However, Zhuravel and his colleagues did not give the formula of $\frac{\partial R(l_0)}{\partial J(l_0)} \frac{\partial J(l_0)}{\partial P_L}$, which prevents us from studying laser-induced change in resistance quantitatively using Equation 2.37.

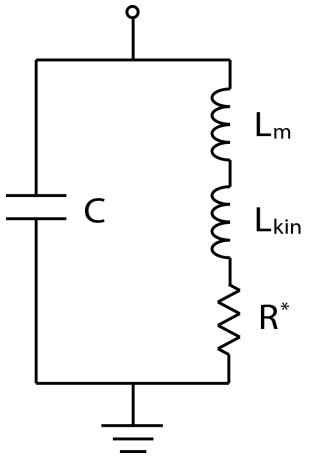

Figure 2.8: The circuit model of an unloaded parallel superconducting lumped element resonator. In the figure, C is capacitance, L_m is geometric inductance, L_{kin} is kinetic inductance, and R^* is effective resistance given by two-fluid model.

In this thesis, we developed a model of laser-induced change in resistive loss specifically for superconducting lumped element resonators, using similar procedure as kinetic inductance case. In an RLC resonator, resistive loss is characterized by energy loss rate $\gamma = \frac{PowerLoss}{EnergyStored}$, as defined in Section 2.4. Our model primarily describes γ instead of resistance, as γ is a more relevant quantity in the context of resonators.

Figure 2.8 shows the circuit model of an unloaded parallel superconducting lumped element resonator. R^*, the effective resistance given by two-fluid model, is determined by real part of Equation 2.13 and aspect ratio, and L_{kin}, the kinetic inductance, by imaginary part and aspect ratio. The equation of motion of this circuit can be derived using voltage crossing every element. The voltage equation is

$$V_C + V_{L_m} + V_{L_{kin}} + V_{R^*} = 0\,. \tag{2.38}$$

By substituting $V_C = Q/C$, $V_{L_m} = L_m \dot{I}$, $V_{L_{kin}} = L_{kin}\dot{I}$, and $V_{R^*} = R^* I$, we have

$$\frac{Q}{C} + L_m\dot{I} + L_{kin}\dot{I} + R^*I = 0\,. \tag{2.39}$$

Taking derivative once with respect to time, we get equation of motion

$$\ddot{I} + \frac{R^*}{L_m + L_{kin}}\dot{I} + \frac{1}{(L_m + L_{kin})C}I = \ddot{I} + \gamma\dot{I} + \omega_0^2 I = 0\,. \tag{2.40}$$

Then we have loss rate of the unloaded circuit. In the regime of $C_\kappa \ll C$, we have $\gamma \approx \frac{R^*}{L_m + L_{kin}}$ as total internal loss rate of the resonator. For a film with thickness larger than London penetration depth, we have

$$\begin{aligned} R^* &= \frac{1}{2}\frac{l}{w}\omega^2\mu_0^2\lambda_L^3(T)\sigma_1 \\ &= \frac{1}{2}\frac{l}{w}\omega^2\mu_0^2\lambda_L^3(T)\frac{(n-n_s)e^2\tau}{m_e(1+\omega^2\tau^2)} \propto n_s^{-3/2}(n-n_s)\,, \end{aligned} \tag{2.41}$$

where $\frac{l}{w}$ is the aspect ratio of the lumped element resonator, and

$$L_{kin} = \mu_0\lambda_L(T)\frac{l}{w} \propto n_s^{-1/2}\,. \tag{2.42}$$

So energy loss rate γ is

$$\gamma = \frac{\frac{1}{2}\frac{l}{w}\omega^2\mu_0^2\lambda_L^3(T)\frac{(n-n_s)e^2\tau}{m_e(1+\omega^2\tau^2)}}{L_m + \mu_0\lambda_L(T)\frac{l}{w}} \propto \frac{n-n_s}{L_m n_s^{3/2} + a n_s}\,, \tag{2.43}$$

where $a = \sqrt{\frac{m_e\mu_0}{e^2}}\frac{l}{w}$. γ is a monotonically decreasing function of n_s.

Laser-induced change in γ is more complicated than simply taking a derivative of γ with respective to n_s, because of the position dependent laser-induced change. To see this, we refer to the definition of energy loss rate $\gamma = \frac{PowerLoss}{EnergyStored}$. As the energy stored in resonator is independent from laser probe, the ratio between $\Delta\gamma$ and γ is

$$\frac{\Delta\gamma}{\gamma} = \frac{\Delta P_R}{P_R}\,, \tag{2.44}$$

where P_R is energy dissipation power, given by

$$P_R = R^*I^2 = \frac{\rho^* l}{A}(JA)^2 = \rho^* l J^2 A = \rho^* J^2 V\,, \tag{2.45}$$

where A is cross section area, l is resistor length, and $\rho^* = R^* l / A$ is effective resistivity. Rewrite P_R in the form of integrating $\rho^* J^2$ over the whole volume with finite current density, we have

$$P_R = \int \rho^* J^2 dV = \int_{V_{rest}} \rho^* J^2 dV + \int_{V_{laser}} \rho^{*'} J^2 dV \,, \tag{2.46}$$

where $\rho^{*'}$ is laser-influenced resistivity, V_{laser} is the volume influenced by laser probe, A_{laser} is the cross section of laser-influenced volume, and V_{rest} is the volume free from laser influence. Assume small laser-induced change in n_s, we have

$$\begin{aligned} P_R &= \int \rho_0^* J^2 dV + \int_{V_{laser}} \Delta\rho^* J^2 dV \\ &= b \int \frac{1}{t} n_s^{-3/2} (n - n_s) J^2 dV - b \int_{V_{laser}} \frac{1}{2t} \Delta n_s n_s^{-3/2} \left(3\frac{n}{n_s} - 1 \right) J^2 dV \\ &= P_{R0} + \Delta P_R \,, \end{aligned} \tag{2.47}$$

where ρ_0^* is unmodified effective resistivity, P_{R0} is unmodified energy dissipation power, t is effective film thickness, $b = \frac{1}{2}\sqrt{m_e \mu_0} \frac{\omega^2 \tau}{1+\omega^2\tau^2}$ is a factor independent from n_s. Then the ratio between $\Delta\gamma$ and γ is

$$\begin{aligned} \frac{\Delta\gamma}{\gamma} = \frac{\Delta P_R}{P_R} &= \frac{-b \int_{V_{laser}} \frac{1}{2t} \Delta n_s n_s^{-3/2} \left(3\frac{n}{n_s} - 1 \right) J^2 dV}{b \int \frac{1}{t} n_s^{-3/2} (n - n_s) J^2 dV} \\ &= -\frac{\Delta n_s (3n - n_s)}{2 n_s (n - n_s)} \frac{\int_{S_{laser}} J^2 dx dy}{\int J^2 dx dy} \\ &= -\frac{\Delta n_s (3n - n_s)}{2 n_s (n - n_s)} \frac{\int f_{laser}(x,y) J^2 dx dy}{\int J^2 dx dy} \\ &= -\frac{\Delta n_s (3n - n_s)}{2 n_s (n - n_s)} F_{laser}(x,y) \,, \end{aligned} \tag{2.48}$$

where S_{laser} is the area of laser spot, and $f_{laser}(x,y)$ and $F_{laser}(x,y)$ are defined the same as in Equation 2.35. $\Delta\gamma$ shares the same position dependence as ΔL_{kin}. Please notice that $F_{laser} \propto \int f_{laser}(x,y) J^2 dx dy$, which is consistent with Equation 2.36. However, similar to ΔL_{kin}, $\Delta\gamma$ is independent from total current flowing through inductor to the first order.

Chapter 3

Measurement of Photo Response

In the first part of this chapter, the general experimental setup will be introduced. The second part introduces 4 possible methods of measuring photo response, where the theory and implementation of which are discussed in detail. Not all of the methods are suitable for extracting laser-induced changes in resonance frequency and internal Q factor of resonators at current stage. At the end of this chapter, noise analysis of reflection coefficient measurement will be discussed.

3.1 General Experimental Setup

Laser scanning microscopy combines measurements with both microwave and optical setup. For some of the measurement tasks, the microwave and optical parts are independent from each other, while for other tasks synchronization of the two parts is required. In this section, microwave and optical setup are introduced separately.

3.1.1 Optical Setup

Optical setup for LSM provides intensity modulated laser, required for the photo response measurements. Optical setup can also get optical images of sample, which is helpful for identifying position of the probe.

Figure 3.1 shows a schematic of the optical setup. Laser generated by a commercial laser diode CS4051205X has wavelength 405 nm. After reflected by two mirrors (due to historical reason, the first mirror is a dichroic, which reflects short wavelength light and transmit long wavelength one), the laser beam is fed to an acousto-optic modulator (AOM). In AOM, a piezo-generated acoustic standing wave changes the refractive index of the optical media periodically in space. Then the Bragg diffraction splits incoming laser beam into several beams with angle θ from 0th order beam given by

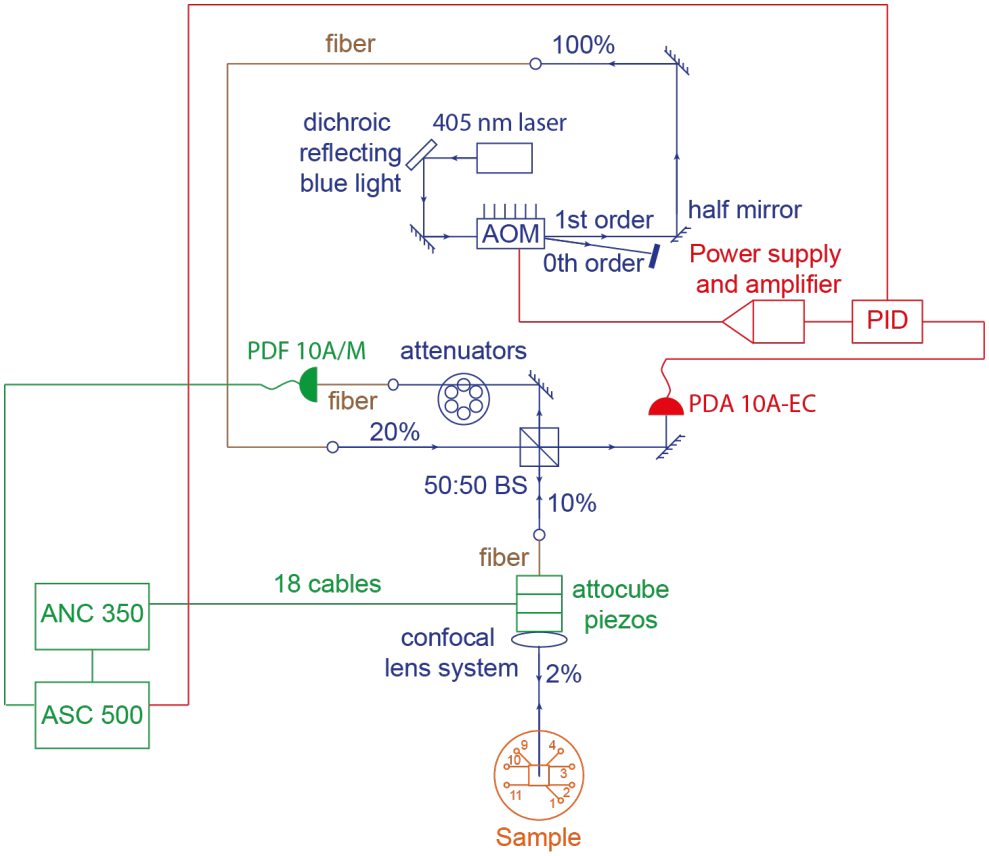

Figure 3.1: The schematic of optical setup of LSM experiment. Laser generated by the laser diode is split into 0th order and higher order beams by AOM. By modulating the voltage amplitude driving AOM, we can modulate the intensity of higher order beams. In our case, beams of order higher than 1 are dim enough to be neglected. PDF and PDA are avalanche photon detectors. The signal from PDA is fed to a PID controller to stabilize laser intensity by tuning the modulation amplitude of AOM. PDF is used to detect reflected light from sample. The percentages indicated besides laser beam specifies the ratio of laser power at current position to the power before the first laser coupler.

$$sin\theta = \frac{m\lambda}{\Lambda}, \tag{3.1}$$

where $m = ..., -2, -1, 0, +1, +2, ...$, λ is the wavelength of laser light, and Λ is the wavelength of sound. By modulating the amplitude of acoustic wave, one can modulate the laser intensity with a frequency up to 100 MHz [25]. In general, the amplitude of laser intensity of the first order beams can range from 0% to 80% of total input intensity, while the maximum intensity of higher order beams are much lower. In this thesis, we use 1st order beam only, and 0th order beam is discarded and blocked at a half mirror. The first order beam is subsequently coupled to a fiber coupler, which helps filtering

out higher oder beams. Then the laser beam is split at a 50:50 beam splitter. The transmitted beam is fed to an avalanche photon detector PDA 10A-EC. The signal from the detector is fed to a PID controller, which controls AOM in order to stabilize the laser intensity. The reflected beam at the beam splitter goes into the fridge, where the beam shines on the sample through a confocal lens system, whose X, Y, and Z position are controlled by Attocube piezos. One can thus move laser spot in plane and out of plane for focusing. Reflected light from the sample propagates back to the beam splitter. The transmitted part is attenuated and fed to a highly sensitive avalanche photon detector PDF 10A/M, whose signal is fed to ASC 500 box (Attocube Scanner Controller), and subsequently passed to Daisy software in lab computer. With the reflection signal, one can conduct optical mapping of the sample. ANC 350 box is the position controller for the confocal lens system. ASC 500 box is the scanning controller, which via ANC 350 performs a 2D scanning.

There are two modes of Attocube positioners. One is stepper, designed for wide range movement of the object attached to the positioner. X and Y Steppers cover a 4 mm $\times$ 4 mm area. The other is scanner, designed for fine movement. X and Y scanner cover a 40 μm $\times$ 40 μm area. The working principle of stepper is shown in Figure 3.2. The confocal lens system is attached to the clamped table. A sawtooth voltage is used to control the position of the clamped table. From Time 1 to Time 2, the piezoelectric actuator expands slowly, with the clamped table following the motion of the guiding rod. From Time 2 to Time 3, the piezoelectric actuator contracts suddenly. Due to inertia, the clamped table stays at position at Time 2, while the guiding rod goes back to the position at Time 1. In a period of sawtooth voltage, the clamped table is moved to the right by Δx. The working principle of scanner is more straightforward. By applying unipolar DC voltage on the piezo elements, the scanner controls the expansion of the piezo element. The expansion is amplified by integrated flexure structures, so that scanners can cover a much larger area.

3.1.2 Microwave Setup

A schematic of microwave setup is shown in Figure 3.3. The corresponding attenuation or gain of a device is indicated in unit dB. Two SMB 100A low noise RF microwave signal generators are used to as microwave signal source. One is connected to LO port of an IQ mixer, acting as LO signal. Microwave generated by the other generator is fed to sample in fridge. The reflected signal from sample is fed to RF port of the IQ mixer, after a linear amplification chain. The RF frequency and the LO frequency differ by Δf. After the down conversion at the IQ mixer, IQ quadratures have frequency Δf. I or Q quadrature is then amplified again and fed to either field-programmable gate array (FPGA) or ASC 500 box, where it is measured and

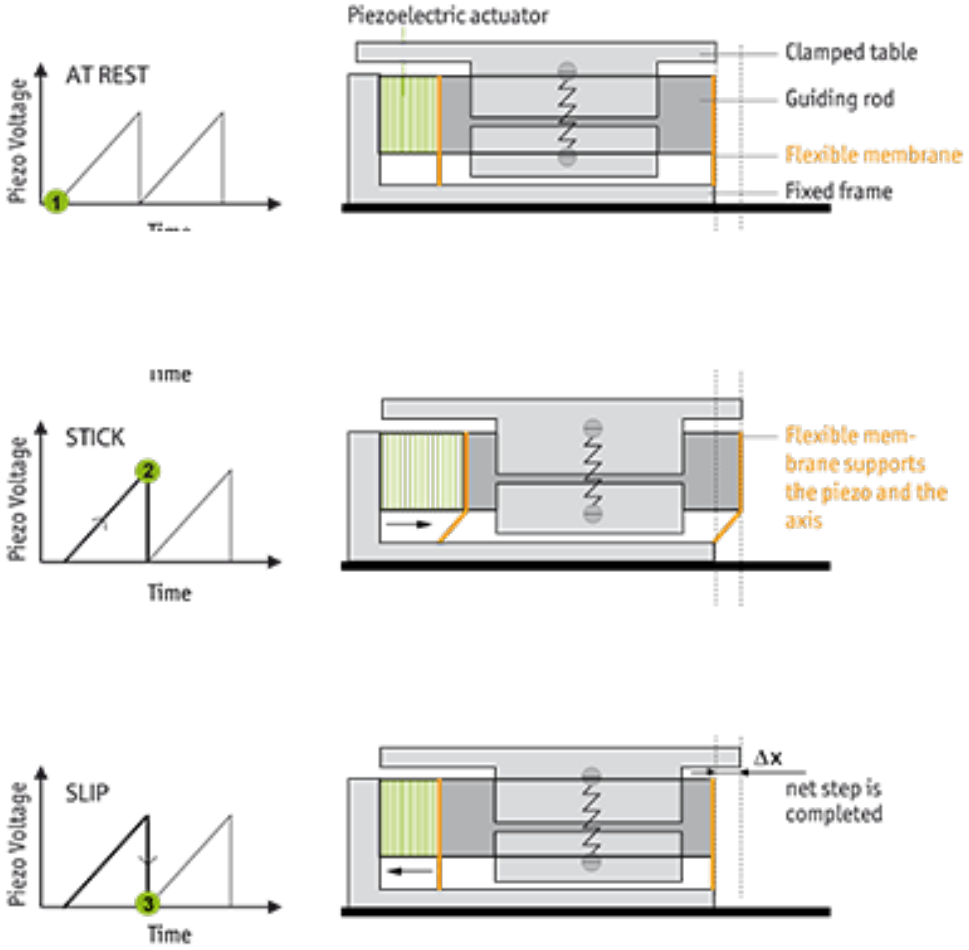

Figure 3.2: The working principle of Attocube Stepper. From Time 1 to Time 2, the piezoelectric actuator expands slowly, without relative movement between the clamped table and the guiding rod. From Time 2 to Time 3, the piezoelectric actuator contracts suddenly, and pulls out the guiding rod from the clamped table. The clamped table stays at the position at Time 2 due to inertia. From Time 1 to Time 3, the position of the clamped table moves to the right by Δx. [26]

analyzed. We will choose $\Delta f = 250$ MHz, if we use FPGA. Because in Virtex 6 FPGA, the 250 MHz signal is digital down-converted to DC with a build-in LO signal. We choose $\Delta f = 0$ if we use ASC 500 box to measure photo response. In this case, I or Q quadrature carries a signal with frequency of laser modulation (due to photo response).

DC blocks are used to prevent ground loops. The directional couplers in the fridge are used to separate incoming and outgoing signals from the resonator, or incoming and outgoing signals will form standing wave in the

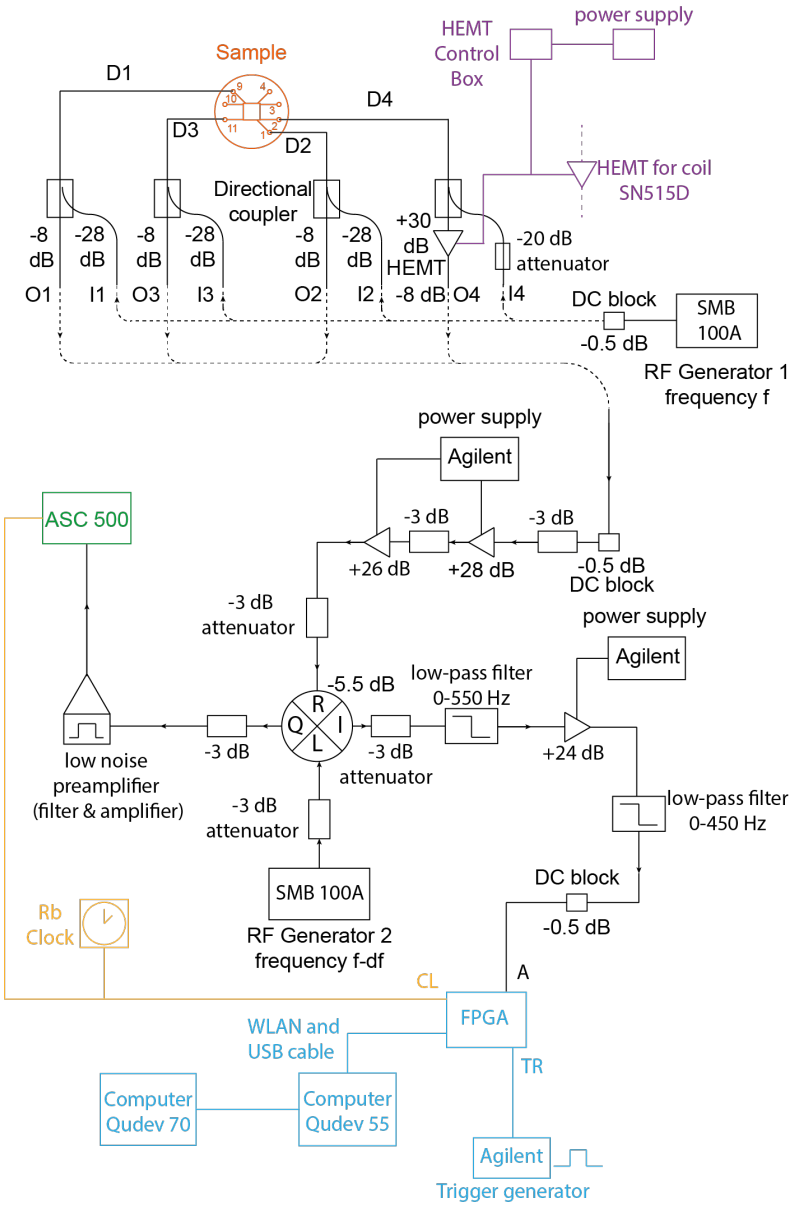

Figure 3.3: The schematic of microwave setup of LSM experiment. Please see the text for details.

cable, which is harmful to measurement. To reduce thermal noise, the attenuator, the directional coupler, and the high-electron-mobility transistor (HEMT) are thermalized to 3 K. A detailed calculation of noise can be found in Section 3.4. The attenuators on amplification chain are used to reduce the effect of standing waves. In frequency domain (which is the case for spectrum measurement using FPGA), standing waves with different frequencies act like harmonic oscillators as a function of frequency, which significantly

influences measured spectrum. Attenuators can reduce the standing waves (an analogy of increasing γ in reflection coefficient), so that the base line becomes effectively flat in the region we are interested in. Low pass filters on amplification chain connected to FPGA are used to filter out high frequency noise. The band pass filter built in the low noise preamplifier connected to ASC 500 box filters out both high frequency and low frequency noise. The Rb clock is used to synchronize devices, so that they have the same time reference. The trigger generator (an arbitrary waveform generator (AWG)) is used to trigger the FPGA measurements.

3.2 Signal Processing in FPGA

A field-programmable gate array (FPGA) is an integrated circuit designed for fast measurement and processing of data. As indicated by its name, the function of FPGA is programmable by the user. In Qudev Lab, the labview file used to control FPGA is called Cleansweep. There are several applications in Cleansweep, in this study we used "Correlator" only. More detailed introduction to FPGA and Cleansweep can be found in Qudev wiki in FPGA section.

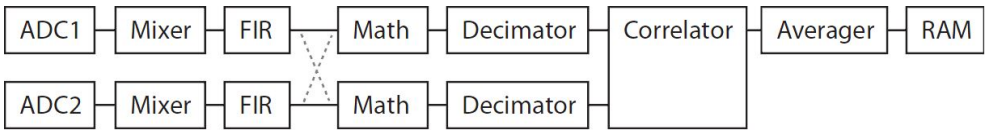

Figure 3.4: The schematic of signal processing pipeline in our FPGA design.

Figure 3.4 shows the signal processing pipeline in our FPGA design. The input signal is detected and converted to digital number by ADCs (analog-to-digital converter) at the beginning of the processing chain. At the mixer, the signal is digital down-converted, with a local oscillator at frequency 250 MHz in our case. Digital down conversion is able to recover amplitudes of I and Q quadratures with just one input. After the down conversion is the real symmetric finite impulse response (FIR), which is a digital filter, designed to filter out noise at undesired frequency. Though the properties of the first three steps can be controlled from Cleansweep, they were kept the same during the study. The digital down-conversion produces two quadratures from one input signal. Signal math function (indicated as "Math" in the pipeline) determines how the two quadratures are mixed to get a single signal.

Figure 3.5 shows a screen shot in Cleansweep and schematic in FPGA of the signal math control tap. In the tap, one can choose the definition of signal a and b, the product of which is the output of the signal math section, which are named s_A and s_B for signal from different ADCs. Please notice

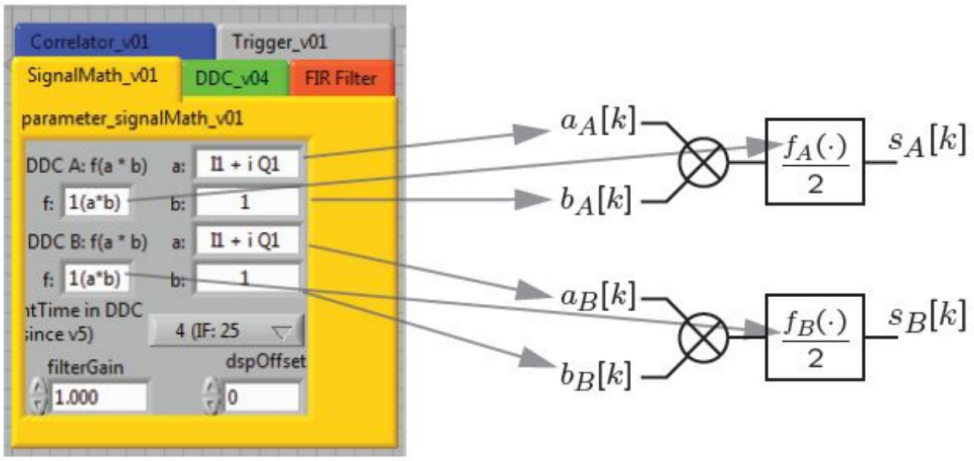

Figure 3.5: Schematic of SignalMath v01 tap in Cleansweep, which controls how FPGA proceeds I and Q quadratures from digital down-conversion. DDC is an abbreviation of digital down-conversion.

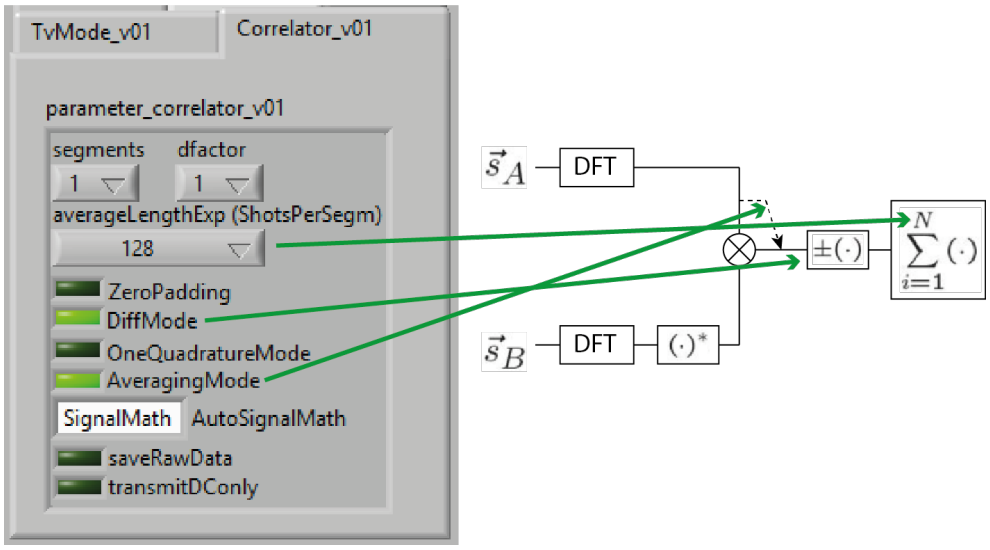

Figure 3.6: Schematic of correlator and averager.

that s_A and s_B are complex in general. The decimator following signal math processing allows one to discard some of the data in a series of repeating measurement. In this thesis, all data points are kept. The Correlator and Averager do the final signal processing before it is written in to RAM.

Figure 3.6 shows the schematics of Correlator and Averager. In the Correlator, the two signals from signal math section are first fast Fourier transformed, and then s_B is converted to its complex conjugate. The two signals are then multiplied at a multiplier. The Averager sums up the result of N

repeating measurements, where N is specified by "averageLengthExp" option under the Correlator tap in Cleansweep. One can choose to turn on and off some functions of the Correlator and Averager on the control panel in Cleansweep. "dfactor" and "ZeroPadding" are used to control decimator. When "DiffMode" is on, FPGA flip the sign of the product of s_A and s_B every other repetition, so that the summation in Averager is the summation of differences between two adjacent measurements. "DiffMode" is the key to measuring photo response by FPGA. When "AveragingMode" is on, s_B is discarded, and Averager calculates the average of N repetitions of s_A, instead of the summation. As we only have one input signal to FPGA, "AveragingMode" is always on during the study. If there is input to the ADC 2, it is possible to measure first order and second order correlation function. This is where the name of the application "Correlator" comes from.

It is beneficial to clarify the concept "one measurement of FPGA" at this point. When FPGA receives a trigger, it measures 8192 points in 8.192 μs, i.e. 1 ns per point, and processes the data before the next trigger. The action corresponds to one trigger pulse is called a "measurement". Limited by the proceeding time, the period of a trigger cannot be as short as the length of the measurement time window. The lower limit of trigger period is around 10 μs in case of Virtex 6 FPGA.

3.3 Measurement of Photo Response

In the previous sections the general experimental setup and the signal processing of FPGA are introduced. Now, we discuss here the measurement of photo response of the lumped element resonators. As pointed out in Chapter 2, irradiation of laser increases the number of quasiparticles in the resonator, thus increases loss rate (γ) and local kinetic inductance. The increasing γ will broaden the dip in resonance profile, and the increasing kinetic inductance will red-shift the resonance frequency (i.e. shift the dip of reflection coefficient to lower frequency). The photo response can be obtained by measuring the changes induced by laser irradiation. Based on changes in reflection coefficient measurement, we developed 4 methods of measuring photo response. 3 methods use FPGA, the FPGA settings of which are listed in Appendix A, while the other uses ASC 500 box. This section will introduce and compare the four methods.

3.3.1 Static Photo Response Measurement

The most straightforward way of measuring photo response is to compare the reflection coefficients with and without laser irradiating on the inductor. The reason for choosing inductor as the target for the laser is because it has the largest current density and then yields maximum photo response. The

laser is turned on and off through AOM. If it is done by turning on and off the laser diode, it will take a long time for the laser to be stabilized.

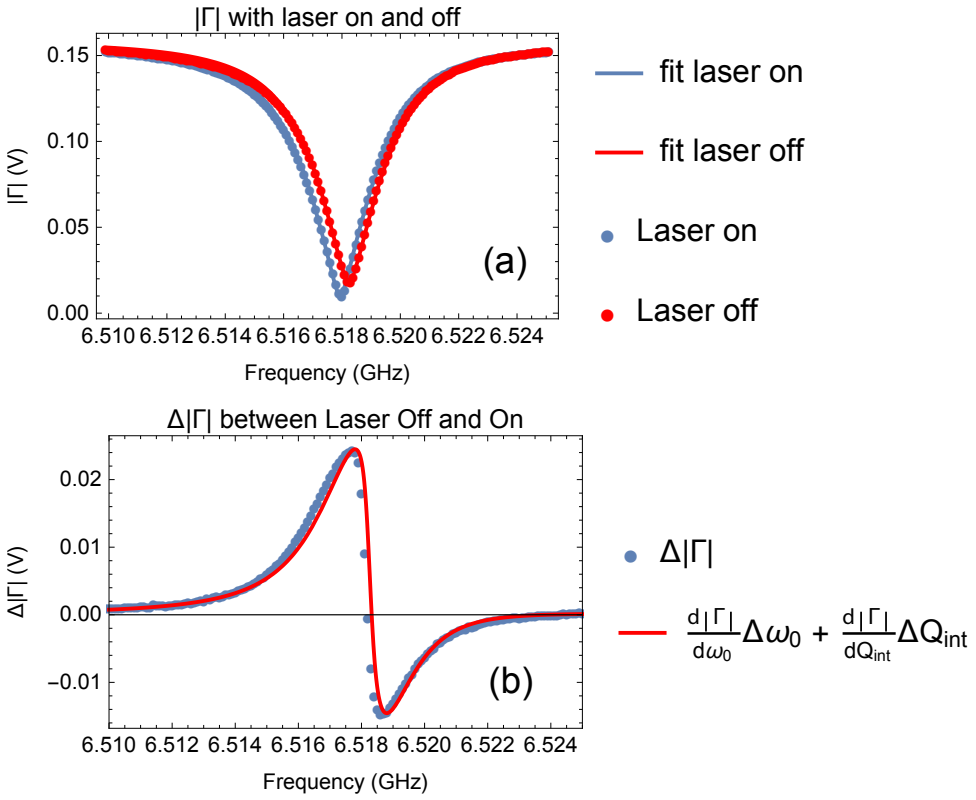

Figure 3.7: (a) Frequency sweep of $|\Gamma|$ with laser on and off. (b) Difference in $|\Gamma|$ between laser on and off.

Figure 3.7 (a) shows the frequency sweeps of $|\Gamma|$ with laser on and off. The difference between the two cases is very small. To make the difference more apparent, one can subtract the two data sets. The result is shown in Figure 3.7 (b).

This method enables extraction of changes in resonance frequency and internal Q factor. By fitting the $|\Gamma|$ curves using the model introduced in Section 2.4:

$$|\Gamma| = \left| \frac{\kappa}{-i(\omega - \omega_0) + \frac{\kappa+\gamma}{2}} \right| = \left| \frac{\omega_0/Q_{ext}}{-i(\omega - \omega_0) + \frac{1}{2}\omega_0(1/Q_{ext} + 1/Q_{int})} \right| . \quad (3.2)$$

One can extract the values of ω_0 and Q_{int} in laser on and off case separately, and the laser-induced changes are the differences between the results. Al-

ternatively, the same information can be extracted by fitting the difference curve shown in Figure 3.7 (b) using model

$$|\Gamma_{off}| - |\Gamma_{on}| = \left| \frac{\omega_0^{off}/Q_{ext}^{off}}{-i(\omega - \omega_0^{off}) + \frac{1}{2}\omega_0^{off}(1/Q_{ext}^{off} + 1/Q_{int}^{off})} \right| - \left| \frac{\omega_0^{on}/Q_{ext}^{on}}{-i(\omega - \omega_0^{on}) + \frac{1}{2}\omega_0^{on}(1/Q_{ext}^{on} + 1/Q_{int}^{on})} \right|, \tag{3.3}$$

where the subscripts and superscripts "on" and "off" stand for the cases of laser on and off respectively. In principle, Q_{ext}'s in the two cases are the same. When the laser-induced changes of resonance frequency and internal Q factor are small, the fitting model can also be written as

$$PR_s = \frac{\partial|\Gamma(\omega)|}{\partial\omega_0}\Delta\omega_0 + \frac{\partial|\Gamma(\omega)|}{\partial Q_{int}}\Delta Q_{int}\,, \tag{3.4}$$

where PR_s stands for "static photo response".

There are two main drawbacks of this method. The first one is relatively longer measurement time, because two frequency sweeps are required for each photo response measurement. The second drawback is related to laser heating. If laser heating is not negligible, the photo response measured by this method will be composed of the effect of heating and the photo response due to direct breaking of Cooper pairs optically. However, only the later component is interesting in most cases.

3.3.2 Lock-in Amplification Measurement Using ASC 500

Lock-in amplification measurement using ASC 500 is a method developed by previous group members working on LSM project, aimed at acquiring spatial dependence of photo response. This is achieved by lock-in detection of the photo response in microwave signal as a function of position. The result is a surface scan of photo response signal in addition to optical reflection signal.

The key of this photo response measurement method is lock-in amplification. A lock-in amplifier can extract and amplify a signal at the modulation frequency from a noisy background. Consider a lock-in amplifier with sine reference at angular frequency ω_{ref}, and an input waveform $U_{in}(t)$, a DC output signal $U_{out}(t)$, then the output signal can be written as [27]

$$U_{out}(t) = \frac{1}{T}\int_{t-T}^{t} sin(\omega_{ref}s + \varphi)U_{in}(s)ds\,, \tag{3.5}$$

where T is averaging time, φ is the phase of reference signal. If the averaging time $T \ll \frac{2\pi}{\omega_{ref}}$, the period of reference signal, any component of angular frequency other than ω_{ref} in $U_{in}(T)$ will be averaged out, leaving the output signal

$$U_{out} = A_{ref}cos\theta\,, \tag{3.6}$$

where A_{ref} is the amplitude of the component of $U_{in}(t)$ at frequency $\omega_{ref}/2\pi$, and θ is the phase difference between input signal and reference signal. The amplitude A_{ref} is the photo response measured by lock-in amplifier.

To measure photo response with ASC 500, the frequencies of two microwave generator should be the same, making the IQ quadratures of the IQ mixer DC in the absent of laser intensity modulation. When the laser intensity is modulated by AOM, IQ quadratures will carry a frequency the same as the frequency of laser modulation due to photo response. After band-filtering centered at modulation frequency and pre-amplification, one of the quadratures goes into a built-in lock-in amplifier in ASC 500 with a reference signal at the same frequency as laser modulation, where the quadrature will be converted to DC signal.

Measuring photo response using lock-in amplifier depends on the projection of complex reflection coefficient on a user-chosen quadrature axis. In the limit of small changes induced by laser, the model of complex photo response (before projection) in this case is given by

$$PR_c = \frac{\partial\Gamma(\omega)}{\partial\omega_0}\Delta\omega_0 + \frac{\partial\Gamma(\omega)}{\partial Q_{int}}\Delta Q_{int}\,, \tag{3.7}$$

which appears on complex plane in a heart shape as shown in Figure 3.8 (a). The projection on real and imaginary axes are shown in Figure 3.8 (b) and (c) respectively, which are I and Q quadratures of the complex PR, the absolute values of which are the photo response given by ASC 500 depending on the chosen quadrature. The theoretical ASC 500 photo response can be found in Figure 3.9.

However, the experimental data shows deviation from the theoretical prediction. As lock-in amplifier only returns absolute value, the IQ data of photo

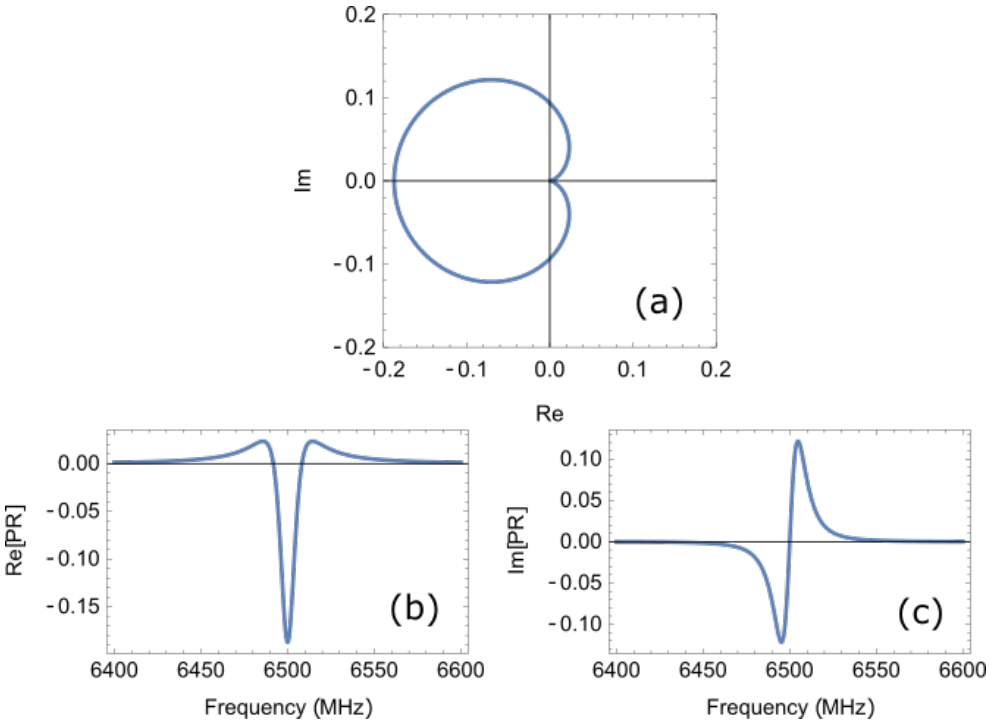

Figure 3.8: Frequency dependent complex PR projected on (a) complex plane, (b) on real axis, and (c) on imaginary axis.

response is folded in the first quadrant of IQ plane. After assigning an arbitrary sign, the IQ data can be expanded to the whole IQ plane, which is shown in Figure 3.10 (b). The absolute projection of PR on I and Q axes is shown in Figure 3.10 (a).

The experimental data differs from theoretical model in various ways. The measured complex PR winds around origin of IQ plane twice, which is not observed in theoretical model. The orientations of the heart shape are also different. Finally, the experimental result is clearly asymmetric, while the theoretical data is symmetric. The asymmetric peaks in ASC 500 photo response are given by the orientation and asymmetry in complex PR data, and the non-monotonic tails away from resonance are caused by the additional winding around the origin in complex PR. So the theoretical model described above is not complete.

The reason for the extra winding around the origin is the non-zero optical length of microwave components. The optical length and phase shift can be modeled by an extra phaser of the complex reflection coefficient

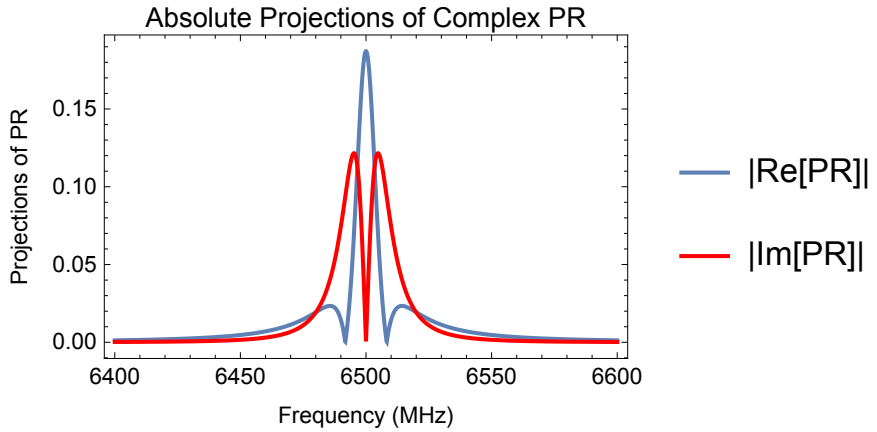

Figure 3.9: Theoretical ASC 500 photo response, i.e. the absolute projection of complex PR on real and imaginary axes.

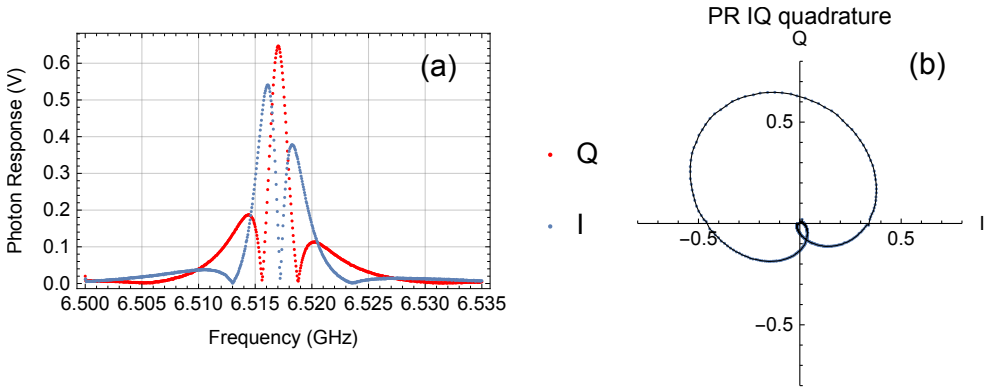

Figure 3.10: (a) ASC 500 photo response from I and Q ports of the IQ mixer; (b) expanded PR on the whole IQ plane.

$$\Gamma = e^{i(\varphi+\tau_{opt}\omega)} \frac{\omega_0/Q_{ext}}{-i(\omega-\omega_0)+\frac{1}{2}\omega_0(1/Q_{ext}+1/Q_{int})} \tag{3.8}$$

where φ is phase shift and τ_{opt} is optical delay due to finite optical length. When we are measuring the amplitude of Γ, the phaser $e^{i(\varphi+\tau_{opt}\omega)}$ cancels out by taking absolute value. However, ASC 500 measures the projection of complex PR on I or Q axis, where the phaser plays a significant role. The phaser can be canceled by multiplying Equation 3.8 with $e^{-i(\varphi+\tau_{opt}\omega)}$. Figure 3.11 (b) shows the phaser-corrected complex PR, where there is no additional winding around origin. In the absolute projection of complex PR, as shown in 3.11 (a), there are no non-monotonic tails away from resonance frequency.

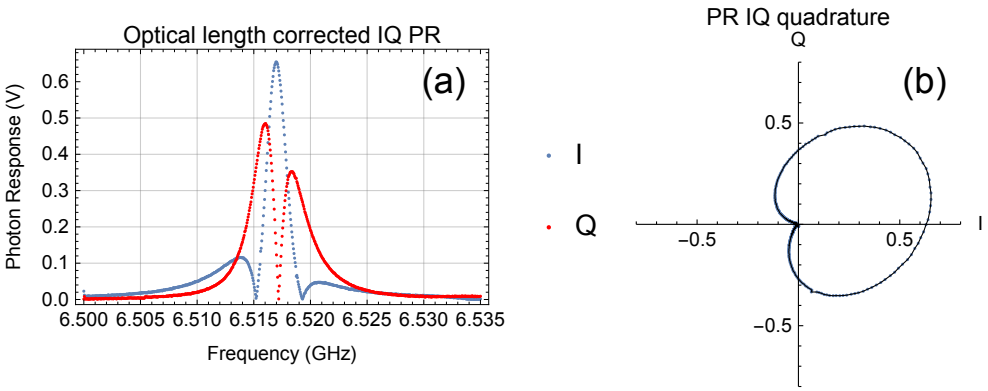

Figure 3.11: (a) Absolute projection of experimental complex photo response after optical length and phase shift correction. (b) Experimental complex photo response after optical length and phase shift correction.

However, as shown by Figure 3.11 (a), the asymmetry in the shape of complex PR still leads to significant asymmetry in absolute projection, which prevents us from extracting information like shift of resonance frequency and shift of internal Q factor by fitting the curves. The origin of the asymmetry is not clear yet, but a possible explanation lies in the time of performing I and Q measurement. We observe more asymmetry when the time between I and Q measurement is longer. If we can develop a method measuring I and Q quadratures simultaneously, we might be able to solve the asymmetry problem.

The uncertainty in phase shift and optical length are also problematic. Calculating PR amplitude from I and Q quadratures helps overcoming this problem. PR amplitude is given by

$$|PR| = \sqrt{|PR_I|^2 + |PR_Q|^2}\,, \tag{3.9}$$

where $|PR_I|$ and $|PR_Q|$ are absolute projection of complex PR on I axis and Q axis respectively, which are the frequency sweep results given by ASC 500 box. The theoretical PR amplitude given by this method is a squared Lorentzian peak centered at resonance frequency. However, the asymmetry in complex PR makes the peak slightly asymmetric as well, which is shown in Figure 3.12.

However, even if the peak is symmetric, the one peak photo response cannot distinguish between the shift of ω_0 and Q_{int}. The amplitude of resonance frequency response is given by

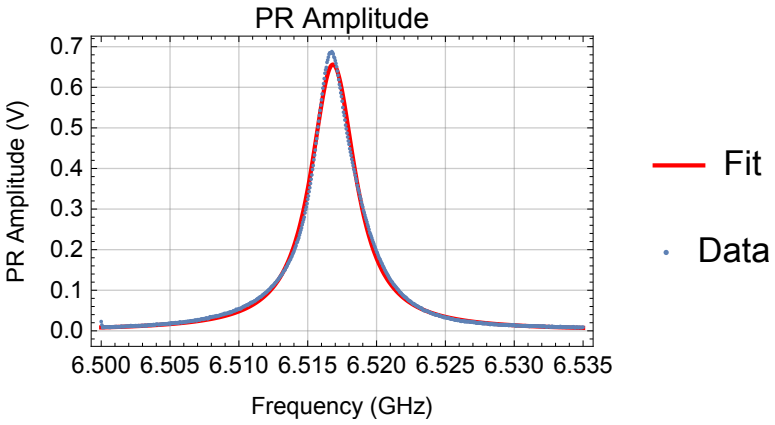

Figure 3.12: PR amplitude calculated by summing up square of I and Q responses, and the best fit given by mathematica.

$$|PR_{\omega_0}| = \left|\frac{\partial\Gamma}{\partial\omega_0}\Delta\omega_0\right| = \left|\frac{(-1-\frac{i}{2Q_{int}})\frac{\omega_0}{Q_{ext}}}{((\omega-\omega_0)-i\frac{1}{2}\omega_0(\frac{1}{Q_{int}}+\frac{1}{Q_{ext}}))^2}\Delta\omega_0\right|, \tag{3.10}$$

and internal Q factor response is given by

$$|PR_{Q_{int}}| = \left|\frac{\partial\Gamma}{\partial Q_{int}}\Delta Q_{int}\right| = \frac{1}{2}\left|\frac{\omega_0^2/Q_{ext}}{Q_{int}^2((\omega-\omega_0)-i\frac{1}{2}\omega_0(\frac{1}{Q_{int}}+\frac{1}{Q_{ext}}))^2}\Delta Q_{int}\right|. \tag{3.11}$$

Both of the $|PR|$ are Lorentzian peaks centered at resonance frequency, which are indistinguishable in the one-peak experimental result. The usage of this calculated PR is to determine total photo response amplitude without being affected by the phaser.

3.3.3 Voltage Photo Response Measurement Using FPGA

Subtracting $|\Gamma_{on}|$ and $|\Gamma_{off}|$, and calculating $|PR| = \sqrt{|PR_I|^2+|PR_Q|^2}$ requires two measurements to get meaningful photo response result. By using DiffMode in FPGA, it is possible to perform the task in one measurement. This subsection introduces the method of measuring voltage photo response using FPGA. The name comes from the fact that this photo response signal is proportional to ADC voltage at FPGA.

As introduced in Section 3.2, when DiffMode and Averaging Mode is on, FPGA will subtract the results of two consecutive measurements, and take

the average of $N/2$ differences, where N is the number of total measurement. When the laser intensity is modulated, triggering FPGA at maximum and minimum laser intensity alternatively gives the photo response. The pulse pattern of FPGA trigger and laser modulation is shown in Figure 3.13. The trigger frequency of FPGA is set to be twice the laser modulation, so that the rising edge of triggering pulse can be located at maximum and minimum of laser intensity. The measurement time of $8.191ns$ for FPGA is negligible compared to the period of laser modulation 200 μs, so that the whole FPGA measurement can be considered as conducted at the same laser intensity.

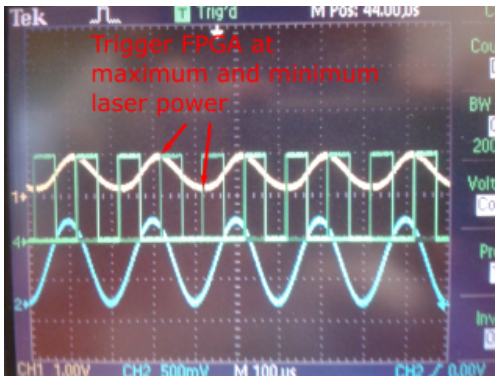

Figure 3.13: The pulse pattern of FPGA trigger in oscilloscope. The green channel is FPGA pulse, the yellow channel is laser intensity, and the blue channel is output signal from ASC 500 box, controlling AOM. FPGA is triggered at rising edge, so the measurement starts at maximum and minimum laser intensity alternatively.

The relative phase between FPGA trigger and laser modulation will drift if AWG triggering FPGA and ASC 500 box (or other device used to generating signal to AOM) is not synchronized. The drifting prevents the measurements conducting at maximum laser intensity difference. ASC 500 box cannot receive external time reference, so the ways to synchronize the two devices are triggering AWG with output signal from ASC 500 using a digital delay generator, or modulating laser with another AWG, which receives the same external time reference as the FPGA triggering AWG.

The theoretical model of voltage PR measurement is

$$PR_v = \sqrt{|Re(\Delta\Gamma)|^2 + |Im(\Delta\Gamma)|^2} = \sqrt{|Re(PR)|^2 + |Im(PR)|^2}, \qquad (3.12)$$

which is exactly the same as PR amplitude given by lock-in amplification method as in Equation 3.9. For the same reason, it is impossible to extract information like shift of ω_0 or Q_{int} from the data acquired by this FPGA setting. However, again, the data is a faithful measure of PR amplitude. Figure

3.14 shows an example of PR amplitude given by FPGA measurement and its fitting curve.

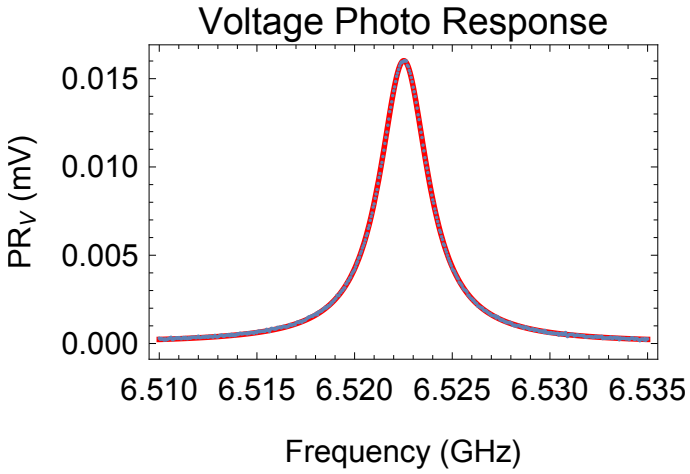

Figure 3.14: An example of PR amplitude acquired by FPGA, where the red curve is the fitting, and blue dots are the data points. The data is acquired in the condition of 10.66 μW laser on sample, -94 dBm microwave power and 4 K temperature.

To confirm the claim that voltage PR and lock-in amplification PR amplitudes are in principle the same, we measured photo responses using the two methods at different input RF power and compared the peak value at IQ mixer (where the amplification chain become different). The results are listed in the following table:

RF power (dBm)	FPGA PR amplitude (mV)	Lock-in PR amplitude (mV)
-50	1.15	1.15
-54	0.7	0.73
-58	0.44	0.46

So the voltage PR and PR amplitude are truly the same, as predicted by theoretical model.

3.3.4 Power Photo Response Measurement Using FPGA

DiffMode in FPGA not only provides the possibility to measure voltage photo response in a single measurement without phase and electric delay effects, but also enables extracting laser-induced changes of resonance frequency and internal Q factor. Similar to the method introduced in Subsection 3.3.3, this method also requires the AWG triggering FPGA being synchronized to laser intensity modulation. The difference in FPGA settings

between power PR measurement and voltage PR measurement is that the former case measures microwave power at FPGA, while the latter case measures ADC voltage. The theoretical model of power PR measurement is

$$\begin{aligned} PR_p &= \Delta|\Gamma|^2 \\ &= |\Gamma(\omega_0 + \Delta\omega_0, Q_{ext}, Q_{int} + \Delta Q_{int})|^2 - |\Gamma(\omega_0, Q_{ext}, Q_{int})|^2 , \end{aligned} \tag{3.13}$$

where PR_p is the power PR, and $\Delta\omega_0$ and ΔQ_{int} are laser-induced changes in resonance frequency and internal Q factor respectively. In practice, Cleansweep takes the absolute value of PR_p, and exhibits a two-peak profile as shown in Figure 3.15.

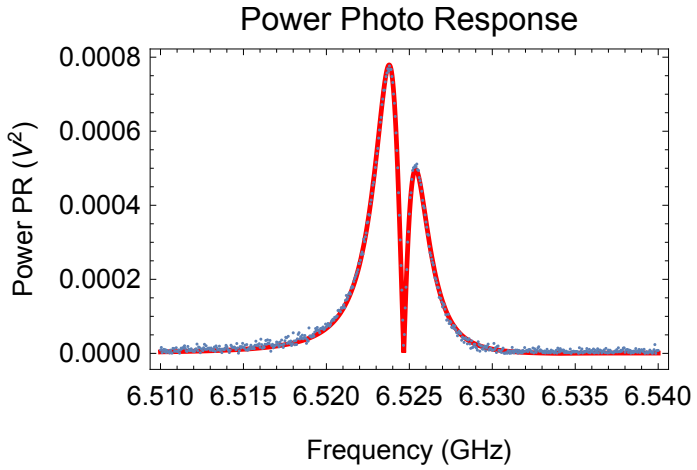

Figure 3.15: A frequency dependent PR_p curve measured at 3.2 K.

Unlike the one-peak curve in PR amplitude case, the difference between two peaks reveals the proportion of ω_0 and Q_{int} contributions in the total photo response. To understand this, plotting $\frac{\partial|\Gamma|^2}{\partial\omega_0}$ and $\frac{\partial|\Gamma|^2}{\partial Q_{int}}$ against frequency is beneficial, because when the laser induced changes are small, PR_p is given by

$$PR_p = \frac{\partial|\Gamma|^2}{\partial\omega_0}\Delta\omega_0 + \frac{\partial|\Gamma|^2}{\partial Q_{int}}\Delta Q_{int} , \tag{3.14}$$

so that the partial derivatives determines the shape of corresponding PR contribution. The partial derivatives with small internal loss in lumped element resonators are plotted in Figure 3.16, which is the case at low temperature. In general, $\frac{\partial|\Gamma|^2}{\partial\omega_0}$ is anti-symmetric and $\frac{\partial|\Gamma|^2}{\partial Q_{int}}$ is symmetric with $\omega = \omega_0$ being

the line of symmetry. Zhuravel and his colleagues developed a method to extract resistive and inductive photo response in terms of S parameter based on this fact [9]. In their method, resistive photo response at a frequency f away from resonance is given by

$$PR_R(f) = \frac{|PR(f+) + PR(f-)|}{2}, \tag{3.15}$$

where $PR(f+)$ is the total photo response at frequency f above resonance frequency and $PR(f-)$ below. Similarly, inductive photo response is given by

$$PR_I(f) = \frac{|PR(f+) - PR(f-)|}{2}. \tag{3.16}$$

Though the basic ideas are the same, we analyzed our data slightly differently. In Chapter 2, we concluded that the sign of laser-induced changes in ω_0 and Q_{int} are both negative, so the two contributions on the low frequency side sum up, and on the high frequency side compensate each other, resulting in asymmetric peaks in the absolute value. The difference in two peaks reveals the proportion of the two PR contributions as we claimed.

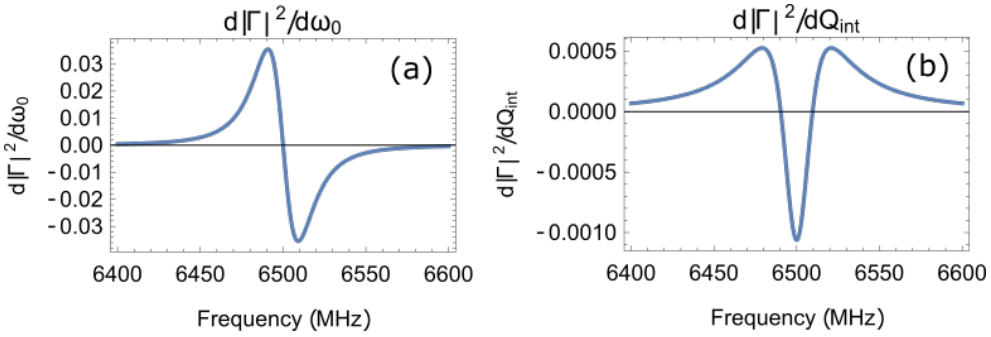

Figure 3.16: Simulation of partial derivatives of $|\Gamma|^2$ with small internal loss in lumped element resonators. (a) $\frac{\partial|\Gamma|^2}{\partial\omega_0}$; (b) $\frac{\partial|\Gamma|^2}{\partial Q_{int}}$.

Although the PR_p method enables laser-induced change extraction, its signal-to-noise ratio is much lower than other methods, which will be discussed in Chapter 5.

3.4 Signal-to-Noise Ratio of Reflection Coefficient Measurement

Signal-to-noise ratio is crucial for any precise measurement, so is it for laser scanning microscopy, especially, when we consider that the ultimate goal is to operate LSM at 20 mK and quantum limited RF power. Before doing any investigation, it is necessary to evaluate the possibility of detecting any signal with target condition. Estimating signal-to-noise ratio of reflection coefficient is the first step, which is directly related to the main noise sources: thermal noise and quantum noise. Signal-to-noise ratio of PR, which will be discussed in Chapter 5, can be estimated on the basis of noise estimation presented here. A detailed introduction to thermal noise calculation can be found in Christopher Eichler's PhD thesis [28].

Consider the sample with HEMT as cold amplifier as shown in Figure 3.3. The initial noise comes from thermal noise at room temperature and noise in signal generation. Because the signal generation noise of Rohde&Schwarz SMB 100A RF generator is very low (down to -128 dBc [29]), we can estimate the initial noise by the thermal noise given by black body radiation at room temperature. (We will see later that the initial noise has little influence on the final result, so the estimation is still valid even if the noise from RF generator is not small compared to thermal noise.) If we write noise in terms of number of noise photons, then the initial number of noise photon $n_0 = 1/(e^{\hbar\omega/k_B T_{room}} - 1) \approx 150$ per Hz per second for $T_{room} = 300$ K. Then the input signal propagates into the fridge, and is attenuated by a thermalized 20 dB attenuator (the power drops to $10^{-20/10} = 0.01$ time of the original value), then the noise becomes $n = 0.01 n_0 + 1/(e^{\hbar\omega/k_B T_{attenuator}} - 1)$. Similarly, the thermalized directional coupler attenuates the signal and noise by 20 dB subsequently, then the noise photon number

$$\begin{aligned} n_s =& 0.01(0.01 n_0 + 1/(e^{\hbar\omega/k_B T_{attenuator}} - 1)) + 1/(e^{\hbar\omega/k_B T_{coupler}} - 1) \\ \approx& 1.58 \textit{ per Hz per second}. \end{aligned} \tag{3.17}$$

The noise photon number at this stage is the noise photon number reflected from sample at an off-resonance frequency, for convenience, here, we name it n_s. By far, the noise from room temperature setup has dropped to 10^{-4} of the initial value, i.e. around 0.01 noise photons per Hz per second, which is ignorable compared to the total noise photon number. The reflected signal with noise n_s is amplified along an amplification chain from sample to FPGA. Because the amplification chain amplifies noise and signal at the same time, the amplifiers have little effect on signal-to-noise ratio if the signal after amplification is much larger than the noise added by the amplifier.

Similar to the effect of attenuation on noise along the input line, the noise added by an amplifier along the amplification chain is more significant if the amplifier is closer to the sample, because the added noise is amplified more times by amplifiers at later stage. For this reason, it is enough to estimate the noise added by HEMT thermalized at 3 K ($T_{HEMT} = 3$ K) along the amplification chain before IQ mixer. According to the data sheet of the HEMT, its noise temperature $T_{NHEMT} = 4$ K. To keep our final noise photon number comparable to the photon number reflected by the sample, the total number of noise photons is normalized by keeping n_s the same, any amplification (attenuation) to signal is treated as attenuation (amplification) to the noise added by microwave elements at later stage. Then the number of noise photon after HEMT is

$$\begin{aligned} n =& \frac{n_{HEMT}+1}{A} + n_s + 1 \\ =& \frac{1}{A}\left(\frac{1}{e^{\hbar\omega/k_B(T_{HEMT})}-1} + \frac{1}{e^{\hbar\omega/k_B(T_{NHEMT})}-1} + 1\right) + n_s + 1\,, \end{aligned} \tag{3.18}$$

where A is the attenuation from sample to HEMT, n_{HEMT} is the thermal noise from HEMT, the 1 added to n_{HEMT} and n_s accounts for amplified vacuum fluctuation [30]. If we substitute the variables with typical value $A = 0.5$, $T_{HEMT} = 3$ K, and $T_{NHEMT} = 4$ K we will have $n \approx 55$ per Hz per second. Neglecting the effect of other amplifiers on signal-to-noise ratio, Equation 3.18 gives the noise at IQ mixer as well. If one of the I or Q port of the mixer is not in use and terminated, the noise will effectively double due to backfolding of noise at frequency higher than LO frequency [31]. In our case, both of I and Q ports are in use, then Equation 3.18 gives the final number of noise photons. So the final normalized number of noise photon per second detected by FPGA is

$$\begin{aligned} N_{noise} &= B\left(\frac{n_{HEMT}+1}{A} + n_s + 1\right) \\ &= B\left(\frac{1}{A}\left(\frac{1}{e^{\hbar\omega/k_B T_{HEMT}}-1} + \frac{1}{e^{\hbar\omega/k_B T_{NHEMT}}-1} + 1\right) + n_s + 1\right)\,, \end{aligned} \tag{3.19}$$

where B is the ADC bandwidth of the FPGA. Taking $B = 1$ GHz, the total normalized noise power detected by FPGA is about 5.5×10^{10} photons per second.

Consider an input RF power of -46 dBm, a typical value in this study, then

the signal power at sample is -94 dBm, where one 20 dB attenuation comes from attenuator, another 20 dB attenuation comes from directional coupler and 8 dB attenuation comes from losses in cables. Then the number of signal photons per second is given by $N_{signal} = \frac{PowerAtSample}{hf} = \frac{2\pi 10^{(-94-30)/10}}{6.63*10^{-34}*6.5*10^{9}} = 9.2 \times 10^{10}$ photons per second. The signal-to-noise ratio η_{sn} in FPGA is then given by

$$\eta_{sn} = \sqrt{\frac{N_{signal}}{N_{noise}}}, \tag{3.20}$$

where the square root comes from the fact that voltage detected by FPGA is proportional to the square root of power, and power is proportional to the photon number per second. With the estimated results, the final estimated signal-to-noise ratio of Γ at -46 dBm RF input is calculated to be about 1.3. The experimental result with the same condition gives a signal-to-noise ratio around 1.3, which agrees with our estimation. To check the validity of our estimation, the comparison is conducted at different RF powers. The results are shown in Figure 3.17, which show the agreement of estimation and experiment is not an coincidence.

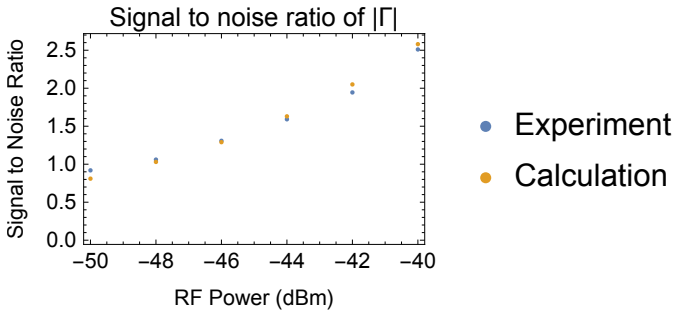

Figure 3.17: Experimental and estimating signal-to-noise at different RF powers.

Chapter 4

Experimental Results of Photo Response and Discussion

In Chapter 3, we have seen how to measure photo response and extract laser-induced resonance frequency and internal Q factor change. In this chapter, the effect of different experimental condition on photo response amplitude and laser-induced changes will be discussed. The varying parameters are laser, microwave power, temperature and focus of laser beam. These studies help us understand the origin of photo response signal, and shine light on optimal operating conditions.

The position of laser beam on sample changes slowly with time even without signal input to the piezos. The uncertainty of laser beam position is around 1 μm, while the inductor stripe width is 2 μm. The drifting of laser beam position has the potential to significantly influence experimental result. To avoid the effect of position drifting, we performed a part of our measurement with defocused laser, because the photo response induced by defocused laser is spatial-insensitive (see Section 4.5 for detail).

4.1 Extraction of Laser-Induced Change of Resonator Properties

It is beneficial to start with the simplest and the most well-understood measurement, the static photo response measurement introduced in Subsection 3.3.1. Although static photo response measurement records both effects of photo response and laser heating, it can provide estimated laser-induced changes of resonance frequency and internal Q factor, which can be used as references.

Figure 4.1 (a) shows the data and fitting of $|\Gamma|$ measurement with laser on and off at 10.66 μW laser and -94 dBm microwave power at sample, and 4 K

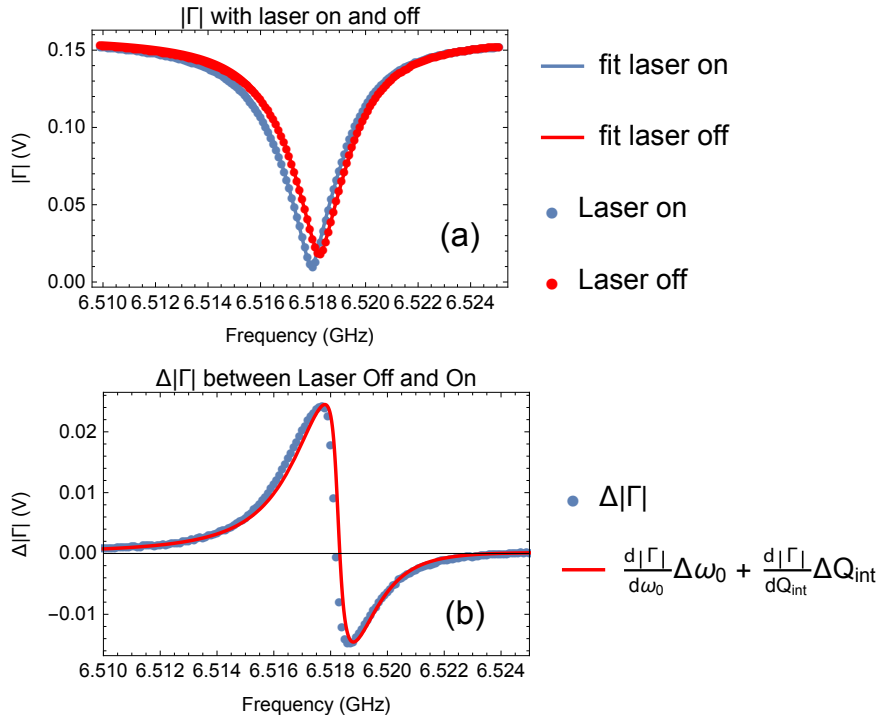

Figure 4.1: (a) $|\Gamma|$ measurements with laser on and off. The experimental condition is 10.66 μW laser and -94 dBm microwave power at sample, and 4 K temperature. (b) The plot of $\Gamma_{off} - \Gamma_{on}$ and the plot of $\frac{\partial|\Gamma|}{\partial\omega_0}\Delta\omega_0 + \frac{\partial|\Gamma|}{\partial Q_{int}}\Delta Q_{int}$ with parameters given by fittings in (a).

temperature. The results of fitting parameters are listed as follows:

Laser Status	Q_{ext}	Q_{int}	f_0 (GHz)
Off	2920 ± 20	3724 ± 19	$6.51824 \pm 5 \times 10^{-6}$
On	2927 ± 22	3332 ± 20	$6.51794 \pm 4 \times 10^{-6}$

where the uncertainties are given by built-in fitting routine. The changes $\Delta f_0 = -300 \pm 71$ kHz and $\Delta Q_{int} = -392 \pm 27$. Figure 4.1 (b) shows the plot of $\Gamma_{off} - \Gamma_{on}$ and the plot of $\frac{\partial|\Gamma|}{\partial\omega_0}\Delta\omega_0 + \frac{\partial|\Gamma|}{\partial Q_{int}}\Delta Q_{int}$ with parameters given by fittings of $|\Gamma|$. The deviation of $\Gamma_{off} - \Gamma_{on}$ from $\frac{\partial|\Gamma|}{\partial\omega_0}\Delta\omega_0 + \frac{\partial|\Gamma|}{\partial Q_{int}}\Delta Q_{int}$ comes from the fact that $\Delta\omega_0$ and ΔQ_{int} are not infinitely small.

In our experiment, most laser-induced changes of resonator properties are extracted by measuring PR_p and fit the result with model presented in Equation 3.13. Figure 4.2 shows the PR_p data measured with the same condition as Figure 4.1. The deviation of fitting curve from experimental data will be discussed in Section 4.4. The values of fitting parameters are listed as follows:

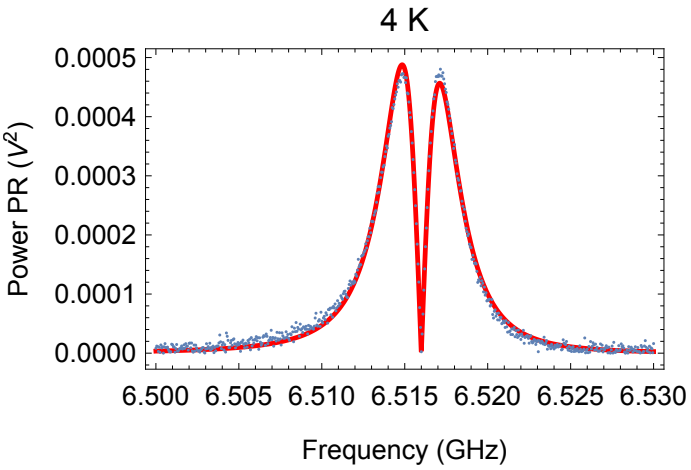

Figure 4.2: PR_p data and fitting. The experimental condition is 10.66 μW laser and -94 dBm microwave power at sample, and 4 K temperature.

Q_{int}	f_0 (GHz)	ΔQ_{int}	Δf_0 (kHz)
3755 ± 27	$6.51612 \pm 3 \times 10^{-6}$	-21 ± 1	-124 ± 0.4

Comparison between the results of two methods shows that the laser-induced changes in resonance frequencies are of the same order, while the change in internal Q factor given by $|\Gamma|$ measurement is one order of magnitude larger than that given by PR_p measurement. The difference could come from different experimental conditions and laser heating in $|\Gamma|$ measurement. The time separation between the two measurements is more than one month. During the time, experimental conditions like laser power on sample and temperature may change. The different resonance frequencies in the two measurements are a signature of different temperature. Moreover, as explained in Chapter 2, heating has similar effect on resonator properties to photo response, which enhances the laser-induced changes in static photo response measurement.

We can also compare theoretically estimated values of resonator properties and photo responses with experimental data. Due to better fitting, we choose PR_p data at 3 K instead of 4 K. Figure 4.3 shows the data and fitting of PR_p under condition 10.66 μW focused laser and -94 dBm microwave power at sample and 3 K temperature.

The key of photo response theory is change in superconducting electron density n_s. Here we estimate n_s by extracting kinetic inductance and London penetration depth. As shown in Section 2.3, in thin film limit ($t \ll \lambda_L(T)$), ω_0 follows the following relation with temperature

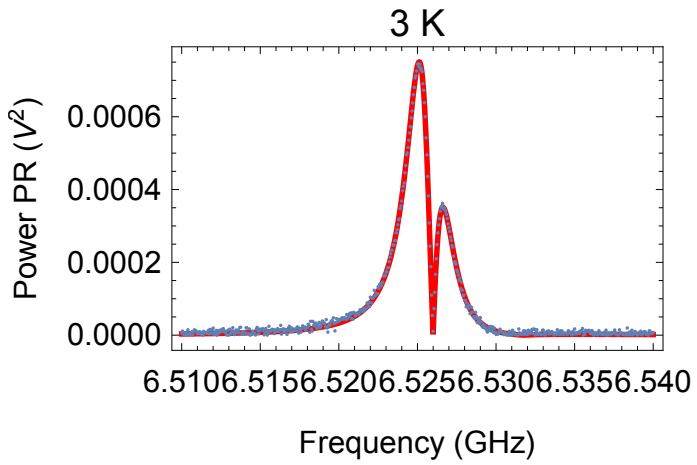

Figure 4.3: PR_p data and fitting. The experimental condition is 10.66 μW laser and -94 dBm microwave power at sample, and 3 K temperature.

$$\omega_0 = \frac{1}{\sqrt{C(L_m + L_{kin})}} = \frac{1}{\sqrt{C(L_m + L_{kin0}/(1-(T/T_c)^4))}}, \tag{4.1}$$

where L_{kin0} is the kinetic inductance at zero temperature; while in thick film limit ($t \gg \lambda_L(T)$),

$$\omega_0 = \frac{1}{\sqrt{C(L_m + L_{kin})}} = \frac{1}{\sqrt{C(L_m + L_{kin0}/(1-(T/T_c)^4)^{1/2})}}. \tag{4.2}$$

Figure 4.4 shows the temperature dependence of ω_0 with fitting using the above equations and condition $T_c = 9.22$ K, $C = 3.5 \times 10^{-13}$ F and $L_m + L_{kin0} = 1.7 \times 10^{-9}$ H, from which the approximate kinetic inductance of the resonator L_{kin0} can be extracted. By applying Equation 2.18 and film thickness $t = 150$ nm, thick film limit fitting gives $\lambda_L(T) = 193$ nm, and thin film limit $\lambda_L(T) = 109$ nm. Neither of the limits satisfies their assumption. The actual penetration depth could be a value in between; we fix it as 150 nm for the following estimation.

According to Equation 2.6, the charge carrier density $n = 1.25 \times 10^{27}$ m^{-3}, and superconducting electron density at 3 K $n_s = 1.24 \times 10^{27}$ m^{-3}. Laser-generated quasiparticle number N_{qp} can be calculated using the following equation

$$\frac{dN_{qp}}{dt} = -\frac{N_{qp}}{\tau_{qp}} + \eta \frac{P}{E_g}, \tag{4.3}$$

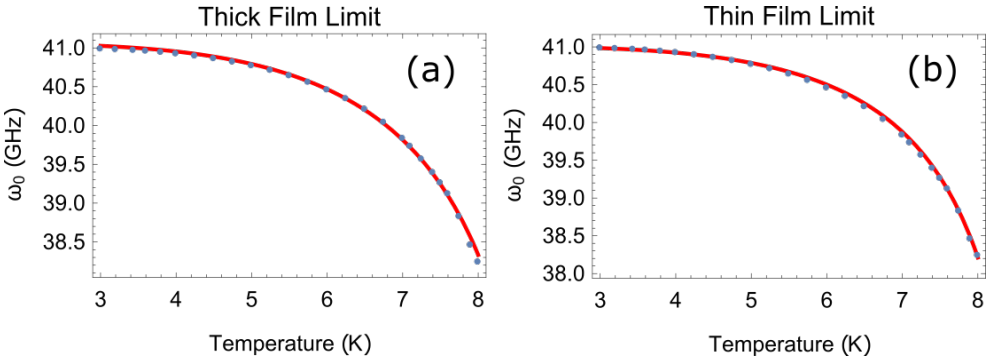

Figure 4.4: Temperature dependence of ω_0 with fitting in (a) thick film limit, and (b) thin film limit. Critical temperature $T_c = 9.22$ K.

where τ_{qp} is the life time of laser-induced quasiparticle, η is the efficiency of photons absorption, P is laser power, and E_g is superconducting gap energy. At equilibrium, we have

$$N_{qp} = \frac{\eta P \tau_{qp}}{E_g}, \tag{4.4}$$

by substituting $P = 10.7$ μW, $\eta = 0.1$ [32], $\tau_{qp} = 10$ ns [33], and $E_g = 2.9(1 - T/T_c)^{1.94}(1 + 2.17T/T_c)$ meV [24, 34], where $T = 3$ K and $T_c = 9.22$ K, the maximum number of laser induced quasiparticle is 3×10^7. The laser-influenced area of focused laser spot S_{laser} is approximately 4 μm^2 (due to diffusion of quasiparticles, this value is larger than the laser spot size), then one can estimate the number of superconducting electron to be $N_s = n_s t S_{laser} = 7 \times 10^8$, which is 1 order of magnitude larger than N_{qp}. Thus, the small laser-induced change estimation is valid in this case. We have

$$\Delta\omega_0 = -\frac{1}{2}\frac{1}{\sqrt{C}}\frac{\Delta L_{kin}}{(L_m + L_{kin})^{3/2}}. \tag{4.5}$$

Assume the laser-influenced area is a rectangle with width $W = w = 2$ μm and length $L = 2$ μm (refer to Figure 4.5), then the total kinetic inductance is the sum of the kinetic inductance of the laser-influenced area and that of the uninfluenced part. Thus the laser-induced kinetic inductance change ΔL_{kin} can be calculated from Equation 2.19 in thick film limit:

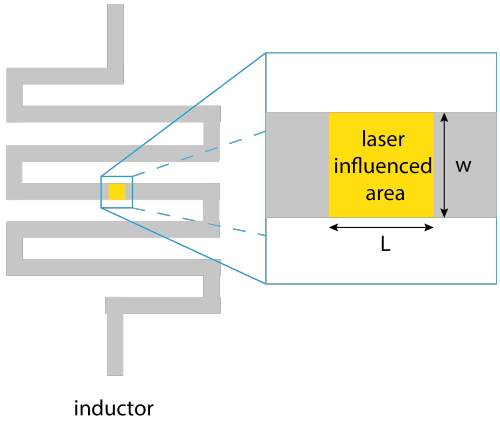

Figure 4.5: Sketch of laser-influenced area for laser focused on meander inductor in a simplified model for photo response estimation, where the laser-influenced area is a square with side length $W = 2\ \mu$m.

$$\begin{aligned}\Delta L_{kin} &= \frac{dL_{kin}}{dn_s}\Delta n_s = -\frac{1}{2}\mu_0\sqrt{\frac{m_e}{e^2\mu_0}}\frac{L}{W}n_s^{-3/2}\Delta n_s = -\frac{1}{2}\mu_0^2\frac{e^2L}{m_eW}\lambda_L^3\Delta n_s \\ &= -\frac{1}{2}\mu_0^2\frac{e^2L}{m_eW}\lambda_L^3\frac{-N_{qp}}{V} = \frac{1}{2}\mu_0^2\frac{e^2L}{m_eW}\lambda_L^3\frac{N_{qp}}{\lambda_L WL} \\ &= \frac{1}{2}\mu_0^2\frac{e^2}{m_eW^2}\lambda_L^2N_{qp}\,.\end{aligned} \tag{4.6}$$

Substituting this expression to Equation 4.5, the laser-induced change in angular resonance frequency is calculated to be $\Delta\omega_0 = -40$ kHz.

By Equation 2.43, energy loss rate γ can be written as

$$\gamma = \frac{R^*}{L_m + L_{kin}} = \frac{\frac{1}{2}\frac{l}{w}\omega^2\mu_0^2\lambda_L^3(T)\frac{n-n_s}{n}\sigma_1}{L_m + \mu_0\lambda_L(T)\frac{l}{w}}\,. \tag{4.7}$$

By substituting $1/\sigma_1 = 0.58 \times 10^{-7}\ \Omega$m [35], the theoretical energy loss rate $\gamma \approx 1$ MHz. Laser-induced change in energy loss rate $\Delta\gamma$ can be estimated similar to $\Delta\omega$. As $L_m \ll L_{kin}$ at 3 K, we can ignore the laser induced change in the denominator of Equation 4.7. Then we have

$$\Delta\gamma = \frac{\Delta R^*}{L_m + L_{kin}}\,, \tag{4.8}$$

where

$$\begin{aligned}\Delta R^* &= \frac{dR^*}{dn_s}\Delta n_s = \frac{d(\frac{1}{2}\omega^2\frac{l}{w}\frac{m_e^{3/2}\mu_0^{1/2}}{e^3}\sigma_1 n_s^{-3/2}\frac{n-n_s}{n})}{dn_s}\Delta n_s \\ &= \frac{1}{2}\omega^2\frac{L}{W}\frac{\mu_0^{1/2}}{ne^3}\sigma_1(\frac{3}{2}n_s^{-5/2}n - \frac{1}{2}n_s^{-3/2})\frac{N_{qp}}{N_s}n_s \\ &= \frac{1}{4}\omega^2\frac{L}{W}\frac{\mu_0^{1/2}}{ne^3}\sigma_1 n_s^{-1/2}(3\frac{n}{n_s} - 1)\frac{N_{qp}}{N_s}\,.\end{aligned} \tag{4.9}$$

Substituting this expression to Equation 4.8, the estimated laser-induced change in loss rate $\Delta\gamma \approx 2$ kHz. The experiment and theoretical results are summarized in the following table:

	γ (MHz)	$\Delta\omega_0$ (MHz)	$\Delta\gamma$ kHz
Experiment	2.6	1.2	152
Theory	1	0.04	2

The theoretically estimated values are smaller than experimental ones. Among which, estimated γ is of the same order of magnitude as experiment, $\Delta\omega_0$ is one order of magnitude smaller, and $\Delta\gamma$ is two orders of magnitude smaller. As estimated $\Delta\gamma$ is calculated from estimated γ, which is smaller than experimental value, a factor of 3 will be added to the deviation of estimated $\Delta\gamma$ from the experimental one. After this correction, we can conclude that the theories of both $\Delta\gamma$ and $\Delta\omega_0$ give values one order of magnitude smaller than the experimental ones with the parameters used above. The deviation between theory and experiment may come from three sources. The first one is using the inaccurate assumption of thick film limit in the calculation of ΔL_{kin}. The second aspect is related to inaccurate parameters. Due to different geometry of Niobium film and different purity, the parameters like recombination rate of quasiparticles, the conductivity, and the absorption efficiency of photon can be very different from the chosen values. The third reason lies in our simplified model. In our model, density of superconducting electrons is uniform in the laser-influenced area. If the spatial distribution of quasiparticle density is taken into consideration, there will be an effective temperature distribution in the laser-influenced area with the highest temperature at the laser spot. When quasiparticles created by laser diffuse away from laser spot, the effective temperature decreases, which will cause a significant increase of τ_{qp} the recombination time of quasiparticles, due to the exponential relation of τ_{qp} and temperature [33]. This increase of τ_{qp} would increase photo response. Other simplification will also affect the accuracy of the theoretical model, so one order of magnitude difference between theoretical and experimental values is reasonable.

4.2 Microwave Power Dependence of PR

Operating LSM at quantum limited microwave power is one of the long term goals for this thesis. Understanding how resonator and its photo response behaves at different RF power is crucial. The theory of current density dependence of photo response is presented in Section 2.5. The microwave power dependence of photo response can be derived from the current density dependence.

The theory states that photo response magnitude in terms of energy should be proportional to the local current density at the laser probe, however the laser-induced changes in resonance frequency $\Delta\omega_0$ and internal energy loss rate $\Delta\gamma$ are independent of the total current passing through the inductor. Our photo response is proportional to voltage of the reflected signal (V_{out}), which is given by $V_{out} = \sqrt{RP}$, where P is the microwave power indicated on ADC in FPGA, and R is the ADC port resistance ($R = 50\ \Omega$). As R is a constant, any change in V_{out} (voltage PR) is given by change in microwave power reflected from the sample. Equation $\kappa E = P_{RF}$ gives the relation between energy stored in resonator and input/output RF power in equilibrium case, with which we can transfer microwave power problem into energy problem. Energy stored in lumped element resonator can be written as $E = (L_m + L_{kin})\bar{I}^2$, where $\bar{I}$ is the root mean current flowing through inductor. Then unperturbed reflected RF power from sample is given by $P = \kappa(L_m + L_{kin})\bar{I}^2$, which is proportional to $\bar{I}^2$ in the resonator. From Chapter 2, there are two sources of energy change generated by laser, resistive and inductive. The inductive one is given by $\Delta E_L = \Delta L_{kin}\bar{I}^2$, where ΔL_{kin} is the laser-induced change in kinetic inductance defined in Equation 2.35. The resistive one is given by $\Delta E_R = \Delta R\bar{I}^2\frac{1}{\kappa}$, where ΔR is the laser-induced change in effective resistance as defined in Section 2.5, and $1/\kappa$ is the characteristic time for a photon in resonator leaking into feed line. Then with laser perturbation, microwave power reflected from the sample is given by

$$\begin{aligned} P = \kappa(E + \Delta E_L - \Delta E_R) &= \kappa\left((L_m + L_{kin})\bar{I}^2 + \Delta L_{kin}\bar{I}^2 - \Delta R\bar{I}^2\frac{1}{\kappa}\right) \\ &= (\kappa(L_m + L_{kin} + \Delta L_{kin}) - \Delta R)\bar{I}^2\,. \end{aligned} \tag{4.10}$$

Then we have laser induced change in reflected microwave power

$$\Delta P = (\kappa\Delta L_{kin} - \Delta R)\bar{I}^2\,, \tag{4.11}$$

which is proportional to $\bar{I}^2$ as well, so it is proportional to input power P. Then the photo response is given by

$$PR = \Delta V_{out} = \frac{1}{2}\sqrt{\frac{R}{P}}\Delta P \propto \frac{\Delta P}{\sqrt{P}} \propto \frac{\bar{I}^2}{\sqrt{\bar{I}^2}} \propto P^{\frac{1}{2}}. \tag{4.12}$$

So we expect a square root dependence of PR on microwave power.

Theory also predicts that laser-induced changes in resonator properties should be independent from microwave power. The resonance angular frequency $\omega_0 = \frac{1}{\sqrt{(L_m+L_{kin})C}}$, where L_m and C are constants during the LSM measurement. Assuming small laser-induced change, the laser-induced change in ω_0 is

$$\Delta\omega_0 = \frac{1}{\sqrt{C}}\frac{\Delta L_{kin}}{(L_m + L_{kin})^{3/2}}, \tag{4.13}$$

which, by Equation 2.35, is proportional to

$$\Delta L_{kin} = -\frac{\Delta n_s}{n_s} F_{laser}(x,y) L_{kin}, \tag{4.14}$$

where function $F_{laser}(x,y)$ is a sort of current participation ratio, defined in Equation 2.35, which is microwave power independent. As L_{kin} is microwave power independent so is Δf_0. Similar argument applies to ΔQ_{int}.

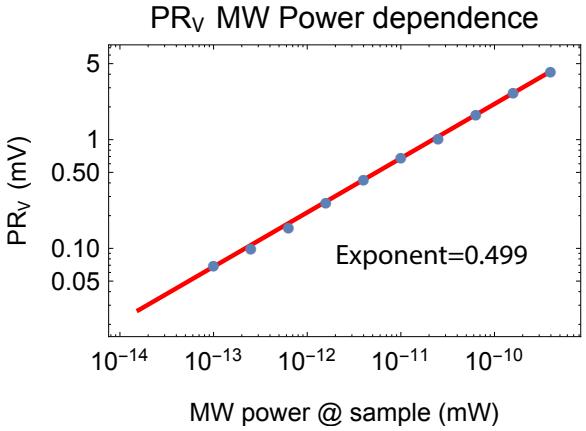

Figure 4.6: Log-log plot of microwave power dependence of voltage PR measured at 10.66 μW defocused laser power at sample and 4 K temperature. x axis is the RF power at sample in micro Watt. The red line is the power law fit, which gives an exponent around 0.5.

Figure 4.6 shows the voltage PR measured at different RF power under the condition of 10.66 μW laser power at sample, defocused laser and 4 K temperature in log-log plot, where RF power at sample is expressed in micro

Watt. The straight pattern on log-log plot in Figure 4.6 is a signature of power law, and the power law fitting fives a power very close to 0.5, which is exactly the value predicted by theory.

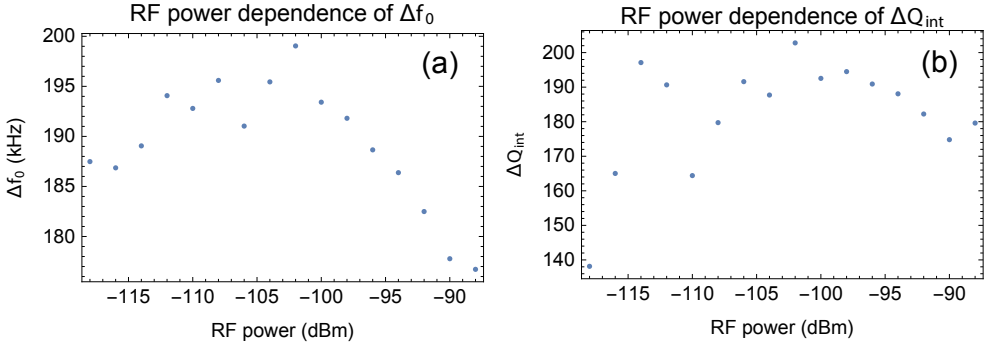

Figure 4.7: Laser-induced changes in resonator properties as a function of microwave power measured at 3.5 K, and defocused laser with 10.66 μW power at sample. (a) Δf_0; (b) ΔQ_{int}

We also extract Δf_0, the laser-induced shift of resonance frequency, and ΔQ_{int} by measuring PR_p under the condition of defocused laser, 10.66 μW laser power at sample, and 3.5 K temperature. The result is shown in Figure 4.7. Neither Δf_0 nor ΔQ_{int} shows clear dependence on microwave power, which matches theoretical prediction.

4.3 Laser Intensity Dependence of PR

Photons break Cooper pairs into quasiparticles. The changes in Cooper pair and quasiparticle density result in photo response. The more photons are absorbed by superconductor, the bigger the laser-induced change. So increasing laser intensity is a straightforward way to increase magnitude of photo response. However, laser-induced heating might be harmful to our experiment at low temperatures, which motivates us to reduce laser power. To understand the effect of laser intensity on PR, we conducted measurements on laser intensity dependence of PR.

Figure 4.8 shows the laser power dependence of voltage PR under the condition of -94 dBm RF power at sample, 3.5 K temperature and focused laser. An unexpected saturation behavior at high laser power is observed. As shown in Section 4.1, this laser power with focused laser beam cannot break all Cooper pairs locally, so the saturation is not an effect of breaking all Cooper pairs. There is also some non-trivial structure at low laser power. The slope of PR as a function of laser power increases from 10 μW to 15 μW before saturation. The reason may be related to the detailed dynamics

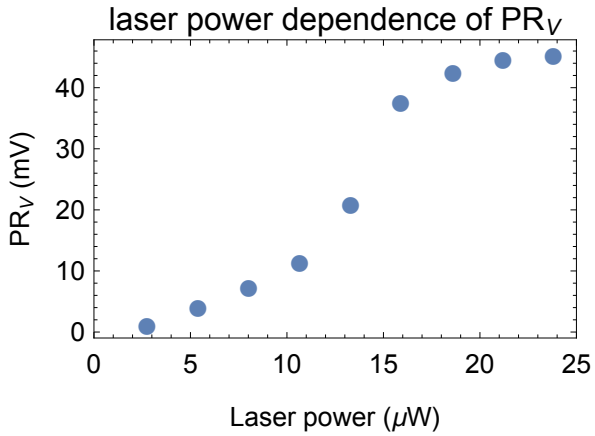

Figure 4.8: Laser power dependence of voltage PR measured at -94 dBm RF power at sample and 3.5 K with focused laser. The laser power in the plot is laser power at sample.

of quasiparticles and Cooper pairs at the edge of stripelines due to some geometric effects [11].

We also extracted the laser-induced change of the resonator properties at different laser power under the condition of -94 dBm RF power at sample, 3.5 K temperature and defocused laser. In this study, no saturation was observed. The result of extracted Δf_0 and $\Delta\gamma$ is shown in Figure 4.9, where both of them show linear dependence on laser power. So we can conclude that in the laser power range of this experiment, the ratio between photo response components does not change.

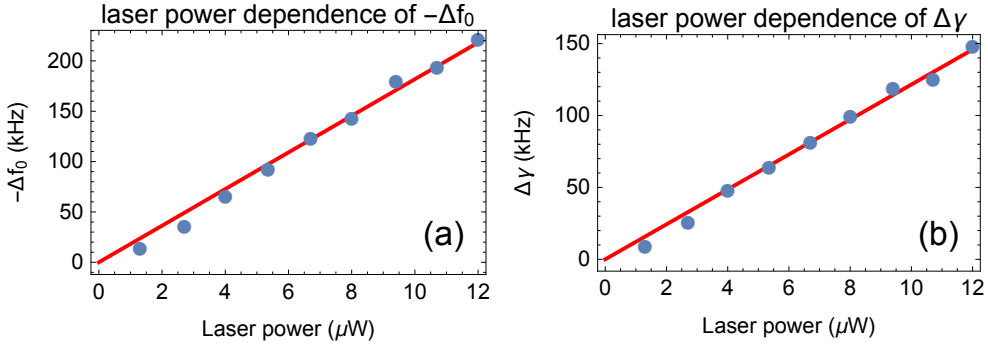

Figure 4.9: Laser-induced change of lumped element resonator vs laser power, with defocused laser at 3.5 K. (a) Δf_0; (b) $\Delta\gamma$.

The fitted slope of laser power dependence of $-\Delta f_0$ is 18.2 kHz/μW, of $\Delta\gamma$ is 12.2 kHz/μW. From the fittings, one can estimate some of the fundamental properties of the illuminated superconductor, like characteristic quasiparti-

cle recombination time τ_{qp}. According to Equation 4.5 and 4.6, the slope of laser power dependence of $-\Delta\omega_0$ can be written as

$$-\frac{\partial\Delta\omega_0}{\partial P_{laser}} = \frac{1}{4}\frac{1}{\sqrt{C}}\frac{\mu_0^2 e^2 \lambda_L^2 \eta \tau_{qp}}{E_g m_e W^2 (L_m + L_{kin})^{3/2}}\,. \tag{4.15}$$

Solving this equation, the estimated $\tau_{qp} = 300$ ns. The accuracy of this value is limited by the accuracy of theoretical model and the accuracy of parameters other than τ_{qp}.

4.4 Temperature Dependence of Photo Response

Operating LSM at quantum limited microwave power requires putting the sample into dilution fridge, which has a typical temperature of 20 mK, which is much lower than the operating temperature in this thesis. To estimate the effect at low temperature, measuring temperature dependence of photo response is necessary.

Temperature has multiple effects on photo response. The first effect of temperature is changing density of superconducting electrons, which is valid even when laser is absent. Please recall Equation 2.8 for the temperature dependent London penetration depth. Compared to Equation 2.6, the London penetration depth at zero temperature, we can conclude the temperature dependence of density of superconducting electrons

$$n_s(T) = n_s(0)\left(1 - \left(\frac{T}{T_c}\right)^4\right), \tag{4.16}$$

where $n_s(0)$ is the density of superconducting electrons at zero temperature, which is simply the density of free electron in Niobium, and T_c is the critical temperature. n_s decreases and quasiparticle density $n_{qp} = n - n_s$ increases as temperature approaches T_c, which will increases both real and imaginary part of surface impedance of superconductor given by Equation 2.13, that is, increases both resistive loss and kinetic inductance. Thus, increasing temperature decreases Q_{int} and ω_0 even without applying laser. The second effect of temperature is changing the gap energy E_g of superconductor. Actually the temperature dependence of superconducting gap energy is closely related to the temperature dependence of n_s, because temperature influences both thermal energy available to break Cooper pairs and the minimum energy required to break one. Superconducting gap energy is the order parameter of superconductor, which is maximum at zero temperature and monotonically decreases as temperature increases, and finally vanishes

at T_c. Increasing temperature in LSM means increasing the number of quasiparticle produced by one photon, which is directly related to Δn_s in photo response theory. Temperature also has influence on optical length, but as we are not interested in complex photo response in this study, we will not discuss this here.

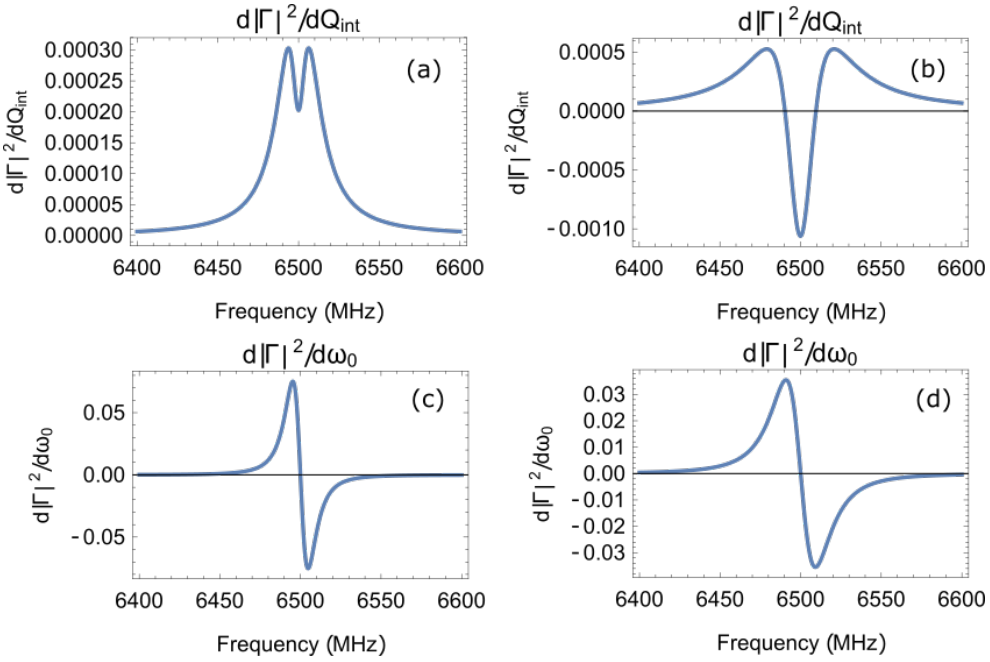

Figure 4.10: $\frac{\partial|\Gamma|^2}{\partial Q_{int}}$ and $\frac{\partial|\Gamma|^2}{\partial \omega_0}$ at overcoupled and undercoupled condition. All the plots share the same $\kappa = 10$ MHz, and the same $\omega_0 = 6.5$ GHz, but with different internal Q factor: (a) $\frac{\partial|\Gamma|^2}{\partial Q_{int}}$ with $Q_{int} = 1000$; (b) $\frac{\partial|\Gamma|^2}{\partial Q_{int}}$ with $Q_{int} = 300$; (c) $\frac{\partial|\Gamma|^2}{\partial \omega_0}$ with $Q_{int} = 1000$; (d) $\frac{\partial|\Gamma|^2}{\partial \omega_0}$ with $Q_{int} = 300$.

Among the effects of temperature, influence on n_s has various effects on PR amplitude. Different n_s lead to different Q_{int}, and different Q_{int} gives different behavior of partial derivatives of $|\Gamma|^2$. Figure 4.10 shows the behaviors of $\frac{\partial|\Gamma|^2}{\partial Q_{int}}$ and $\frac{\partial|\Gamma|^2}{\partial \omega_0}$ at overcoupled and undercoupled condition. In the simulation, $\omega_0 = 6.5$ GHz for all the plots, and $\kappa = 10$ MHz for all the plots, which leads to an $Q_{ext} = 650$, $\omega_0 = 6.5$ GHz for all the plots. Then (a) and (c) with $Q_{int} = 1000$ shows overcoupled case, while (b) and (d) with $Q_{int} = 300$ shows undercoupled case. There is no significant difference between $\frac{\partial|\Gamma|^2}{\partial \omega_0}$'s, but two $\frac{\partial|\Gamma|^2}{\partial Q_{int}}$'s behave quite different around resonance frequency. In undercoupled case, the value of $\frac{\partial|\Gamma|^2}{\partial Q_{int}}$ is always positive, while in overcoupled case, the value of $\frac{\partial|\Gamma|^2}{\partial Q_{int}}$ around resonance drops below zero. $\frac{\partial|\Gamma|^2}{\partial Q_{int}}(\omega_0) = 0$ when

the resonator is critically coupled.

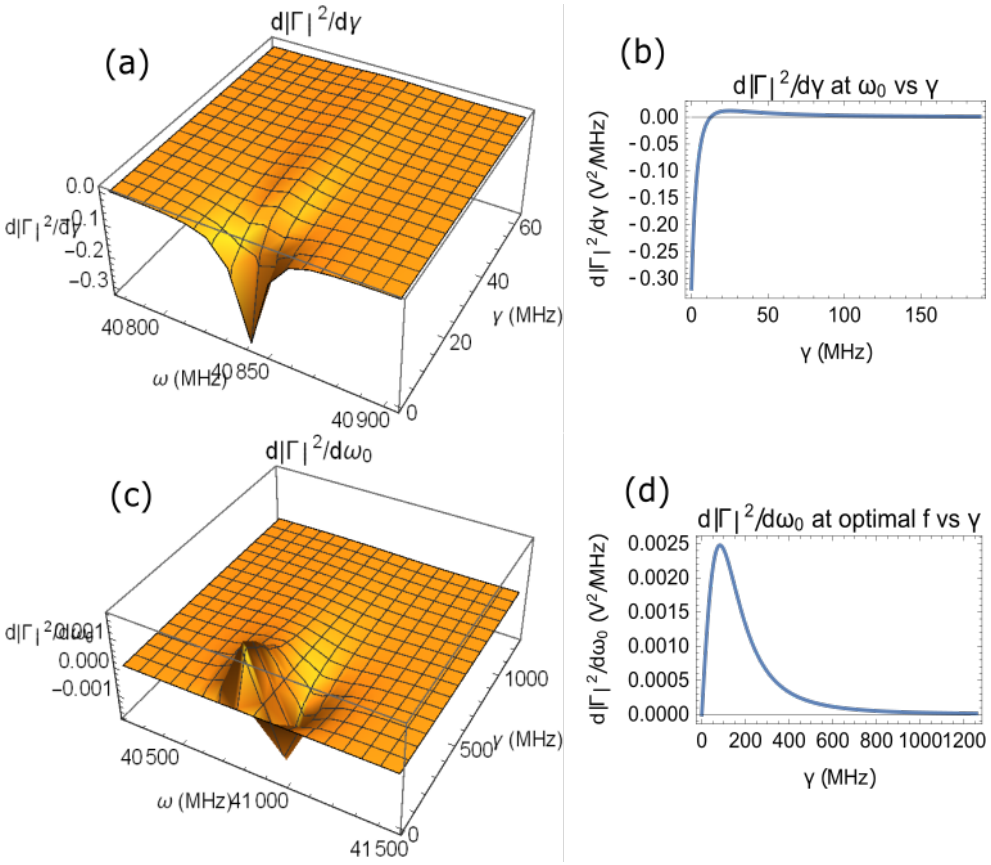

Figure 4.11: $\frac{\partial|\Gamma|^2}{\partial\gamma}$ and $\frac{\partial|\Gamma|^2}{\partial\omega_0}$ as functions of γ and ω. All the plots share the same $\kappa = 12.6$ MHz, and the same $\omega_0 = 2\pi \times 6.5$ GHz. (a) 3D plot of $\frac{\partial|\Gamma|^2}{\partial\gamma}$; (b) frequency slice of (a) at $\omega = \omega_0$; (c) 3D plot of $\frac{\partial|\Gamma|^2}{\partial\omega_0}$; (d) frequency slice of (c) at the frequency where $\frac{\partial|\Gamma|^2}{\partial\omega_0}$ has maximum value.

Apart from the feature of the two partial derivatives, the magnitudes of them are also different. Figure 4.11 shows the 3D plots of $\frac{\partial|\Gamma|^2}{\partial\gamma}$ and $\frac{\partial|\Gamma|^2}{\partial\omega_0}$. If we ignore the temperature related change of resonance frequency, we can consider γ axis in 3D plots as a measure of temperature. The higher the temperature is, the higher the γ. Then from the plots, we can conclude that at high temperature, $\frac{\partial|\Gamma|^2}{\partial\gamma}$ is suppressed, while $\frac{\partial|\Gamma|^2}{\partial\omega_0}$ is still finite (the γ at 8 K is around 250 MHz in our case, where $\frac{\partial|\Gamma|^2}{\partial\omega_0}$ is still finite). The magnitude of $\frac{\partial|\Gamma|^2}{\partial\gamma}$ has a dramatic increase at low temperatures, while $\frac{\partial|\Gamma|^2}{\partial\omega_0}$ vanishes. Because of the different behavior of partial derivatives, temperature dependence of PR has complicated feature.

We can predict the behavior of $\Delta\omega_0$ from theory. As $\omega_0 = 1/\sqrt{C(L_m + L_{kin})}$, assuming small laser-induced change in L_{kin}, we have

$$\begin{aligned}\Delta\omega_0 &= -\frac{1}{2}\frac{1}{\sqrt{C}}\frac{\Delta L_{kin}}{(L_m + L_{kin})^{3/2}} = -\frac{1}{2}\frac{1}{\sqrt{C}}\frac{\frac{\Delta n_s}{n_s - \Delta n_s}F_{laser}(x,y)L_{kin}}{(L_m + L_{kin})^{3/2}} \\ &= -\frac{1}{2}\frac{1}{\sqrt{C}}\frac{\frac{\Delta n_s}{n_s(n_s - \Delta n_s)}F_{laser}(x,y)\frac{m_e l}{e^2 A}}{(L_m + \frac{1}{n_s}\frac{m_e l}{e^2 A})^{3/2}} \\ &= -\frac{1}{2}\frac{1}{\sqrt{C}}\frac{\Delta n_s F_{laser}(x,y)\frac{m_e l}{e^2 A}}{(1 - \Delta n_s/n_s)(n_s^{4/3}L_m + n_s^{1/3}\frac{m_e l}{e^2 A})^{3/2}}.\end{aligned} \tag{4.17}$$

From this equation, if $\Delta n_s < n_s$ we expect a monotonically increasing behavior of $|\Delta\omega_0|$ as n_s decreases, which is equivalent to a monotonically increasing behavior of $\Delta\omega_0$ as a function of temperature, and $\Delta\omega_0$ should diverge at the temperature where $\Delta n_s = n_s$.

We can also predict the behavior of $\Delta\gamma$ from theory. According to Equation 2.46, 2.47 and 2.48, not necessarily in small Δn_s limit, we have

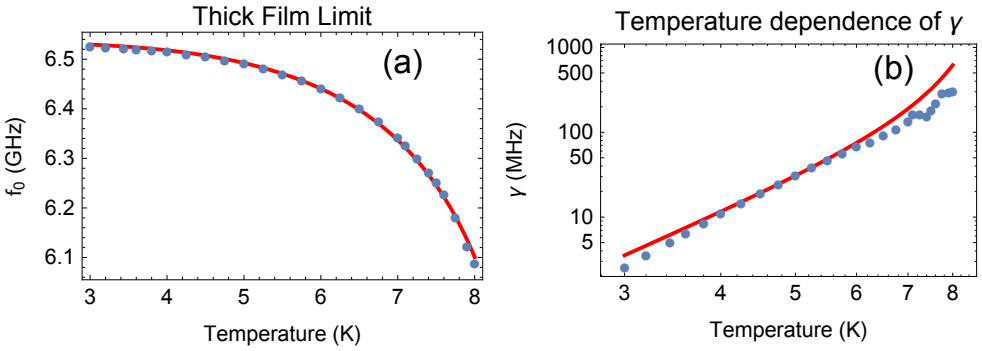

Figure 4.12: Temperature dependence of different resonator properties and photo response with focused laser. (a) f_0 and its thick film limited fitting; (b) γ and its power law fitting in log-log scale with exponent 4.7.

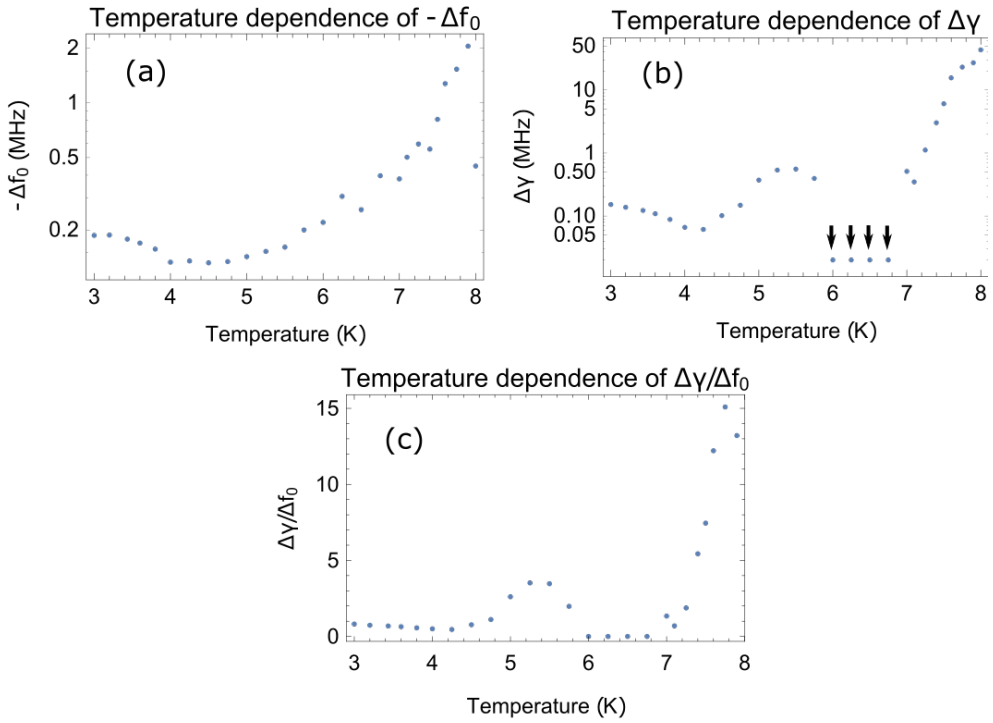

Figure 4.13: Temperature dependence of different resonator properties and photo response with focused laser. (a) Δf_0; (b) $-\Delta\gamma_0$, where the points pointed by arrows are below the lower bound of plot range; (c) $-\Delta\gamma/\Delta f_0$.

$$\begin{aligned}\Delta\gamma =& \frac{(n_s-\Delta n_s)^{-3/2}(n-(n_s-\Delta n_s))-n_s^{-3/2}(n-n_s)}{n_s^{-3/2}(n-n_s)}F_{laser}(x,y)\gamma \\ =& \left(\left(\frac{n_s}{n_s-\Delta n_s}\right)^{3/2}\frac{(n-(n_s-\Delta n_s))}{n-n_s}-1\right)F_{laser}(x,y)\frac{\frac{1}{2}\frac{l}{w}\omega^2\mu_0^2\lambda_L^3(T)\frac{(n-n_s)e^2\tau}{m_e(1+\omega^2\tau^2)}}{L_m+\mu_0\lambda_L(T)\frac{l}{w}} \\ \propto& \left(\left(1+\frac{\Delta n_s}{n_s-\Delta n_s}\right)^{3/2}\frac{(n-(n_s-\Delta n_s))}{n-n_s}-1\right)F_{laser}(x,y)\frac{n-n_s}{L_m n_s^{3/2}+an_s},\end{aligned} \tag{4.18}$$

where $a=\sqrt{\frac{m_e\mu_0}{e^2}}\frac{l}{w}$ as defined in Section 2.5. In the equation above

$$\left(1+\frac{\Delta n_s}{n_s-\Delta n_s}\right)^{3/2}\frac{(n-(n_s-\Delta n_s))}{n-n_s}-1>0 \tag{4.19}$$

for all temperature, because $\Delta n_s>0$ in our convention and $n-n_s>0$. Then $\Delta\gamma$ is a monotonically increasing function of temperature and diverges at the

temperature where $\Delta n_s = n_s$. In summary, theory states that both $\Delta\omega_0$ and $\Delta\gamma$ are monotonically increasing function of temperature, and diverge at the temperature where $\Delta n_s = n_s$.

Now we can have a look at experimental results. Figure 4.12 shows the temperature dependence of resonator properties, and 4.13 the photo response with focused laser. Temperature dependence of ω_0 has already been discussed in Section 4.1. Figure 4.12 (b) shows the temperature dependence of γ and its fitting using temperature dependence law given by two fluid model

$$\gamma \propto n_s^{-3/2}(n - n_s) \propto \left(1 - \left(\frac{T}{T_c}\right)^4\right)^{-3/2} \frac{T^4}{T_c^4}. \tag{4.20}$$

The fitting matches experimental data well, except the points at temperature below 3.2 K and above 7 K. The deviation comes from the inaccuracy of temperature dependence given by two fluid model. The temperature dependence of superconducting electron density predicted by BCS theory can by found in reference [36], which is more complicated.

The case is a bit different for laser-induced changes. Both $-\Delta f_0$ and $-\Delta\gamma$ blow up at high temperature as expected, but the decreasing behavior of $-\Delta f_0$ as a function of temperature at low temperature and the non-monotonic behavior of $-\Delta\gamma$ at temperature from 4 to 7 K are not predicted by our model. The behavior of $-\Delta f_0$ at low temperature can be explained by longer recombination time of quasiparticles. Interestingly, $\Delta\gamma$ drops to zero from 6 to 7 K, due to the constrain $\Delta\gamma > 0$ in the fitting. If we fit the data without constrain, $\Delta\gamma$ will drop below zero, which can never be true if our basic theory holds in general, because it means breaking Cooper pairs using laser reduces the loss in resonator.

It is helpful to look into the fittings at this point, which can reflect more about experimental data and our model. Figure 4.14 shows the $|\Delta|\Gamma|^2|$ data and its fitting at different typical temperatures. From 3 K to 4 K, the lower frequency peak is higher than the higher frequency peak, due to the addition of two PR components (see Chapter 3 for detail). In this temperature range, the model fits data well. From 4 K to 5 K, the higher frequency peak is higher than lower frequency peak. However, this cannot be reproduced by our model with positive $\Delta\gamma$ and negative Δf_0. Thus resistive contribution to PR is highly suppressed in fitting result. In Figure 4.13 (b), points are close to zero in this temperature range. From 5 K to 6 K, the higher frequency peak is still higher, but the model is able to fit this feature with a positive $\Delta\gamma$ as in the temperature range from 3 K to 4 K. From 6 K to 6.75 K, the relative height of the peaks reversed again. This time, the fitting returns an

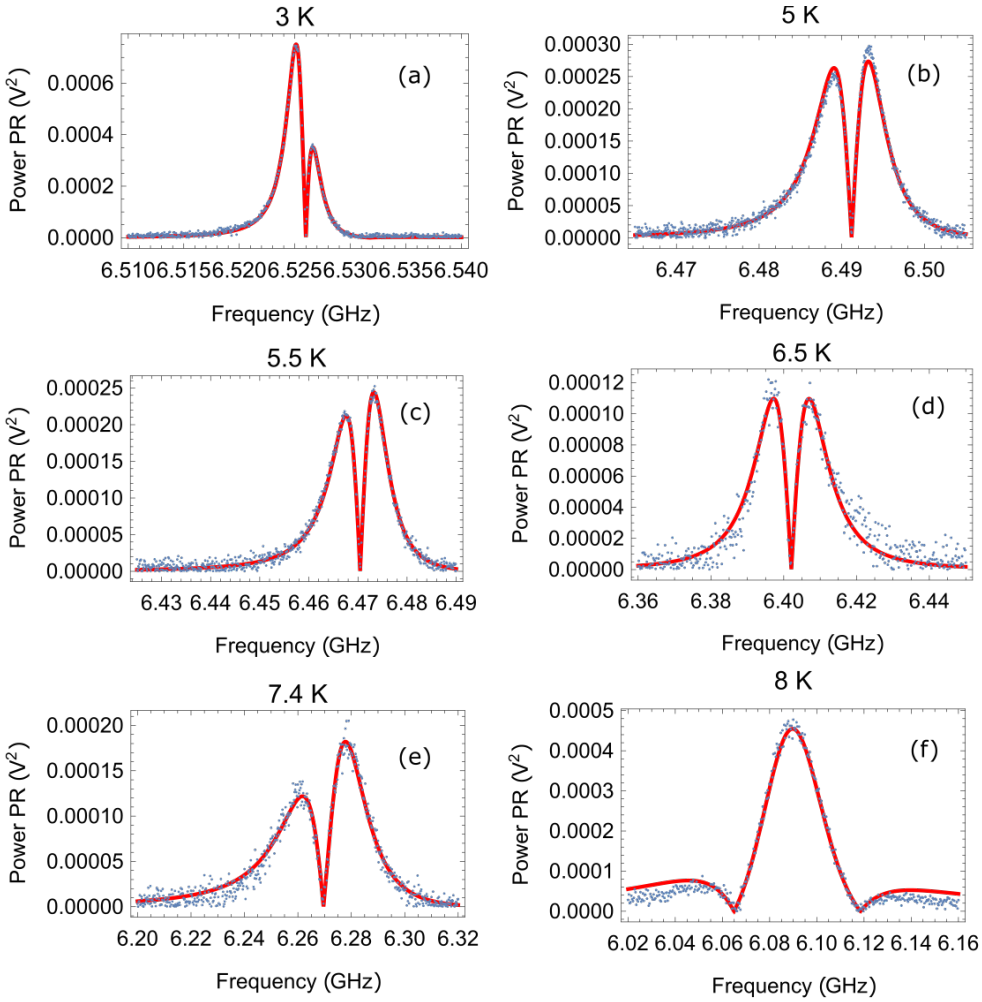

Figure 4.14: $|\Delta|\Gamma|^2|$ data (blue dots) and its fitting (red curve) at different typical temperatures. (a) 3 K; (b) 5 K; (c) 5.5 K; (d) 6.5 K; (e) 7.4 K; (f) 8 K.

unphysical negative $\Delta\gamma$, if there is no constrain on fitting condition. When temperature is above 7 K, the higher frequency peak is higher again, and can be fitted with physical laser-induced changes. Finally, at 8 K, resistive like contribution dominates the shape of PR_p. From Figure 4.14 (b) and (d), it is clear that the unphysical laser-induced changes are given by experimental data, not only poor fitting process. If the data is trustworthy, it will infer physics beyond our model. In fact, the data has reliable reproducibility.

Among the peak height reversals around 4 K, 5.25 K, 6 K, and 7 K, our model only captures the one around 5.25 K. To see the reason, we simulate PR_p with γ =2.6, 27, 47, and 92 MHz, which correspond to 3 K, 4.75 K, 5.5 K and 6.5 K respectively. The simulation results are shown in Figure 4.15. In the simulation, we take $\kappa = 13.5$ MHz, which is close to the real value,

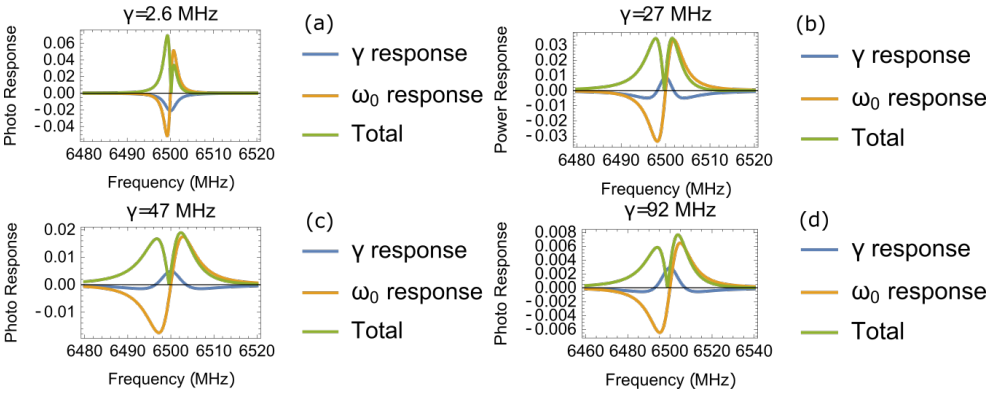

Figure 4.15: Simulation of PR_p at different γ.

$f_0 = 6.5$ GHz, which makes little difference on the properties we are interested in. $\Delta\omega_0$ and $\Delta\gamma$ are take some reasonable values with $\Delta\omega < 0$ and $\Delta\gamma > 0$.

In the simulation, there is only one peak height reversal, the one between simulations with $\gamma = 7$ MHz and $\gamma = 47$ MHz, corresponding to the reversal around 5.25 K. Noticeably, in Figure 4.15 (d), the higher frequency peak of $|PR_p|$ is higher, which is a clear difference from Figure 4.14 (d). The reason for the inconsistency might be poorly calibrated FPGA, which prevent us from extracting the correct κ and γ, large laser-induced change, which makes derivative method shown in Figure 4.15 a poor estimation, and laser heating, which modifies γ.

4.5 Defocus of Laser Beam

So far, all the studies in laser scanning microscopy use highly focused laser, which is able to resolve the details of the microwave elements. However, in some cases, detailed current distribution is not significant for known element (e.g. when we are measuring the resonance modes of coupled resonator systems). Shining highly defocused laser on the whole inductor allows performing the measurement faster.

Defocused laser beam yields spatial-insensitive photo response. This is valuable for wide range scanning study, because there is non-negligible error in the position of step scanner of Attocube piezos, and one would need the position data to optically inspect for line alignment. By comparing the position given by the step scanner and the optical image of a resonator, we conclude that the errors in step scanner position can be up to 6 μm, which is twice of the stripe width. However, the spatial profile of photo response given by a highly defocused beam (shining on the whole inductor) is spatially insen-

sitive. The photo response profile of an inductor acquired by ASC method using Q quadrature can be found in Figure 4.16, where photo response on the narrower vertical direction has a range of relatively flat spatial dependence about 50 μm, which is much larger than the step scanner position error. So the error in step scanner position is not a problem for defocus beam study.

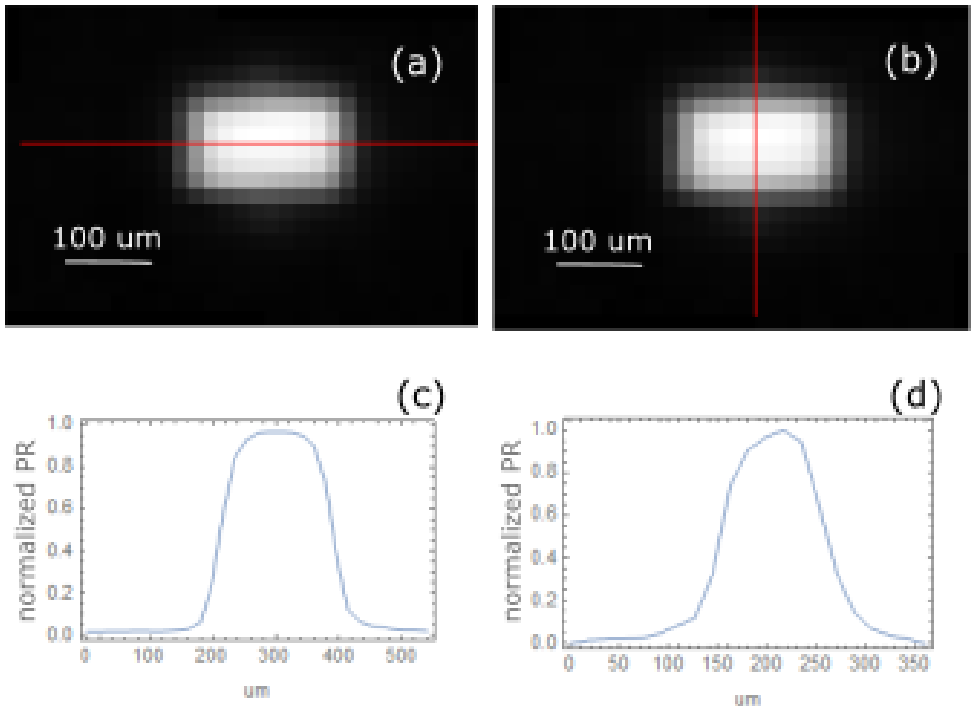

Figure 4.16: The defocus PR profile measured by ASC method using Q quadrature at frequency of maximum Q quadrature PR. Maximum PR is normalized to 1. (a) The red line shows the position of horizontal cut on the inductor; (b) the red line shows the position of vertical cut; (c) photo response along the horizontal cut line; (d) photo response along the vertical cut line.

Figure 4.17 shows the spatial scanning of PR and reflected light at different defocus distance. As defocus distance becomes larger, the contrast between inductor line and gap between them becomes more blurring. Due to different color scale, inductor lines become indistinguishable in reflection scan at smaller defocus distance than PR scan.

One would expect voltage PR changes with defocus distance, because some of the laser light from defocused beam shines into gap between stripes, which will reduce photo response. Let's refer to Equation 2.17 for a formal argument. The laser induced change in E_{kin} is given by

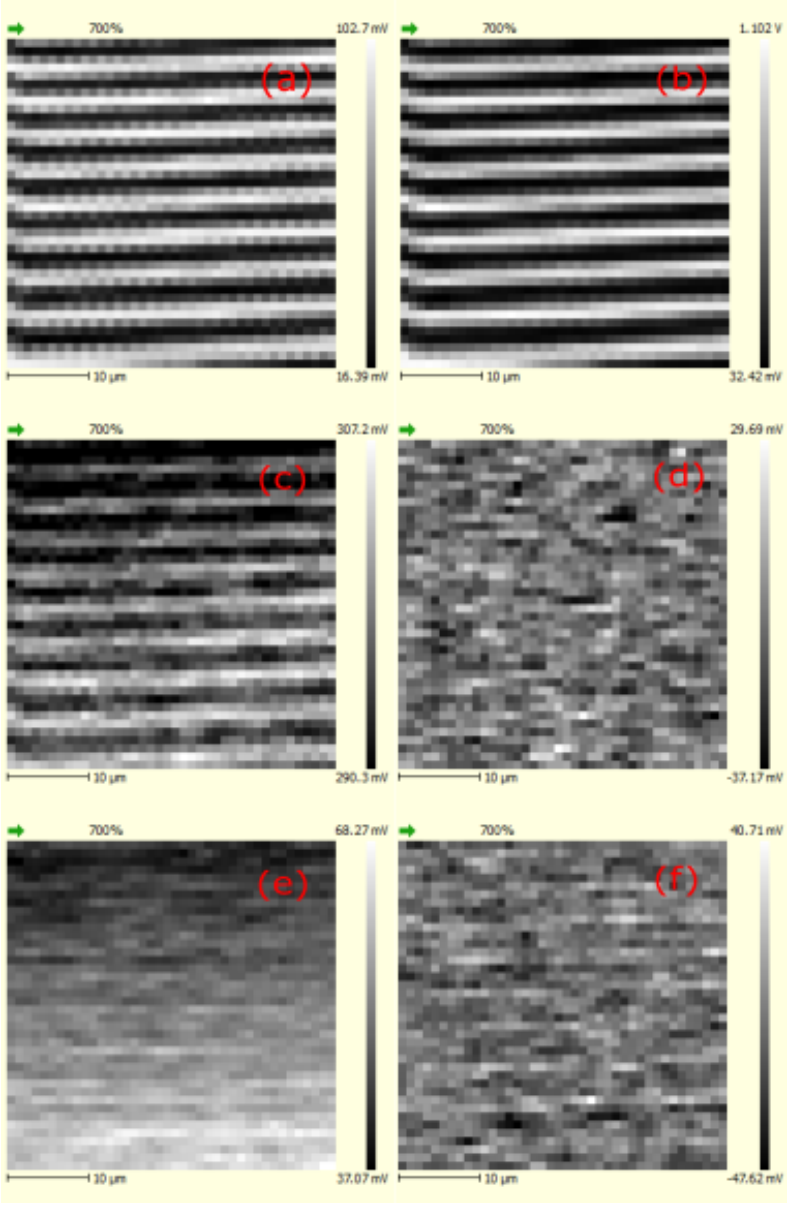

Figure 4.17: Spatial scanning of PR signal (on the left) and reflected light signal (on the right). (a), (c), (e) are PR scan at Z position 0, 40, 51 μm from focus; (b), (d), (f) are reflected light scan at the same position as corresponding PR scans on the left.

$$\Delta E_{kin} = \int_{V_{spot}} \frac{m_e \Delta n_s \vec{v}_0^2}{2} dV = \frac{m_e \vec{v}_0^2}{2} \int_{V_{spot}} \Delta n_s dV = \frac{1}{2} \Delta N_s m_e \vec{v}_0^2 . \qquad (4.21)$$

Where V_{spot} is the volume where n_s is changed by laser, and ΔN_s is the change in total number of superconducting electrons. Similar argument ap-

plies to laser induced change in dissipated energy. If we assume defocusing does not change the ratio of laser photons absorbed by the superconductor, we would expect ΔN_s dropping to half of the focused case when the laser is highly defocused, because half of the laser light shines on inductor lines. However, in practice, though the voltage PR changes with defocusing distance, it does not behave as expectation.

Figure 4.18 shows the defocusing distance dependence of ASC PR amplitude of Q port under the condition of 4 K temperature, -94 dBm RF power and 10.66 μW laser power at sample. From the plot, PR amplitude first drops to half of the focused value as defocusing increases, as expected; then it slowly increases to maximum value at around 200 μm from focus; then it starts to decrease slowly at higher distance. The decrease of PR amplitude at small defocusing distance can be explained by shining light into the gap between inductor lines, and the decrease at large defocusing distance is a result of shining laser out of inductor area. The increasing of PR amplitude in between is anti-intuitive.

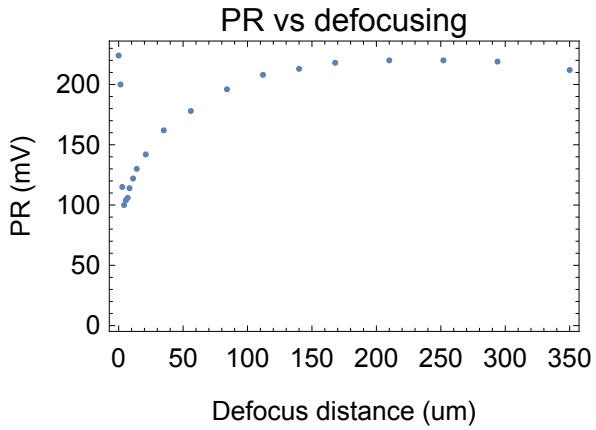

Figure 4.18: Defocusing distance dependence of PR amplitude measured by lock-in amplification method through Q port with 10.66 μW laser power.

A possible reason for the differences between focused and defocused laser is that they gives different proportion of ω_0 and Q_{int} response. We measured $\Delta|\Gamma|^2$ and extract Δf_0 and ΔQ_{int} at different defocusing distance at 4 K in order to verify the hypothesis. Figure 4.19 shows the frequency dependent $|\Delta|\Gamma|^2|$ curve at 4 K and its fitting with focused and highly defocused laser, where the two peaks in both (a) and (b) are of the same height and symmetric. This feature results from negligible Q factor contribution to the total photo response. $|\Delta|\Gamma|^2|$ curves at different defocus distances have the same feature, and the only evident difference is the height of the peaks. Then it is

enough to fit all the data with finite Δf_0 and zero ΔQ_{int}.

The result of defocusing distance dependence of Δf_0 is shown in Figure 4.20 (a). The general shape of Δf_0 is similar to that of PR amplitude in Figure 4.18, except some structures at small defocusing distance, which come from different starting points of defocusing. Δf_0 determines the magnitude of PR_p under this condition. To see this, we normalized every Δf_0 value in Figure 4.20 (a) by dividing it with the maximum value of the corresponding frequency dependent $|\Delta|\Gamma|^2|$ curve (e.g. a curve shown in Figure 4.19 (a)). The result is shown in Figure 4.20 (b), where there is no apparent defocusing distance dependence of normalized Δf_0. So at all defocusing distance at 4 K, photo response is determined by resonance frequency response, and resistive response is negligible.

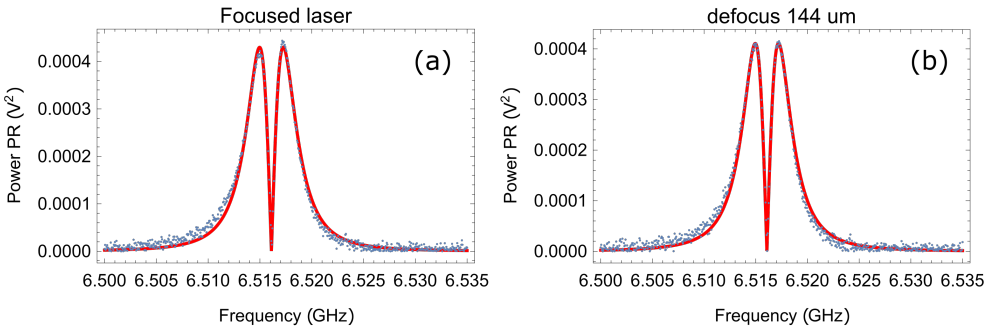

Figure 4.19: $|\Delta|\Gamma|^2|$ at 4 K with (a) focused laser, and (b) laser defocused by 144 μm.

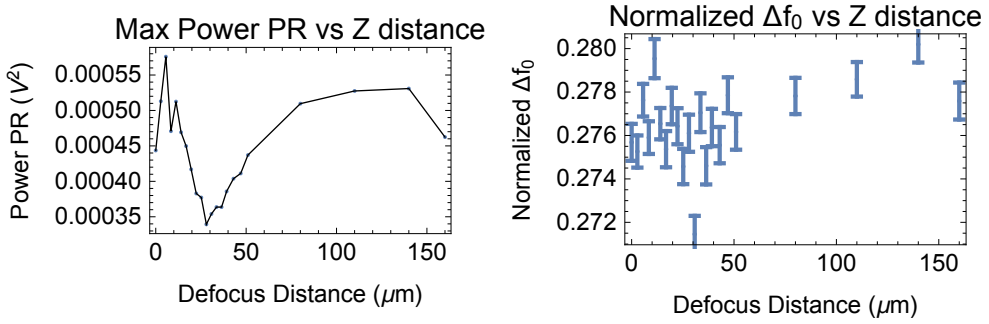

Figure 4.20: Defocusing distance dependence of (a) Δf_0 with almost invisible error bars given by mathematica fitting, and (b) normalized Δf_0 with error bars given by mathematica fitting.

We did not observe any defocusing distance related changes in the proportion of ω_0 and Q_{int} contributions to total PR at least at 4 K. The result might be biased by the fact that ΔQ_{int} is close to 0 at this temperature. Similar study at different temperatures is required to have a more complete under-

standing of defocusing, and the temperature study shows some evident of different PR proportion at temperature close to T_c. However, the increase in PR magnitude in the defocusing process is surely not a result of different proportion of contributions, because the effect is observed at 4 K.

Another possible explanation to the increase of PR magnitude in defocus study lies in dynamics of quasiparticles. If the laser is strong enough to break all the Cooper pairs around the laser probe, defocusing (i.e. increasing the area of laser spot) will increase the number of Cooper pairs broken by laser. However, as shown in Section 4.1, under our experimental condition, we estimated that laser cannot break all Cooper pairs locally.

Large current density passing through a superconductor can also break superconductivity. Here we estimate the current density in inductor lines, and compare the value with critical current density of superconducting Niobium film. The maximum current in the inductor is given by

$$I_{max} = \sqrt{\frac{2P_m}{\kappa(L_m + L_{kin})}}, \tag{4.22}$$

where P_m is microwave power at sample. Then the maximum current density in the inductor is given by

$$J_{max} = \frac{I_{max}}{S} = \frac{1}{tw}\sqrt{\frac{2P_m}{\kappa(L_m + L_{kin})}}, \tag{4.23}$$

where S is the effective cross section. By substituting $P_m = -94$ dBm, $L_m = 1.7 \times 10^{-9}$ H, $L_{kin} = 2.2 \times 10^{-10}$ H, $t = 150$ nm, and $w = 2$ μm, we have $J_{max} = 3 \times 10^7$ A/m^2, which is 2 orders of magnitudes smaller than 3×10^9 A/m^2, the critical current density of a superconducting Niobium film at liquid Helium temperature [37]. The current density in the inductor therefore does not significantly change Cooper pair density. We can now conclude that focused laser with power used in this study cannot break all the Cooper pairs locally even when the laser is focused. In fact, even if focused laser does break all the Cooper pairs locally, the number of laser-induced quasiparticle will saturate fast as we defocus the beam. Saturation of N_{qp} locally is not a solution to the increasing in PR magnitude during defocusing.

The final proposal of explanation is that focused laser heats the area under the laser spot, changes the local temperature. When laser is defocused, the heating effect becomes less significant locally, and the difference in temperature causes the difference in PR magnitude. We have seen in the temperature

dependence section that, at 4 K, when the temperature increases a bit, the magnitude of PR will decrease, which matches the general tendency of our defocusing plot. The drop of PR at small defocusing distance can again be explained by shining laser into the gaps. To be able to explain the amount of revival at large defocusing distance, dramatic laser-induced change in temperature is required (more than 1 K), which is larger than our expectation. However, this explanation is the best so far.

Defocused laser also has effects different from focused one in laser intensity and temperature dependence of PR.

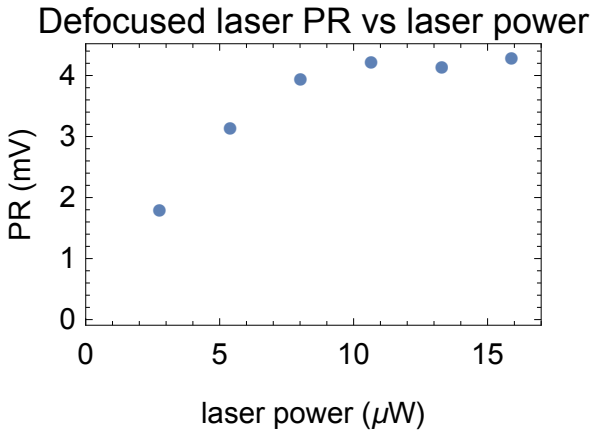

Figure 4.21: Laser power dependence of voltage PR measured at -94 dBm RF power at sample and 4 K with defocused laser. The laser power in the plot is laser power at sample.

Figure 4.21 shows the laser power dependence of voltage PR under the condition of -94 dBm RF power at sample, 4 K temperature and highly defocused laser. The data points show a saturation feature at high laser power the same as the focused laser data. However, at low laser power, there is no increase of PR slope observed.

Figure 4.22 and 4.23 show the results of PR temperature dependence experiment with -94 dBm RF power and 10.7 μW defocused laser on sample. Compared to focused laser case shown in Section 4.4, the basic properties of defocused laser behave the same. Laser-induced changes behave similarly at low temperature as well. However, at temperature close to T_c, defocused laser does not give prominent divergent behavior at high temperature as focused laser does, and the data points are noisy due to weak photo response magnitude. The differences come from the factor of $\frac{\Delta n_s}{n_s - \Delta n_s}$ in laser-induced changes of ω_0 and γ (refer to Equation 4.17 and 4.18), where both n_s and Δn_s are superconducting electron density and laser-induced change of it respectively in the laser-influenced region. The total numbers of broken Cooper

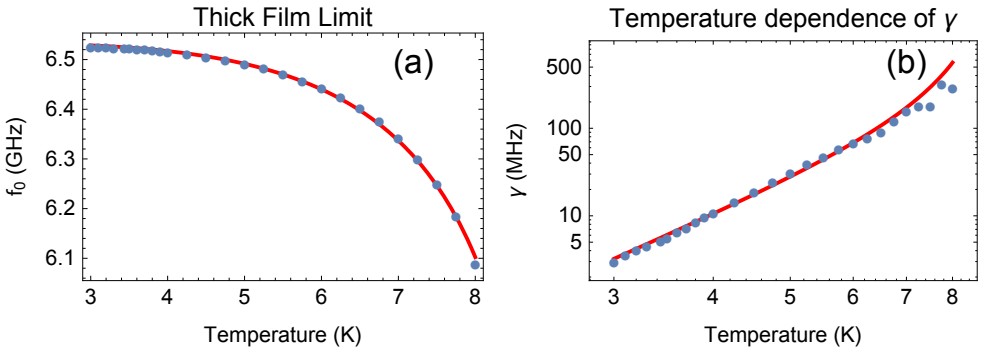

Figure 4.22: Temperature dependence of different resonator properties and photo response with defocused laser. (a) f_0; (b) γ.

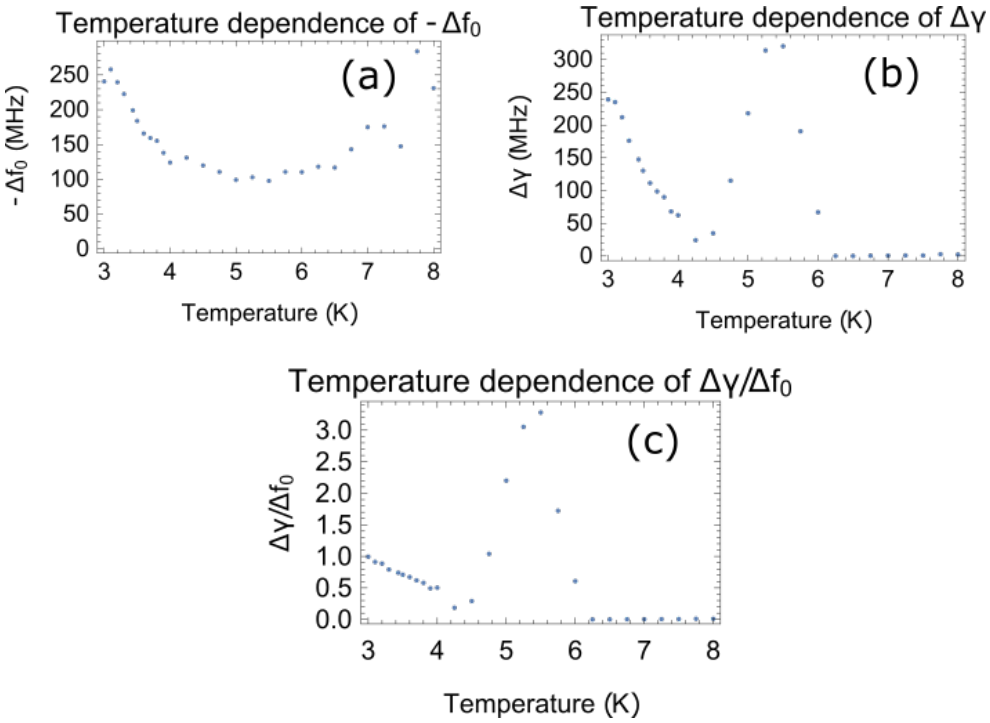

Figure 4.23: Temperature dependence of different resonator properties and photo response with defocused laser. (a) PR_p; (b) $-\Delta f_0$; (c) $-\Delta Q_{int}$; (d) $\Delta\gamma$; (e) $\Delta Q_{int}/\Delta f_0$; (f) $\Delta\gamma/\gamma$.

pairs are of the same order of magnitude in both focused laser and defocused laser cases. However, the focused laser generates all the quasiparticles in a small volume, leading to large Δn_s. When temperature approaches T_c, $\frac{\Delta n_s}{n_s - \Delta n_s}$ diverges as laser breaks all Cooper pairs locally. When the laser is defocused, laser-induced quasiparticles are distributed in the whole inductor, leading to small Δn_s. Thus, $\frac{\Delta n_s}{n_s - \Delta n_s}$ does not diverge in the experimental temperature range for defocused laser, and Δf_0 and $\Delta\gamma$ do not diverge either.

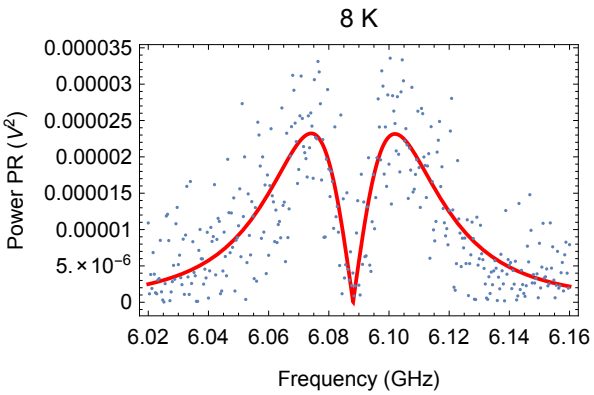

Figure 4.24: PR_p and its fitting for defocused laser at 8 K.

Chapter 5

Conclusions and Outlook

In this chapter, we will discuss the possibility of detecting photo response at 20 mK temperature with quantum limited microwave power or laser power, conclude the work in this thesis, point out possible experiment to improve our understanding of photo response, and possible application of LSM with current setup.

5.1 Possibility of Detecting Photo Response at Quantum limited Microwave Power and Laser Power

Operating LSM at quantum limited microwave power or laser power is one of the long term goals for LSM on superconducting lumped element resonator at this stage. With dilution fridge and quantum limited parametric amplifier, detecting photo response at quantum limited microwave power is achievable, while detecting optical photon quanta is not realistic with our current sample design and technique.

5.1.1 Laser Power and Microwave Power Map of Photo Response

In this section, we plot the map of PR as a function of both laser and microwave power. The data was acquired at 4 K, with defocused laser. The result is shown in Figure 5.1, which is just a smooth extension of Figure 4.6 and Figure 4.21.

As one of the long term goals is to operate LSM at quantum limited microwave power, we are interested in the question "at which microwave power do we still observe a photo response with current setup". To answer this question, we plot microwave power dependence of PR amplitude on several laser power slices. The result is shown in Figure 5.2, where the horizontal line is noise level at FPGA with 1024 averages, below which we

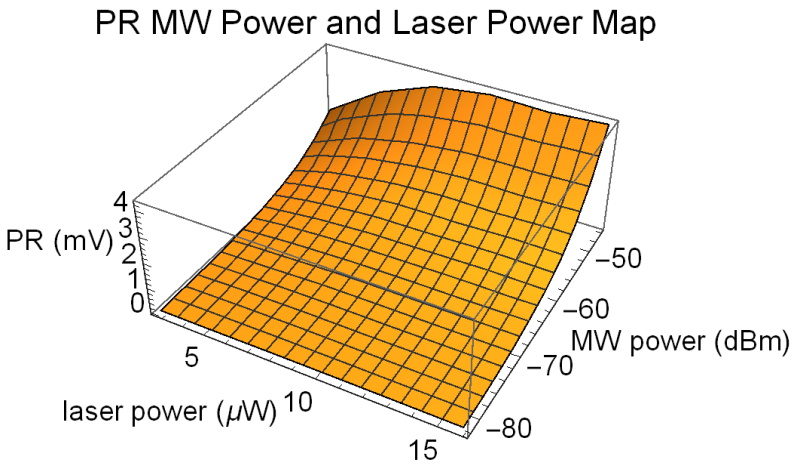

Figure 5.1: Laser power and microwave power map of photo response amplitude, measured at 4 K with defocused laser.

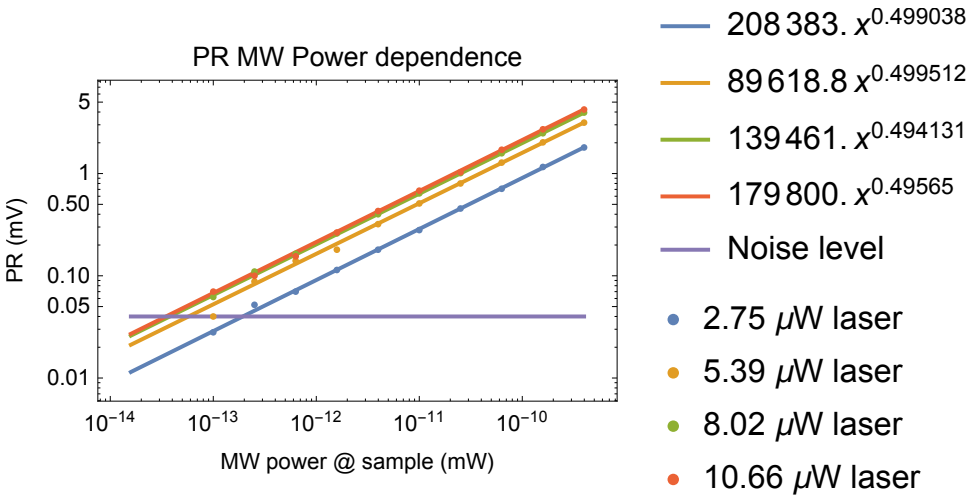

Figure 5.2: Microwave power dependence of PR amplitude at different laser power. The horizontal line is noise level at 1024 FPGA averages.

consider photo response is overwhelmed by noise. The power fit of the data points shows exponents close to 0.5 in all cases, which matches theoretical prediction very well. Quantum limited microwave power for our sample is 2.7×10^{-15} mW, which is smaller than any microwave power of the intersections in Figure 5.2. The result shows that in current setup, pr signal is dominated by noise at quantum limited microwave power.

5.1.2 Estimate Signal-to-Noise Ratio of Photo Response Measurement at 20 mK

In the previous subsection, we have seen that at 4 K, noise will overwhelm photo response signal at quantum limited laser power or microwave power. In this subsection, the possibility to detect photo response signal at 20 mK will be discussed.

For both microwave power and laser power calculations, we need noise level at 20 mK with quantum limited parametric amplifier, which has essentially zero amplification noise. In our lab, a typical detection chain gives 3 to 5 effective noise photons in a resonator at 20 mK [28, 38]. For reflection coefficient measurement at quantum limited microwave power, there is 1 signal photon in the resonator, which gives a signal-to-noise ratio around 0.25 in terms of photon number, at which detection of reflection coefficient is possible with reasonable number of averages.

With noise level at 20 mK, we can now estimate the noise of photo response measurements. Here, we estimate noise in $|PR| = |\Gamma_{off}| - |\Gamma_{on}|$ measurement, introduced in Subsection 3.3.1 and Subsection 3.3.3, and noise in $|PR_{sq}|$ measurement introduced in Subsection 3.3.4. Noise propagation equations used in estimation can be found in reference [39]

For $|PR|$, error estimation is straightforward:

$$\sigma_{PR} = \sqrt{\sigma^2_{|\Gamma|_{off}} + \sigma^2_{|\Gamma|_{on}}} = \sqrt{2\sigma^2_{|\Gamma|}}\,, \tag{5.1}$$

by substituting $\sigma_{|\Gamma|} = 4$ photons, we have $\sigma_{PR} = 6$ photons.

For $|PR_{sq}| = |\Gamma_{off}|^2 - |\Gamma_{on}|^2$, the case is more complicated, because error propagation in multiplication is involved. The usual equation for multiplication error propagation is for small error compared to signal. However, in our case, the error of $|\Gamma|$ measurement without averaging is comparable to signal. Then for $z = xy$, we have formula

$$z + \sigma_z = (x + \sigma_x)(y + \sigma_y) = xy + x\sigma_y + y\sigma_x + \sigma_y\sigma_x\,, \tag{5.2}$$

which leads to formula

$$\frac{\sigma_z}{z} = \frac{\sigma_x}{x} + \frac{\sigma_y}{y} + \frac{\sigma_x\sigma_y}{xy}\,, \tag{5.3}$$

where we cannot conclude the exact noise or signal-to-noise without information about signal level. However, due to the additional term $\frac{\sigma_x \sigma_y}{xy}$, we would expect a smaller signal-to-noise ratio in this case.

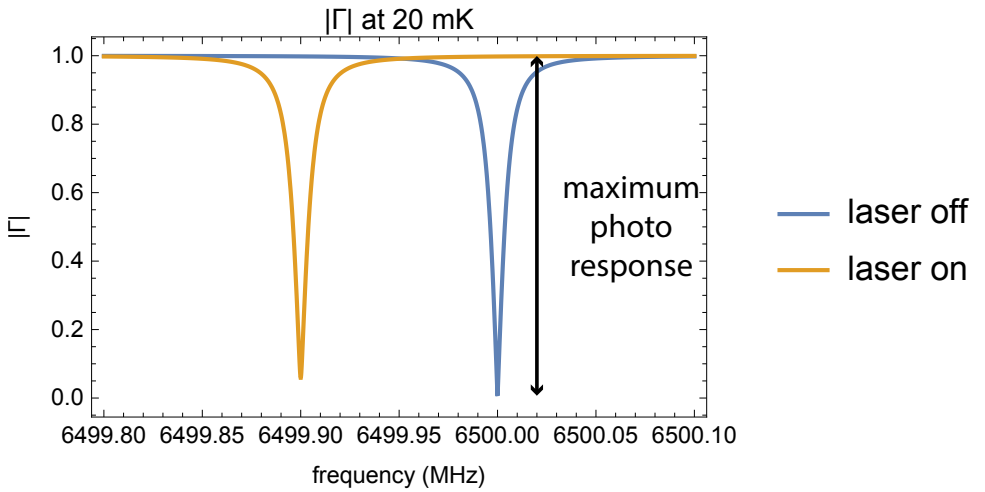

Figure 5.3: Sketch of $|\Gamma|$ at 20 mK in laser on and off case.

Now, we are ready to estimate signal-to-noise ratio at quantum limited microwave power and laser power. At first, we discuss the possibility of detecting photo response at quantum limited microwave power. At 20 mK, a typical value of internal energy loss rate is $\gamma = 40$ kHz. To make the resonators close to critically coupled to feed line, κ should be of the same order. Here, for simplicity, we take $\kappa = 40$ kHz. Then the resonance dip of reflection coefficient has a half bandwidth $(\kappa + \gamma)/2 = 40$ kHz. According to reference [33], the characteristic quasiparticle recombination time increases exponentially as temperature decreases, thus photo response should increases exponentially as well. However, as laser illumination gives an effective temperature and a quasiparticle lifetime, we only observed a modest increase of laser-induced change when temperature decreases from 4 K to 3 K, as shown in Figure 4.13. Here, we estimate the lower bound of signal-to-noise by assuming laser-induced change of resonance frequency and internal energy loss rate is the same as the case at 3 K, which are $\Delta\gamma = 152$ kHz and $\Delta\omega_0 = 1.2$ MHz with 10.66 μW laser power at sample. Please notice that in this case, the half bandwidth of reflection coefficient $(\kappa + \gamma)/2 = 40$ kHz $\ll$ $\Delta\omega_0 = 1.2$ MHz, where photo response amplitude is limited by the depth of the dip of $|\Gamma|$ at resonance frequency (refer to Figure 5.3). When the resonator is critically coupled to the feed line, the maximum photo response signal is equal to the baseline of Γ, which is one signal photon. Compare this value with noise of $|PR|$, the signal-to-noise ratio of $|PR|$ at 20 mK in terms of photon number with quantum limited microwave power is 0.18,

which can still give reasonable contrast if proper filter and averaging is applied. The above estimation is valid with smaller laser power, as long as $\Delta\omega_0 > \frac{\kappa+\gamma}{2}$, which provides the possibility of reducing laser intensity while still detect the same amount of photo response. We can estimate the minimal laser power with the power at which $\Delta\omega_0 = \frac{\kappa+\gamma}{2} = 40$ kHz. According to the linear relation between $\Delta\omega_0$ and laser power shown in Section 4.3, the minimum laser power $P_{Lmin} = 10.66 \times 40 \div 1200 = 0.36$ μW. We can conclude that it is possible to detect photo response with averaging and filtering at quantum limited microwave energy.

As for PR_{sq}, we can estimate $\frac{\sigma^2_{|\Gamma|}}{|\Gamma|^2}$ by substituting x and y in Equation 5.3 with one photon, and substituting σ_x and σ_y by 4 photons. Then we have $\frac{\sigma^2_{|\Gamma|}}{|\Gamma|^2} = 16$. Similar to $|PR|$ case, $\Delta\omega_0 \gg \frac{\kappa+\gamma}{2}$, so the maximum PR_{sq} signal is given by square of $|\Gamma|$ baseline. Then we have signal-to-noise ratio of PR_{sq} to be $1/(\sqrt{2}\frac{\sigma^2_{|\Gamma|}}{|\Gamma|^2}) = 0.044$, where $\sqrt{2}$ comes from error propagation in subtraction. The signal-to-noise ratio of PR_{sq} at quantum limited RF power is one order of magnitude smaller than that of $|PR|$. However, detecting reasonable contrast is still possible with averaging.

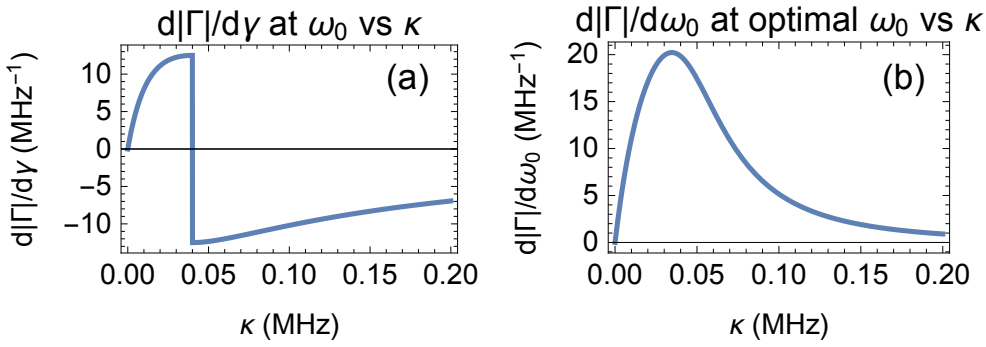

Figure 5.4: Partial derivatives of $|\Gamma|$ with $\gamma = 40$ kHz as a function of κ. (a) $\frac{\partial|\Gamma|}{\partial\gamma}$; (b) $\frac{\partial|\Gamma|}{\partial\omega_0}$.

The possibility of detecting single optical photon can be estimated similarly, with the assumption that laser-induced changes at 20 mK are 4 times of those at 3 K. Optical photon energy is quantized, so the effective laser power of a single photon is not single photon energy divided by one second, but divided by an effective time scale. There are two time scales playing an role in single optical photon detection, which are quasiparticle recombination rate $\tau_{qp} \approx 100$ ns and FPGA single shot measurement time $t_{FPGA} = 8192$ ns. The effective laser power is given by the longer time scale, which is $E_{photon}/t_{FPGA} = 4.9 \times 10^{-19}/8192 \times 10^{-9} = 6 \times 10^{-14}$ W. To increase the sensitivity of photon detection, we need to optimize κ.

Figure 5.4 shows $\frac{\partial|\Gamma|}{\partial\gamma}$ and $\frac{\partial|\Gamma|}{\partial\omega_0}$ with $\gamma = 40$ kHz as a function of κ. In both cases, the absolute values of the partial derivatives are maximum at $\kappa = \gamma = 40$ kHz, at which value $\frac{\partial|\Gamma|}{\partial\gamma} = 12.5$ MHz^{-1} and $\frac{\partial|\Gamma|}{\partial\omega_0} = 19.8$ MHz^{-1}. Apply the linear relation between laser power and $\Delta\omega_0$ and $\Delta\gamma$ and our assumption, we have $\Delta\omega_0 = 1.2 \times 10^6 \times 6 \times 10^{-14}/10.66 \times 10^{-9} = 7$ Hz and $\Delta\gamma = 150 \times 10^3 \times 6 \times 10^{-14}/10.66 \times 10^{-9} = 0.8$ Hz. Single-photon-induced changes of resonator properties are much smaller than half bandwidth of reflection coefficient dip, so the photo response amplitude detected by FPGA can be calculated by $b\left|\frac{\partial|\Gamma|}{\partial\gamma}\Delta\gamma + \frac{\partial|\Gamma|}{\partial\omega_0}\Delta\omega_0\right|$, where b is the effective baseline of ADC response at sample. Averaging is not allowed for single photon detection, so we assume photo response signal from a single optical photon should be at least 2 times of the noise level for a plausible detection event.

In the case of weak optical light power like single photon detection, statistical fluctuation of quasiparticle number at finite temperature due to generation and recombination can be a significant source of optical noise. The noise equivalent power is given by [40]

$$NEP_{g-r} = E_g\sqrt{\frac{N_{qp}}{\tau_{qp}}}, \tag{5.4}$$

which is proportional to the square root of quasiparticle number in the film volume interacting with optical light. At low temperature, a equation more accurate than 2.7 for quasiparticle density is given by [36]

$$n_{qp} = n_s(0) - n_s(T) = 2n_s(0)\int_{E_g/2}^{\infty}\left(-\frac{\partial f}{\partial E}\right)\frac{E}{(E^2-(E_g/2)^2)^{1/2}}dE, \tag{5.5}$$

where $f = 1/(e^{E/k_bT}+1)$ is the density of state of fermion. At 20 mK, n_{qp} is essentially zero, so generation recombination noise is not crucial in this case. Then, ignoring resistive response, the minimum baseline $b_{min} = 2\sigma_{PR}/(\Delta\omega_0\partial|\Gamma|/\partial\omega_0) = 0.01$ mV, which is equivalent to -87 dBm microwave power at sample. -87 dBm microwave power at sample is achievable, which indicates that single optical photon detection using superconducting lumped element resonator might be possible. However, one needs to make sure that the current density flowing through the resonator does not exceed the critical current density of Niobium film. For the current design of sample, assume the current density is distributed evenly through out the cross section, -87 dBm RF power gives a current density 2×10^5 A/m^2, which is smaller than the critical value 3×10^9 A/m^2 of a Niobium thin film.

Some measurements like PR measurement without averaging require higher signal-to-noise ratio. Signal-to-noise ratio can be further improved by reducing superconducting film thickness [11].

5.2 Conclusions and Outlook

Laser scanning microscopy provides ways to probe and tune the properties of superconducting resonators, which has the potential to become a powerful tool when encounters quantum information processing. In this thesis, the work on understanding and developing laser scanning microscopy on superconducting lumped element resonator is presented. Laser-induced change in kinetic inductance and internal loss rate of the superconducting resonator were found to be proportional to a participation ratio $F_{laser}(x,y) = \frac{\int f_{laser}(x,y) J_s^2 dxdy}{\int J_s^2 dxdy}$. Four ways of measuring photo response using FPGA or lock-in amplifier were developed and modeled. Two methods using FPGA allow extracting laser-induced changes in resonance frequency and internal quality factor at current stage. Laser power, microwave power, and temperature dependence of photo response were studied. Photo response and laser-induced changes in resonance frequency and internal loss rate are proportional to square root of microwave power, and increase with laser power, but the dependence is not trivial. The temperature dependence of photo response is not monotonic, but the behavior is more stable at low temperature. Defocusing laser beam is found to be a good way to perform quick scanning measurement and avoid error in position. Finally, conducting LSM at quantum limited microwave and laser power in dilution fridge is found to be possible, which opens the window of applying LSM in quantum information on superconducting circuits.

Before promoting the cooling system to dilution fridge and embracing potential new physics given by low temperature LSM, there are still some experimental and theoretical work, which may improve our understanding of photo response, needing to be done:

1. understand the reason for the difference between theory and experimental data;
2. understand the missing piece in the current model inferred by temperature study;
3. understand the difference between focused laser and defocused laser;
4. extract $\Delta\omega_0$ and $\Delta\gamma$ when laser probe is on island or ground plane;
5. change laser modulation frequency to probe the dynamics of quasiparticles;
6. spatial porfile study (see Appendix C for detail);

7. measure laser-induced resonance frequency shift using phase change;
8. apply new photo response measurement method to linear and circular chain of coupled resonators.

Apart from above studies, understanding the effect of dynamics of quasiparticles and Cooper pairs at laser spot is crucial for understanding the origin of photo response. Dynamics of charge carriers will also play an significant role at low temperature.

Appendix A

FPGA Settings for Photo Response Measurements

The FPGA settings for different photo response measurement are listed in the following table.

Measurement	SignalMath v01 (a_A, b_A, a_B, b_B)	AveragingMode	DiffMode
Static PR ($\|\Gamma\|$)	$(I1 + iQ1, 1, 1, 1)$	On	Off
$\|PR\|$ ($\|\Delta\Gamma\|$)	$(I1 + iQ1, 1, 1, 1)$	On	On
$\|PR_{sq}\|$ ($\|\Delta\|\Gamma\|^2\|$)	$(I1 + iQ1, I1 - iQ1, 1, 1)$	On	On

Appendix B

Signal-to-Noise Ratio of FPGA and ASC 500 Photo Response Measurement

Due to different amplification settings and data processing after the IQ mixer, FPGA and ASC 500 have different signal-to-noise ratio when they are used to measure photo response amplitude ($|PR|$). Knowing signal-to-noise ratio helps choosing the better measurement method when both of them satisfy the requirement.

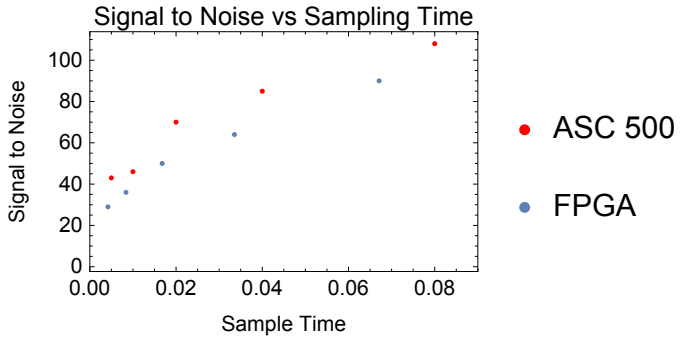

Figure B.1: Signal-to-noise ratios of FPGA and ASC 500 $|PR|$ measurements vs total sampling time of every data point.

The sampling rate of the built-in ADC in ASC 500 is 2.5 μs, while that of FPGA is 1 ns. The big difference in sampling rate infers that comparing signal-to-noise ratios at the same sample number is not proper. A proper comparison could be between signal-to-noise ratios at the same sampling time. The sampling time per data point of FPGA is $n \times 8.192$ μs, where n is the number of average, and 8.192 s is the measurement time window of FPGA. The sampling time per data point of ASC 500 is $n \times t_s$, where t_s is

the sampling time specified by Daisy software. Figure B.1 shows signal-to-noise ratios of FPGA and ASC 500 $|PR|$ measurements, measured in typical condition of photo response experiment. The signal-to-noise ratio of ASC 500 measurement is higher than that of FPGA with the same total sampling time. In fact, though the total sampling times are the same in the two cases, ASC 500 measurement takes much shorter time than FPGA, because the period of FPGA trigger is much longer than 8.192 μs, the measurement time window. So ASC 500 is the more time-favorable $|PR|$ measurement method.

Appendix C

Spatial Profile of Current Distribution

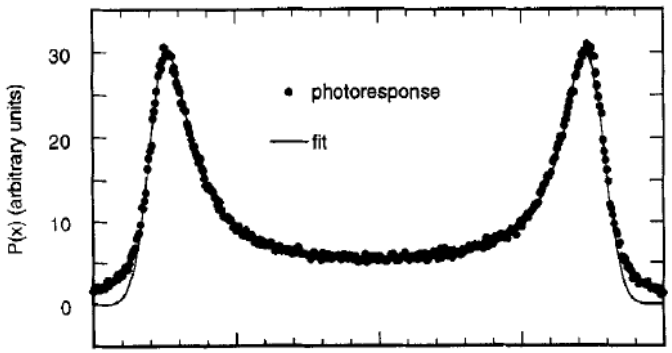

Figure C.1: Higher photo response is observed at edges of stripe. [1]

In previous works on laser scanning microscopy, people reported observing higher photo response at edges of stripe [1, 2, 4]. The phenomenon is a result of Meissner effect. However, in our experiment, this edge effect does not appear constantly. Sometimes, it appears in a microwave power window, but other times, it disappears from the whole sweeping range of microwave power, a spatial profile with maximum value at the center of the stripe appears instead. Even when the edge effect appears, the feature is not exactly the same as reported by other people. Figure C.2 shows the scanning image of inductor lines with and without edge effect. For the image with edge effect, the photo response to the edges does not increase as sharp as shown in Figure C.1.

We need more study to get the exact condition for edge effect to appear in our settings.

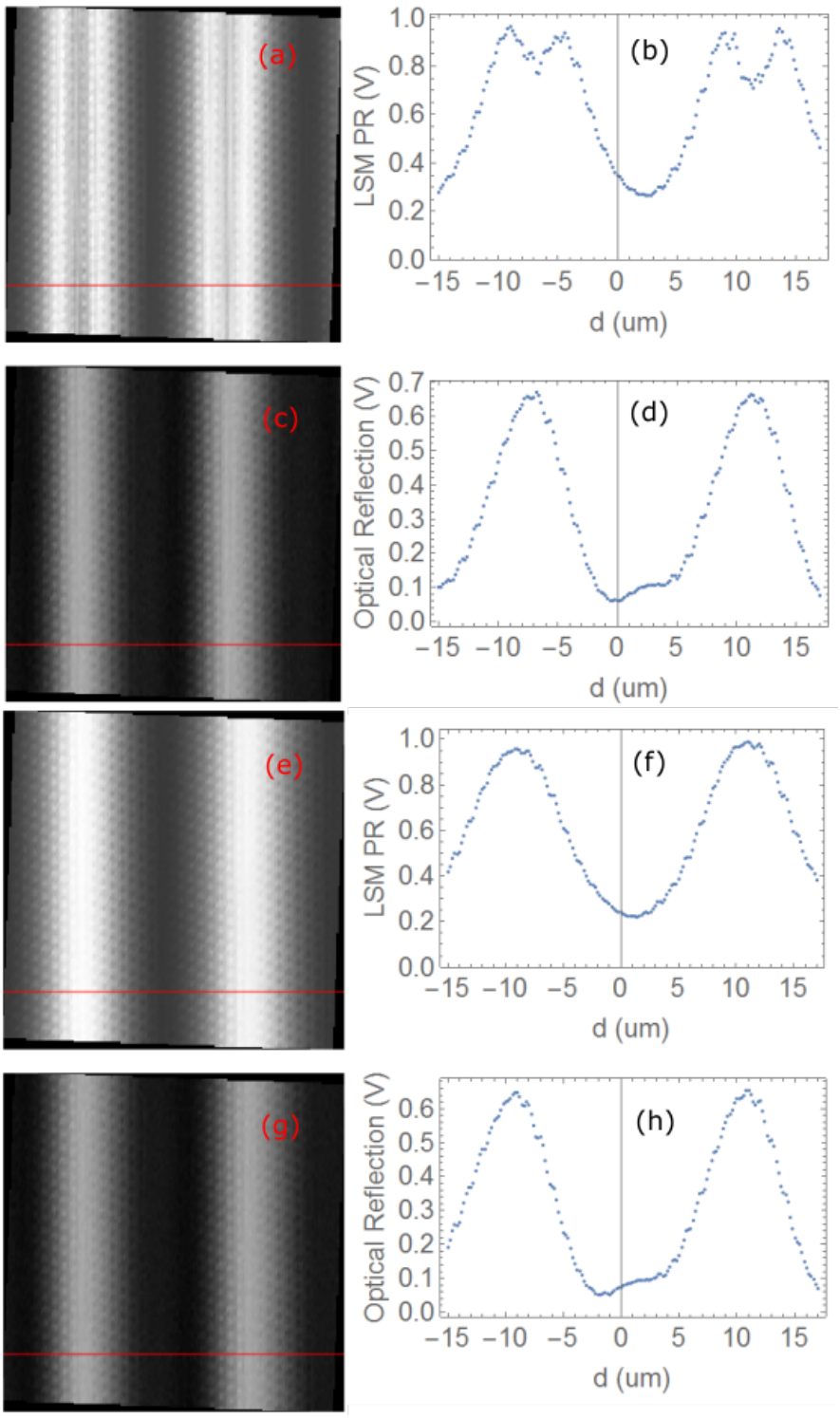

Figure C.2: Spatial scanning of optical images and ASC PR images. (a) and (c) are scanning images of the stripe with edge effect, where (a) is PR image, and (c) is optical image (reflects the spatial position of stripes). (b) and (d) are normalized average of PR and reflection signal along the stripe line respectively. Figure (e) to (h) are the same images as (a) to (d) with edge effect absent.

Bibliography

[1] H. S. Newman and J. C. Culbertson, "Measurement of the current-density distribution in high-temperature superconducting microstrip by means of kinetic-inductance photoresponse," *Microwave and Optical Technology Letters*, vol. 6, no. 13, pp. 725–728, 1993.

[2] J. C. Culbertson, H. S. Newman, and C. Wilker, "Optical probe of microwave current distributions in high temperature superconducting transmission lines," *Journal of applied physics*, vol. 84, no. 5, pp. 2768–2787, 1998.

[3] A. P. Zhuravel, C. Kurter, A. V. Ustinov, and S. M. Anlage, "Unconventional rf photoresponse from a superconducting spiral resonator," *Physical Review B*, vol. 85, no. 13, p. 134535, 2012.

[4] A. Zhuravel, A. Ustinov, K. Harshavardhan, and S. M. Anlage, "Influence of laalo3 surface topography on rf current distribution in superconducting microwave devices," *Applied physics letters*, vol. 81, no. 26, pp. 4979–4981, 2002.

[5] A. Zhuravel, A. Ustinov, D. Abraimov, and S. M. Anlage, "Imaging local sources of intermodulation in superconducting microwave devices," *Applied Superconductivity, IEEE Transactions on*, vol. 13, no. 2, pp. 340–343, 2003.

[6] A. Zhuravel, A. Ustinov, K. Harshavardhan, S. Remillard, and S. M. Anlage, "Microscopic imaging of rf current distribution and intermodulation sources in superconducting microwave devices," in *Materials Research Society Symposium Proceedings, EXS-3, EE9*, vol. 7, 2004.

[7] A. P. Zhuravel, B. Ghamsari, C. Kurter, P. Jung, S. Remillard, J. Abrahams, A. Lukashenko, A. V. Ustinov, and S. M. Anlage, "Imaging the

anisotropic nonlinear meissner effect in nodal yba 2 cu 3 o 7- δ thin-film superconductors," *Physical review letters*, vol. 110, no. 8, p. 087002, 2013.

[8] A. Zhuravel, A. Sivakov, O. Turutanov, A. Omelyanchouk, S. M. Anlage, and A. Ustinov, "Laser scanning microscopy of hts films and devices," *arXiv preprint cond-mat/0512582*, 2005.

[9] A. P. Zhuravel, S. M. Anlage, and A. V. Ustinov, "Measurement of local reactive and resistive photoresponse of a superconducting microwave device," *Applied physics letters*, vol. 88, no. 21, p. 212503, 2006.

[10] P. K. Day, H. G. LeDuc, B. A. Mazin, A. Vayonakis, and J. Zmuidzinas, "A broadband superconducting detector suitable for use in large arrays," *Nature*, vol. 425, no. 6960, pp. 817–821, 2003.

[11] M. Rösch, *Development of lumped element kinetic inductance detectors for mm-wave astronomy at the IRAM 30 m telescope*. PhD thesis, Karlsruher Institutes of Technology, 2013.

[12] D. Moore, B. Mazin, S. Golwala, B. Bumble, J. Gao, B. Young, S. Mchugh, P. Day, H. LeDuc, and J. Zmuidzinas, "Quasiparticle trapping in microwave kinetic inductance strip detectors," in *AIP Conference Proceedings*, no. 1185, pp. 168–171, American Institute of Physics, 2009.

[13] A. Potočnik, "Seminar: Laser scanning microscopy of lumped element resonators," 2015.

[14] C. J. Gorter and H. Casimir, "The thermodynamics of the superconducting state," *Z. tech. phys*, vol. 15, pp. 539–42, 1934.

[15] Ashcroft and Mermin, *Solid State Physics*. Saunders College, 1976.

[16] G. Rickayzen, "The two-fluid model of superconductivity," *Proceedings of the Physical Society*, vol. 89, pp. 129–134, Sept. 1966.

[17] K. Yoo, X. Zhao, M. Siddique, R. Alfano, D. Osterman, M. Radparvar, and J. Cunniff, "Rate of electron—phonon relaxation in niobium," in *Ultrafast Phenomena VII*, pp. 357–359, Springer, 1990.

[18] F. London and H. London, "The electromagnetic equations of the supraconductor," vol. 149, no. 866, pp. 71–88, 1935.

[19] L. Cohen, A. Cowie, J. Gallop, I. Ghosh, and I. Goncharov, "Microwave power dependence in gd 123 and tl 2212 thin films: Examining the evidence for limiting behavior," *Journal of superconductivity*, vol. 10, no. 2, pp. 85–90, 1997.

[20] M. I. Tsindlekht, E. B. Sonin, M. A. Golosovsky, D. Davidov, X. Castel, M. Guilloux-Viry, and A. Perrin, "Microwave properties of $yba_2cu_3o_{7-\delta}$ thin films in linear and nonlinear regime in a dc magnetic field," *Phys. Rev. B*, vol. 61, pp. 1596–1604, Jan 2000.

[21] E. Maxwell, P. Marcus, and J. C. Slater, "Surface impedance of normal and superconductors at 24,000 megacycles per second," *Physical Review*, vol. 76, no. 9, p. 1332, 1949.

[22] A. Abadal, *Josephson Parametric Amplifiers with Lumped-element Coupled Resonators*. PhD thesis, Master thesis, ETH Zürich, 2015.

[23] What-When-How, "Electrical conduction in metals and alloys (electrical properties of materials) part 3," 2012.

[24] V. Novotny and P. Meincke, "Single superconducting energy gap in pure niobium," *Journal of Low Temperature Physics*, vol. 18, no. 1-2, pp. 147–157, 1975.

[25] G. Puebla-Hellmann, *DC, Microwave and Optical Measurement Schemes for Nano-Scale Devices*. PhD thesis, ETH Zürich, 2012.

[26] AttocubeSystemsAG, "Working principle – premium line positioners," 2015.

[27] C. Stutt, "Low-frequency spectrum of lock-in amplifiers," 1949.

[28] C. Eichler, *Experimental Characterization of Quantum Microwave Radiation and its Entanglement with a Superconducting Qubit*. PhD thesis, ETH Zürich, 2013.

[29] R. . Schwarz, "R & s smb100a rf and microwave signal generator," 2015.

[30] A. Clerk, M. Devoret, S. Girvin, F. Marquardt, and R. Schoelkopf, "Introduction to quantum noise, measurement, and amplification," *Reviews of Modern Physics*, vol. 82, no. 2, p. 1155, 2010.

[31] C. Lang, *Read-out strategies for multi-qubit states in circuit quantum electrodynamics*. PhD thesis, Diploma thesis, LMU Munich, 2009.

[32] M. Dressel, "Electrodynamics of metallic superconductors," *Advances in Condensed Matter Physics*, vol. 2013, 2013.

[33] A. Leo, G. Grimaldi, R. Citro, A. Nigro, S. Pace, and R. Huebener, "Quasiparticle scattering time in niobium superconducting films," *Physical Review B*, vol. 84, no. 1, p. 014536, 2011.

[34] R. C. Dougherty and J. D. Kimel, "Temperature dependence of the superconductor energy gap," *arXiv preprint arXiv:1212.0423*, 2012.

[35] M. Göppl, *Engineering Quantum Electronic Chips - Realization and Characterization of Circuit Quantum Electrodynamics Systems*. PhD thesis, ETH, Zürich, 2009.

[36] M. Tinkham, *Introduction to Superconductivity*. Dover Publications Inc, 1996.

[37] W. R. Hudson and R. J. Jirberg, "Superconducting properties of niobium films," tech. rep., National Aeronautics and Space Administration, Cleveland, Ohio (USA). Lewis Research Center, 1971.

[38] C. Eichler, J. Mlynek, J. Butscher, P. Kurpiers, K. Hammerer, T. Osborne, and A. Wallraff, "Exploring interacting quantum many-body systems by experimentally creating continuous matrix product states in superconducting circuits," *arXiv preprint arXiv:1508.06471*, 2015.

[39] V. Lindberg, "Uncertainties and error propagation part i of a manual on uncertainties, graphing, and the vernier caliper," 2000.

[40] A. Sergeev, V. Mitin, and B. Karasik, "Ultrasensitive hot-electron kinetic-inductance detectors operating well below the superconducting transition," *Applied physics letters*, vol. 80, no. 5, pp. 817–819, 2002.

ETH

Eidgenössische Technische Hochschule Zürich
Swiss Federal Institute of Technology Zurich

Declaration of originality

The signed declaration of originality is a component of every semester paper, Bachelor's thesis, Master's thesis and any other degree paper undertaken during the course of studies, including the respective electronic versions.

Lecturers may also require a declaration of originality for other written papers compiled for their courses.

I hereby confirm that I am the sole author of the written work here enclosed and that I have compiled it in my own words. Parts excepted are corrections of form and content by the supervisor.

Title of work (in block letters):

Laser Scanning Microscopy on Microwave Superconducting Lumped Element Resonators

Authored by (in block letters):
For papers written by groups the names of all authors are required.

Name(s):	**First name(s):**
Chen	Junxin

With my signature I confirm that

- I have committed none of the forms of plagiarism described in the 'Citation etiquette' information sheet.
- I have documented all methods, data and processes truthfully.
- I have not manipulated any data.
- I have mentioned all persons who were significant facilitators of the work.

I am aware that the work may be screened electronically for plagiarism.

Place, date	**Signature(s)**
Zürich, 10/11/2015	Junxin Chen

For papers written by groups the names of all authors are required. Their signatures collectively guarantee the entire content of the written paper.